Tracing the Dynamics in Venus' Upper Atmosphere

by

Amanda S. Brecht

A dissertation submitted in partial fulfillment
of the requirements for the degree of
Doctor of Philosophy
(Atmospheric and Space Sciences)
in The University of Michigan
2011

Doctoral Committee:

Research Professor Stephen W. Bougher, Chair
Professor Emeritus Andrew F. Nagy
Associate Professor Edwin A. Bergin
Assistant Professor Christiane Jablonowski
Assistant Research Scientist Christopher D. Parkinson

ACKNOWLEDGEMENTS

As I began graduate school I was told the journey ahead was like a marathon. Along this journey I tackled mentally challenging problems. I learned how to think analytically, ask questions, take risks, and not to be afraid of being wrong. I have learned more about myself and science than I ever thought I would. My journey would not have been possible without the many people who cheered me on, encouraged me, and helped me through the tough stretches.

Special thanks go to Dr. Janet Luhmann for providing the opportunity to work as a summer intern at Space Sciences Laboratory, UC Berkeley, and encouraging my curiosity in space science. Also I thank her for her continuing support through my years in graduate school. Another person responsible for my being here is Professor Andrew F. Nagy who called and asked me honestly "Are you serious about wanting to come to graduate school?" That call helped me make a very important decision in my life. He has been my "grandfather" advisor for all these years and has provided support and guidance whenever I needed it.

Next, I would like to acknowledge my "coach" in this marathon, my adviser Dr. Stephen W. Bougher. I owe him a great deal of gratitude. He was willing to take me on as a graduate student on short notice and turn me into a research scientist. Without his patience and guidance I would not have gotten through all the tough stretches: his door was always open and he was available to listen. His wealth of knowledge in the field provided the confidence I needed to tackle those difficult questions like, "How did I blow up Venus?" He advised me, coached me, and gave me many opportunities

to attend conferences in the US and Europe.

To Ben Foster, my NCAR contact and computer guru, thank you for all the continual support, especially in those last few weeks. His insight and time helped propel the numerical side of upgrading the VTGCM. It also was an amazing experience collaborating with Dr. Jean-Claude Gerard from the University of Liege, Belgium. He generously shared his research results and his knowledge of the Venus Express nightglow data. To Dr. Hunter Waite who first took a chance on having me as a graduate student. For the short time we worked together he was always encouraging.

From the beginning to the end of this marathon, I have had amazing support from the entire AOSS department chaired by Dr. Tamas Gombosi. His needling, humor and insight truly were and are appreciated. Yes, Dr. Gombosi "Trouble" is finally leaving. A special thank you to the graduate students who have befriended me over the years: Dan Welling, Dave Pawlowski, Tami McDunn, Yiqun Yu, Patty Dowd, Jared Bell, Anna DeJong, Dalal Najib, Raluca Ille, Manish Mehta, and Kim Kreykes, to name a few. They all have made an impact on my success as a graduate student from helping with classwork, being supportive office-mates, sharing medical experiences, telling funny stories, to guidance through a life as a graduate student. The AOSS department list would not be complete without acknowledging the ever so supportive staff. Thank you, Margaret Reid, Debbie Eddy, Jan Beltran, Sue Griffin, Darla Briggs, and Bryan White.

To my committee members: Dr. Bougher, Professor Nagy, Professor Bergin, Professor Jablonowski, and Dr. Parkinson, thank you for taking the time and effort to be part of my defense processes and providing insightful revisions for my dissertation.

Heartfelt thanks go to my family for the unconditional support they have shown from day one. To my Dad, Steve, thank you for asking me questions and "talking science" when I needed to sort through a problem. To my Mom, Nancy, thank you for understanding everything I was going through. To my brothers, Andrew and

Matthew, thank you for always keeping me grounded and making sure I was still alive. To my Husband, James Weber, who has been there for all the emotional lows and highs and the stresses and successes. Jamie you have given me the extra strength to get through this journey.

TABLE OF CONTENTS

ACKNOWLEDGEMENTS ii

LIST OF FIGURES viii

LIST OF TABLES xii

LIST OF ABBREVIATIONS xiv

ABSTRACT xvi

CHAPTER

I. Introduction 1

- 1.1 Introduction 1
- 1.2 Brief Introduction to the Lower Atmosphere Dynamics 3
- 1.3 Brief Introduction to the Middle and Upper Atmospheric Dynamics 5
  - 1.3.1 Zonal Winds 6
  - 1.3.2 Meridional Winds 7
  - 1.3.3 Polar Vortices 8
  - 1.3.4 Waves and Tides 9
- 1.4 Outline of Upcoming Chapters 11

II. Upper Atmosphere Observations and Data Sets (∼70 - 200 km) 12

- 2.1 Introduction 12
- 2.2 Mariner Missions 13
- 2.3 Venera Missions/Vega Missions 16
- 2.4 Pioneer Venus Missions 19
  - 2.4.1 Understanding of the Thermal Structure 22
  - 2.4.2 Understanding of the Neutral Gas Composition . . . 23
  - 2.4.3 Understanding of the Night Airglow 25

2.4.4 Understanding of the Ionosphere 28
2.4.5 Understanding of Gravity Waves 29
2.5 Ground-based Observations 29
2.5.1 Ground-based Nightside Temperature Observations 30
2.5.2 Ground-based Wind Observations 32
2.5.3 Ground-based CO Observations 36
2.5.4 Ground-based Airglow Observations 36
2.6 Venus Express Mission 38
2.6.1 VEX Temperature Observations 39
2.6.2 VEX Wind Observations 40
2.6.3 VEX Night Airglow Observations 41
2.6.4 VEX Gravity Wave Observations 44
2.7 Outstanding Problems and Unresolved Issues 45

III. Numerical Modeling of Venus 48

3.1 Introduction 48
3.2 One Dimensional Empirical Models 48
3.3 One Dimensional Theoretical Models 52
3.4 Two Dimensional Theoretical Models 56
3.5 Three-Dimensional General Circulation Models 57
3.6 The Three-Dimensional Venus Thermospheric General Circulation Model 60
3.6.1 VTGCM Description 61
3.6.2 VTGCM Numerical Formulation 63
3.6.3 VTGCM Implementation 68
3.6.4 NO UV Nightglow and N-production 71
3.6.5 Updated Airglow Chemistry 72
3.6.6 Re-evaluated Chemical Rate Coefficients 77
3.6.7 Chemical Trace Species at lower altitudes 78
3.7 Double Resolution Examination 79
3.8 Gravity Wave Momentum Drag Scheme 80
3.9 Summary 82

IV. Results and Implications 84

4.1 Introduction 84
4.2 VTGCM “Mean” Simulation 84
4.2.1 “Mean” Simulation - Parameters for VEX conditions 85
4.2.2 “Mean” Simulation - Results 85
4.2.3 Sensitivity Tests upon the “Mean” Simulation . . . 95
4.2.4 Implications and Data Model Comparisons 100
4.3 Atomic Oxygen Distributions 105
4.3.1 Introduction 105
4.3.2 Observations and Generation of Statistical Maps . . 106

4.3.3 Results 108
4.3.4 Implications for Night Airglow and Thermospheric Circulation 116
4.4 Implications from the Double Resolution Examination 118
4.5 Preliminary Study with Gravity Wave Scheme 120

V. Conclusions and Future Work 124

5.1 Conclusions on VTGCM Mean Simulation 125
5.2 Conclusions on Atomic Oxygen Distributions 126
5.3 Conclusions on VTGCM Numerical and Physical Improvements 126
5.4 Future Work 127

BIBLIOGRAPHY 131

LIST OF FIGURES

Figure

1.1 A cartoon of the Venus circulation patterns. The illustration is looking down at the north pole. MT is the morning terminator, ET is the evening terminator, SS-AS is the subsolar-antisolar wind pattern, RSZ is the retrograde superrotating zonal wind pattern. Adopted from *Schubert et al.* (2007). 7

1.2 South polar dipole mosaic from images by the Visible and Infrared Thermal Imaging Spectrometer instrument on Venus Express from (http://www.esa.int/SPECIALS/Venus_Express/SEM2F373R8F_0.html). 9

1.3 Ultraviolet image of Venus' clouds as seen by the Pioneer Venus Orbiter (Feb. 26, 1979). (http://nssdc.gsfc.nasa.gov/) 10

2.1 Solar flux during the successful missions to Venus 13

3.1 Block diagram illustrating previous Venus models which have led to the present three-dimensional model adapted from *Bougher* (1985). 49

3.2 The prescribed RSZ (m s^{-1}) wind in the VTGCM as a function of log pressure ($Z_p = \ln(P_o/P)$). 70

3.3 VTGCM simplified dayside odd oxygen chemical scheme. This provides the sources for atomic O which is transported to the nightside to produce the O_2 IR and NO UV night airglow emissions. 73

3.4 VTGCM simplified dayside odd nitrogen chemical scheme. Taken from *Bougher et al.* (1990). 74

4.1 VTGCM "mean" case for VEX conditions; longitude-height cross section at 2.5°N (local time vs height) for neutral temperature (K). 87

4.2 The heating and cooling terms at LT = 12:00 (left panel) and LT = 24:00 (right panel) near the equator. The hashed lines represent cooling and the solid lines represent heating 87

4.3 VTGCM "mean" case profiles at 2.5°N: (a) temperature (K) at 0000 LT and (b) total dynamical heating rate (K/day) (adiabatic + total advection) at 0000 LT. 88

4.4 VTGCM "mean" case for VEX conditions; longitude-height cross section at 2.5°N (local time vs height) for zonal winds (m s^{-1}) . . . 90

4.5 VTGCM "mean" case for VEX conditions; longitude-height cross section at 2.5°N: (a) the morning terminator (MT) total zonal winds (m s^{-1}) where the solid line represents the asymmetric case and the dashed line represents the symmetric case, (b) the evening terminator (ET) total zonal winds (m s^{-1}) where the solid line represents the asymmetric case and the dashed line represents the symmetric case, and (c) the retrograde zonal winds (RSZ) prescribed as a function with height (m s^{-1}). 90

4.6 VTGCM "mean" case for VEX conditions; density profiles at 2.5°N (density vs height) for atomic oxygen at noon and midnight. The density is in units of cm^{-3}. 91

4.7 VTGCM "mean" case for VEX conditions; density profiles at 2.5°N (density vs height) for N(^{4}S) at noon and midnight. The density is in units of cm^{-3}. 91

4.8 VTGCM "mean" case for VEX conditions; longitude-height cross section at 2.5°N (local time vs height) illustrates a max O_2 IR night airglow volume emission rate close to midnight. The emission rate unit is $\log_{10}$(photons cm^{-3} s^{-1}). 92

4.9 VTGCM "mean" case for VEX conditions; longitude-height cross section at 2.5°N (local time vs height) illustrates a max NO UV night airglow volume emission rate close to 01:00 LT. The emission rate unit is $\log_{10}$(photons cm^{-3} s^{-1}). 93

4.10 VTGCM "mean" case for VEX conditions; time scale profiles at 2.5°N (time (day) vs height (km)) for midnight. 94

4.11 Altitude slice at 103 km from the three-dimensional map of atomic oxygen density (cm^{-3}) derived from the VEX O_2 IR nightglow emission map (local time vs latitude) (*Soret et al.*, 2010a). The maximum value is 2.8 x 10^{11} cm^{-3}. 107

4.12 VTGCM “mean” case for VEX conditions; altitude slice at 103 km (local time vs latitude) for atomic oxygen density (cm^{-3}). The maximum value = 3.7 x 10^{11} cm^{-3}. 109

4.13 Vertical profiles of CO_2 density (cm^{-3}) near the equator at 0000 LT on a log scale. VTGCM “mean” case for VEX conditions with trace species (solid line with dots), VEX-SPICAV CO_2 mean density vertical profiles (solid line), VTS3 CO_2 density vertical profiles (circles). 111

4.14 Vertical profiles of O density (cm^{-3}) near the equator at different local times, 2200 LT (left), 0000 LT (center), 0200 LT (right), on a log scale. VTGCM “mean” case for VEX conditions with trace species (solid line with dots) and without trace species (dashed line). VEX O density vertical profiles derived from the O density maps (solid line). The VEX profile is given above 90 km due to the limitations of CO_2 (SPICAV) densities. 112

4.15 Vertical profiles of O density (cm^{-3}) near the equator at different local times, 2000 LT (left), 0000 LT (center), 0400 LT (right), on a log scale. VTGCM “mean” case for VEX conditions with trace species (solid line with dots) and without trace species (dashed line). VEX O density vertical profiles derived from the O density maps (solid line). The VEX profile is given above 90 km due to the limitations of CO_2 (SPICAV) densities. 113

4.16 Vertical profiles of O density (cm^{-3}) near 0000 LT at different latitudes, 30°N (left), 0° (center), 30°S LT (right), on a log scale. VTGCM “mean” case for VEX conditions with trace species (solid line with dots) and with out trace species (dashed line). VEX O density vertical profiles derived from the O density maps (solid line). The VEX profile is given above 90 km due to the limitations of CO_2 (SPICAV) densities. 114

4.17 Vertical profiles of O density (cm^{-3}) near 0000 LT at different latitudes, 0° (left), 45°S (center), 60°S LT (right), on a log scale. VTGCM “mean” case for VEX conditions with trace species (solid line with dots) and with out trace species (dashed line). VEX O density vertical profiles derived from the O density maps (solid line). The VEX profile is given above 90 km due to the limitations of CO_2 (SPICAV) densities. 115

4.18 VTGCM "mean" case for VEX conditions at 2.5° x 2.5° resolution; longitude-height cross section at 2.5°N (local time vs height). Neutral temperature (K) is on the left side and zonal winds (m s^{-1}) are on the right side. 119

4.19 VTGCM "mean" case for VEX conditions at 2.5° x 2.5° resolution; longitude-height cross section at 2.5°N (local time vs height). A illustration of the max O_2 IR night airglow volume emission rate close to midnight in the left panel and the max NO UV night airglow volume emission rate close to 01:00 LT in the right panel. The emission rate unit is $\log_{10}$(photons cm^{-3} s^{-1}). 119

4.20 VTGCM "mean" case for VEX conditions; longitude-height cross section at 2.5°N (local time vs height) for the zonal drag (m s^{-2}) due to Rayleigh friction. The maximum drag is 0.012 m s^{-2} near 140 km at 06:00 LT. 120

4.21 VTGCM "mean" case with *Fritts and Lu* (1993) wave drag scheme replacing Rayleigh friction. Both figures are longitude-height cross sections at 2.5°N (local time vs height) illustrating neutral temperature (K). The figure on the left prescribed phase speeds of 6 m s^{-1} and the figure on the right prescribed phase speeds of 8 m s^{-1}. . . . 121

4.22 VTGCM "mean" case with *Fritts and Lu* (1993) wave drag scheme replacing Rayleigh friction. Both figures are longitude-height cross sections at 2.5°N (local time vs height) illustrating zonal winds (m s^{-1}). The figure on the left prescribed phase speeds of 6 m s^{-1} and the figure on the right prescribed phase speeds of 8 m s^{-1}. 121

4.23 VTGCM "mean" case with *Fritts and Lu* (1993) wave drag scheme replacing Rayleigh friction. Both figures are longitude-height cross sections at 2.5°N (local time vs height) illustrating the magnitude of drag (m s^{-1}). The figure on the left prescribed phase speeds of 6 m s^{-1} and the figure on the right prescribed phase speeds of 8 m s^{-1}. . 122

LIST OF TABLES

Table

1.1 Venus and Earth property comparison 2

2.1 Successful Missions To Venus 14

2.2 Pioneer Venus Orbiter Mission Payload 20

2.3 Pioneer Venus Large Probe Payload 21

2.4 Pioneer Venus Small Probes Payload 22

2.5 Summary of temperature measurements for the Venus nightside near 95 km from *Bailey et al.* (2008) 32

2.6 Ground-based equatorial wind measurements adapted from *Lellouch et al.* (1997) and *Sornig* (2009) 34

2.7 Ground-based equatorial wind measurements continued from Table 2.6. 35

2.8 Venus Express Mission Payload 39

2.9 Three-Dimensional modeling constraints from observations 46

3.1 The VTGCM upgrades completed for this dissertation. 71

3.2 Key O_2 IR and NO UV nightglow parameters. Rate coefficients are $cm^3\ sec^{-1}$ and three body rate coefficients are $cm^6\ sec^{-1}$ 76

4.1 Results from the Nightside Eddy Diffusion sensitivity test 96

4.2 Results from the wind sensitivity test 98

4.3 Key Chemical Reaction Rate Tests (cm^6 s^{-1}) 99

4.4 Density map values at 103 km (cm^{-3}) for specific locations from VTGCM simulation and VEX data 110

4.5 Vertical profile density peaks (cm^{-3}) and altitude (km) for VTGCM simulations and VEX data 112

LIST OF ABBREVIATIONS

BIMS PV Bus Ion Mass Spectrometer

BNMS PV Bus Neutral Mass Spectrometer

CAM Community Atmosphere Model

ET Evening Terminator

F10.7 10.7 cm radio flux, measured at Earth, normalized to 1 AU and measured in the units of 10^{-22} W m^{-2} Hz^{-1}; historically used as a proxy of EUV radiation incident upon the Earth's upper atmosphere.

GCM General Circulation Model

GRW Gierasch-Rossow-Williams

GSFC Goddard Space Flight Center

HHSMT Heinrich Hertz Submillimeter Telescope

kR kilo-Rayleigh (10^{10} photons cm^{-2} s^{-1} into 4π sr)

LMD Laboratoire de Météorologie Dynamique

LT Local Time

MR Mega-Rayleigh (10^{12} photons cm^{-2} s^{-1} into 4π sr)

MS Morningside

MT Morning Terminator

NCAR National Center for Atmospheric Research

NLTE Non-Local Thermodynamic Equilibrium

OAD Orbiter Atmospheric Drag

OETP PV Orbiter Electron Temperature Probe

OIMS PV Orbiter Ion Mass Spectrometer

ONMS PV Orbiter Neutral Mass Spectrometer

OPA PV Orbiter solar wind Plasma Analyzer

ORO PV Orbiter Radio Occultation

ORPA PV Orbiter Retarding Potential Analyzer

OUVS PV Orbiter Ultraviolet Spectrometer

PV Pioneer Venus

PVO Pioneer Venus Orbiter

PVM Pioneer Venus Multiprobe

RSZ Retrograde Superrotating Zonal

SPICAV Spectroscopy for Investigation of Characteristics of the Atmosphere of Venus

SS-AS Subsolar to AntiSolar

SZA Solar Zenith Angle

TIME-GCM Thermosphere Ionosphere Mesosphere Electrodynamics General Circulation Model

VeRa Venus Express Radio Science

VEX Venus Express

VIRTIS Visible and Infrared Thermal Imaging Spectrometer

VMC Venus Monitoring Camera

VTGCM Venus Thermospheric General Circulation Model

ABSTRACT

Venus is a unique planet because its atmospheric dynamics are mainly driven by thermal heating and its very low rotation rate. Many details of the middle and upper atmospheric dynamics can be determined from observing nightside airglow emissions, which serve as effective tracers of Venus' middle and upper atmosphere global wind system. The purpose of this dissertation is to use the National Center for Atmospheric Research (NCAR) Venus Thermospheric General Circulation Model (VTGCM) to examine the underlying processes that control the thermospheric circulation of Venus by comparing simulations to observations. Most recently, Venus Express (VEX) has been monitoring key atmospheric features (O_2 IR nightglow, NO UV nightglow, and nightside temperatures) of Venus. Statistical maps have been created utilizing these nightglow observations from VEX. Moreover, the O_2 IR statistical map has been used to deduce a three-dimensional atomic oxygen density map, which is used to examine the implications of atomic oxygen density distributions below 140 km on the nightside.

The VTGCM model has been reconstructed and revised in order to address these key nightglow observations and provide diagnostic interpretation. Specifically, the VTGCM simulations capture the statistically averaged mean state of these three key observations. The correlation between the simulation results and the VEX data sets implies a weak retrograde superrotating zonal flow (RSZ) from ∼80 km to 110 km with the emergence of modest RSZ winds approaching 60 m s^{-1} above ∼130 km. This RSZ flow is superimposed upon a strong subsolar-antisolar flow from day-to-night. VTGCM sensitivity tests were subsequently performed using two tunable parameters (nightside eddy diffusion and wave drag) to examine corresponding variability within

the VTGCM and these nightglow distributions.

The VTGCM also reproduces a nightside atomic oxygen density map and vertical profiles across the nightside. Both the simulated map and vertical profiles are in close agreement with VEX observations within a ∼30° contour of the anti-solar point. The atomic oxygen vertical profiles are comparable to the data above 90 km, consistent with the corresponding O_2 IR nightglow intensities. The research performed for this dissertation has determined the parametric sensitivity of the thermospheric flow around Venus.

CHAPTER I

Introduction

1.1 Introduction

Throughout centuries of scientific study, Venus has often been described as Earth's twin. Yet apart from size, mass, density, and volume, Venus is vastly different. Table 1.1 is a chart of Venus' relevant properties along side comparable Earth's properties. The atmosphere of Venus is almost entirely CO_2, but is also noted for its sulfuric acid clouds which cover the whole planet. Due to the planet's thick cloud layer, Venus' surface was a mystery until the mid-1950's (e.g. *Colin*, 1983). The surface of Venus is relatively flat, compared to Earth, and is the hottest planetary surface in our solar system ($\sim$750 K) (e.g. *Seiff*, 1983). Along with these atmospheric properties, Venus' axis of rotation is inclined at 177.36 degrees (with respect to Earth) with a very small inclination (*Carpenter*, 1964; *Goldstein*, 1964; *Shapiro*, 1968; *Colin*, 1983). By comparison to Earth, this means Venus rotates in the opposite direction; i.e. the Sun rises in the West instead of the East. In addition to the axis of rotation and direction, Venus has a very slow rotation speed. The Venus year is shorter than the Venus day. For comparison, a Venus day is equivalent to 243 Earth days, while a Venus year is 224.7 Earth days (*Shapiro*, 1968).

In addition to these properties, the temperature resulting from absorption of solar radiation is a major driver for Venus' atmospheric dynamics. Venus' proximity to

Table 1.1: Venus and Earth property comparison

Physical Elements	Venus	Earth
Mean Distance From Sun (km)	108.2 x 10^6	149.6 x 10^6
Major Atmospheric Component	CO_2	N_2
Mass (kg)	4.871 x 10^{24}	5.976 x 10^{24}
Equatorial Radius (km)	6051.3	6378
Mean Density (g/cm^3)	5.24	5.52
Surface Pressure kPa (atm)	9000(90)	101.3 (1)
Surface Gravity (m s^{-2})	8.87	9.78
Solar Irradiance (W m^{-2})	2613.9	1367.6
Obliquity (°)	-2.6	23.45
Eccentricity	0.006787	0.0167
Sidereal Rotation Period (Earth Units)	243.01 day	23.9345 hr
Orbital Period (Earth Day)	224.701	365.256
Existence Of Internal Magnetic Field	No	Yes

the sun coupled with the planet's slow rotation speed results in the upper boundary, exobase (∼250 km on the dayside), varying from 300 K on the dayside to 100 K on the nightside during solar maximum conditions (*Barth*, 1968; *Rottman and Moos*, 1973; *Strickland*, 1973; *Kumar and Broadfoot*, 1975; *Anderson*, 1976). The region from the exobase down to ∼100 km is known as the thermosphere. In part, due to the slow rotation, the nightside thermosphere is characterized as a "cryosphere" because the temperatures decrease with altitude while on the dayside the temperatures increase with altitude (*Keating et al.*, 1979b,c; *Schubert et al.*, 1980). Below the thermosphere is the cloud deck, ∼50-70 km, which absorbs solar radiation resulting in warmer temperatures with decreasing altitude. Meanwhile, at the surface, Venus is hotter than any other planet in our solar system. In the region from the surface to the cloud deck, the planet stays globally warm due to the proximity to the Sun and the Greenhouse Effect (*Wildt*, 1940a,b; *Sagan*, 1961; *Pollack and Sagan*, 1965a,b). These extreme conditions result in Venus having unique global dynamics.

1.2 Brief Introduction to the Lower Atmosphere Dynamics

The lower atmosphere, 0 - ∼70km, will be briefly discussed in this section. Moreover, it is important to discuss the lower atmosphere in order to provide a global view of Venus' atmospheric dynamics since the lower atmosphere is closely coupled to the upper atmosphere, ∼100 - ∼250.

The primary dynamical feature of the lower atmosphere is the superrotating zonal mean flow, which flows in the same direction as the planet's rotation, and reaches ∼100 m/s at cloud tops. The generation of this superrotation is the most addressed question for the lower atmosphere. At this time, it is thought that the mechanism that drives the Retrograde Superrotating Zonal (RSZ) winds is operating in the deep atmosphere (see next section) (*Counselman et al.*, 1980; *Gierasch et al.*, 1997). In addition, *Schubert* (1983) claimed the momentum per unit volume of the RSZ winds peaks near 20 km, with the likely momentum source being the planet itself.

There are very limited observations of the lower atmosphere. However, *Gierasch et al.* (1997) described what had been observed up to 1997, while *Schubert et al.* (2007) explained the latest developments of our understanding of the lower atmosphere.

The most common theory for the generation of the RSZ flow is called the Gierasch-Rossow-Williams (GRW) mechanism (*Gierasch*, 1975; *Rossow and Williams*, 1979). The theory entails a Hadley cell extending from the surface to the cloud tops (∼70 km), with a poleward flow, in combination with thermal tides, transporting retrograde momentum upward from the solid planet (e.g. *Schubert et al.*, 2007). The existing data is from ground-based observations, including Pioneer Venus, and USSR probes/balloons. However, most of the data had poor accuracy and only provided information at specific locations (*Gierasch et al.*, 1997). Because of the scarce data, scientists turned to numerical analysis to examine the stated theory.

The first successful lower atmosphere general circulation model (GCM) was developed by *Young and Pollack* (1977), and used a weak GRW mechanism. Later, this implementation was deemed erroneous due to the model's vertical diffusion formulation, which could have exaggerated the RSZ flow (*Rossow et al.*, 1980; *Young and Pollack*, 1980).

Later modeling attempts were by *del Genio et al.* (1993) and *del Genio and Zhou* (1996), making use of an Earth GCM but with a slower rotation period to match Venus. They were able to conserve momentum to a high accuracy, the higher altitudes became decoupled due to a layer of high static stability, and they used a strong GRW mechanism. However, the model used the atmospheric mass of Earth (about two orders of magnitude less than Venus), and did not include the day-night cycle (tides) (*Schubert and Whitehead*, 1969). Calculated zonal winds were an order of magnitude slower than the observed wind speeds at the cloud tops.

The next modeling attempts were conducted by *Yamamoto and Takahashi* (2003a,b, 2004, 2006a,b, 2007a,b, 2009a,b). They incorporated the correct atmospheric mass for Venus and the day-night cycle. They also employed a strong GRW mechanism, a Hadley cell extending from the equator to the pole and from the surface to ∼60 km, to produce a RSZ flow. It is important to note that the model had to incorporate an unrealistically large thermal forcing to produce a strong Hadley cell to create the correct RSZ wind magnitude. Similar results were produced by other modeling groups, such as *Hollingsworth et al.* (2007) and *Lee et al.* (2006). *Schubert et al.* (2007) commented about this era of modeling as follows: "with day-night variations included, 'these models' should be capable of simulating most of the superrotation mechanisms suggested since the phenomenon was observed, including the meridional circulation and non-axisymmetric eddies (*Gierasch*, 1975; *Rossow and Williams*, 1979), instability (*Thompson*, 1970) and diurnal solar heating variations such as thermal tides (*Schubert and Whitehead*, 1969; *Newman and Leovy*, 1992)".

The most recent modeling efforts have included topography, thereby capturing the surface-atmosphere interaction. Depending on how various parameterizations were done in the GCM's (e.g. heating, surface drag, model resolution, etc.), the topography might impact the superrotation (*Herrnstein and Dowling*, 2007; *Yamamoto and Takahashi*, 2009a). The latest models are presented by *Yamamoto and Takahashi* (2009a,b); *Lee and Richardson* (2010); *Lebonnois et al.* (2010), and *Parish et al.* (2010). *Parish et al.* (2010) developed a Venus GCM by modifying the Earth-based Community Atmosphere Model (CAM) and uses simplified physics to examine periodicity of the zonal winds. They do not include topography or the diurnal cycle. However, they find the zonal winds below the clouds vary on a decadal time scale near mid-latitudes at 40-60 km. Future work entails incorporating similar physics and features as *Lebonnois et al.* (2010), thus the models can be compared directly. The *Lebonnois et al.* (2010) model, based upon the Laboratoire de Météorologie Dynamique (LMD) Earth model, is the most comprehensive lower atmosphere model. *Lebonnois et al.* (2010) includes surface topography, the diurnal cycle, a dependence of specific heat on temperature, and a consistent radiative transfer calculation. They have multiple cells stacked from the equator to the poles and are maintained with the GRW mechanism. Unfortunately, all these models rely on unrealistically large thermal forcing to properly produce the RSZ winds in Venus' lower atmosphere. However, Venus' lower atmosphere modelers need more observations to help improve parameterizations used in the models.

1.3 Brief Introduction to the Middle and Upper Atmospheric Dynamics

Venus' lower atmosphere dynamics are thought to be intimately coupled with the middle and upper atmospheric dynamics. However, observations are more abundant for Venus' middle and upper atmosphere. A brief overview of Venus' most influential dynamics will be discussed; zonal winds, meridional winds, polar vortices, and waves.

1.3.1 Zonal Winds

Venus has two dominant circulation patterns (see Figure 1.1) (e.g. *Bougher et al.*, 1997, 2006; *Lellouch et al.*, 1997; *Schubert et al.*, 2007). One pattern mainly occurs in the region between the planet's surface and the top of the cloud deck at ∼70 km; this was discussed in the previous section. This region is dominated by a stable wind system, the RSZ flow. The RSZ flow is in the direction of the planet's spin and at the cloud tops has a superrotation rate of 4 Earth days, which is 60 times faster than Venus' planetary body's rotation (*Schubert et al.*, 2007). The second pattern occurs above ∼120 km and is a relatively stable mean subsolar-to-antisolar flow (SS-AS) (*Bougher et al.*, 1997). In the upper atmosphere, Venus has inhomogeneous heating by solar radiation (EUV, UV, and IR) thus providing huge pressure gradients to generate the dominant SS-AS flow pattern (*Dickinson and Ridley*, 1977; *Schubert et al.*, 1980; *Bougher et al.*, 1997). The maximum SS-AS flow above ∼120 km is ∼200 - 300 m/s (*Bougher et al.*, 2006). In the altitude range of ∼70 - ∼120 km, also known as the transition region, the two major flow patterns interact and create a highly variable wind system. This interaction produces at least three modifications to the general flow: (1) a shift in the divergence of the net flow from the subsolar point toward the morning terminator, (2) a stronger wind system at the evening terminator than the morning terminator, and (3) a shift in the convergence of the net flow away from midnight and toward the morning terminator.

These modifications also vary with time and altitude, which reflects the changing importance of underlying drivers and solar cycle variations (*Schubert et al.*, 2007). The specific processes responsible for maintaining and driving variations in the SS-AS and RSZ winds of Venus' atmosphere are still not well understood or quantified. Although, wave mechanisms are thought to be important, it is still uncertain which processes are responsible for the variations in the global zonal flow (*Alexander*, 1992; *Zhang et al.*, 1996; *Bougher et al.*, 1997). More importantly, the interactions between

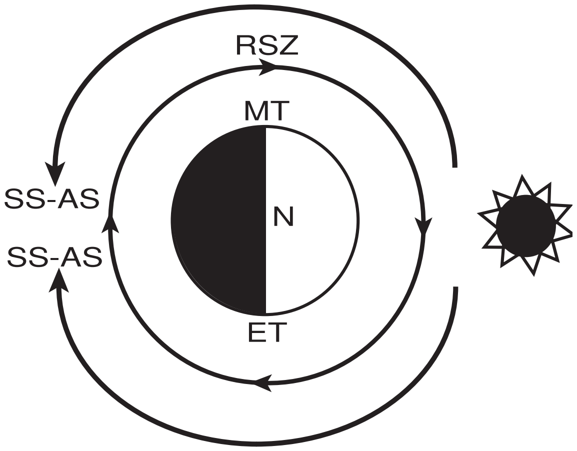

Figure 1.1: A cartoon of the Venus circulation patterns. The illustration is looking down at the north pole. MT is the morning terminator, ET is the evening terminator, SS-AS is the subsolar-antisolar wind pattern, RSZ is the retrograde superrotating zonal wind pattern. Adopted from *Schubert et al.* (2007).

the two flows occur in a region where there is little or no recorded data and where modeling is most challenging.

1.3.2 Meridional Winds

Venus' meridional winds are less intense than the zonal winds but can be very important to the global dynamics. The meridional winds exist due to an imbalance of absorbed solar radiation and emitted infrared radiation, resulting in a circulation pattern from the equator to the poles (*Schubert*, 1983). The stronger meridional winds seem to occur near the cloud level where the solar energy absorption is maximum; these winds are presumed to be part of a cloud level Hadley circulation (*Schubert et al.*, 2007). From past observations (e.g. Pioneer Venus probes), the presumed cloud level Hadley circulation seems to have multiple layers, known as Hadley cells (*Schubert*, 1983). One cell, likely exists from the surface to ∼40 km, another weak indirect cell may be present between ∼40 and 50 km, and finally a strong cloud-level cell is clearly present (*Seiff et al.*, 1980; *Avduevskii et al.*, 1976). Observations for Hadley cells are too limited to verify them; instead they have been inferred from thermal observations and poleward motion cloud-tracked features (*Schubert et al.*, 2007). More recently, cloud tracking has shown meridional winds to peak in mid-latitudes (∼20 m/s) and decrease to zero near the equator and poles (*Limaye*, 2007). In addition, instruments onboard the Venus Express mission have performed simultaneous cloud measurements at different wavelengths, thus providing wind velocities at different altitudes (*Sánchez-Lavega et al.*, 2008). At ∼66 km, they observed 0 m/s winds near the equator and pole and a maximum of 10 m/s near 55 S. However, for the lower altitudes (∼61 km and ∼47 km) the winds were consistently <5 m/s without a latitude trend. Nevertheless, the lower part of the Hadley cell (returning from the pole) has not been observed (*Sánchez-Lavega et al.*, 2008). The meridional winds also contribute to the maintenance of the polar vortices (*Taylor et al.*, 1983; *Schubert et al.*, 2007).

1.3.3 Polar Vortices

The polar vortices are complex dynamical features at Venus' North and South pole. The vortex circulation has been observed since Mariner 10 in 1974 (*Suomi and Limaye*, 1978) and most recently by Venus Express; see Figure 1.2. Based on these observations, these vortices are assumed to be stable and locked over the poles (*Limaye*, 2007). By contrast, terrestrial hurricanes travel and persist until they lose their energy source (*Limaye*, 2007; *Schubert et al.*, 2007). *Limaye* (2007) briefly discusses the similarities and differences between a terrestrial hurricane and Venus' polar vortices. The vortices extend to approximately 65 degrees latitude and are mainly observed at the cloud tops (∼70 km) with a depth of 50 km or maybe more (*Piccioni et al.*, 2007; *Schubert et al.*, 2007). Visible and ultra-violet observations have detected the polar vortices in an 'S' like shape at each pole. This 'S' shape represents a polar dipole, having two centers of atmospheric rotation in the overall direction of the planet's rotation (*Piccioni et al.*, 2007). The 'S' shape structure is surrounded by a "cold collar", a region that is slightly cooler than the rest of the pole

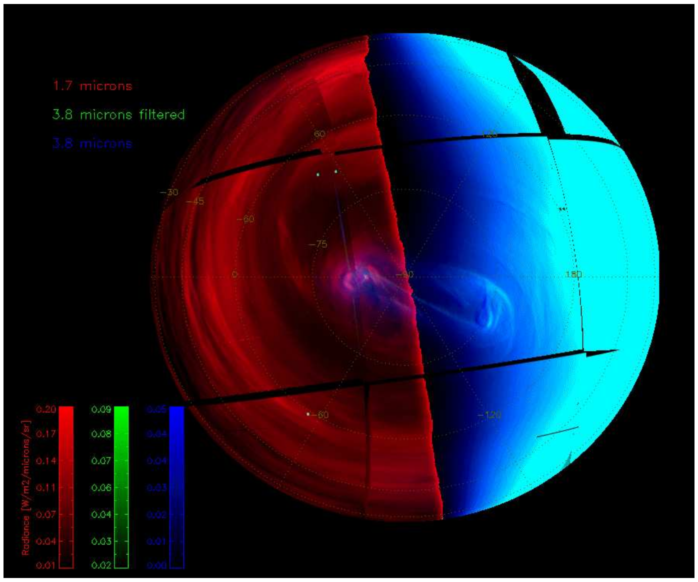

Figure 1.2: South polar dipole mosaic from images by the Visible and Infrared Thermal Imaging Spectrometer instrument on Venus Express (http://www.esa.int/SPECIALS/Venus_Express/SEM2F373R8F_0.html).

(∼30 K) (*Titov et al.*, 2008). The "cold collar" is observed between 50°-70° latitude (e.g. *Taylor et al.*, 1980), *Titov et al.* (2008). In theory the vortices exist due to the combination of thermal transport by the poleward meridional winds (cloud level Hadley cell) and the influence of RSZ winds *Suomi and Limaye* (1978). However, the actual vertical structure of these vortices is poorly defined, and the influence of the vortex circulation on the rest of Venus' atmosphere is unknown.

1.3.4 Waves and Tides

Waves of various spatial and temporal scales exist throughout Venus' atmosphere. The existence of planetary-scale waves (a wave due to shear in rotating fluids with respect to latitude, for Earth they are due to the variation in the Coriolis effect with latitude) and gravity waves (a wave disturbance in which buoyancy (or reduced gravity) acts as restoring force on parcels displaced from hydrostatic equilibrium) are easily confirmed using photographs of Venus' clouds (e.g. *Belton et al.*, 1976b,c,a; *Rossow et al.*, 1980; *Peralta et al.*, 2008). Some of the wave structures are seen as

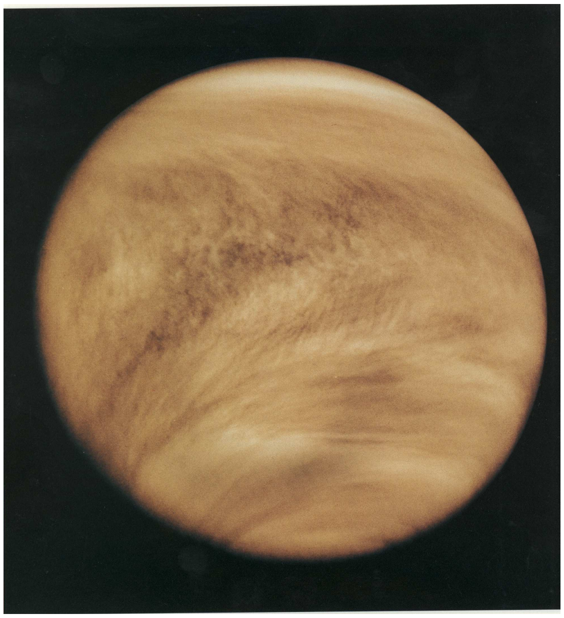

Figure 1.3: Ultraviolet image of Venus' clouds as seen by the Pioneer Venus Orbiter on Feb. 26, 1979. (http://nssdc.gsfc.nasa.gov/)

bands in the ultra-violet; these bands are traveling waves because the bands do not align with any circle of latitude and the bands travel at a different velocity than the background velocity (*Schubert*, 1983). The most noted wave feature is the dark horizontal "Y", shown in Figure 1.3 (e.g. *Belton et al.*, 1976b,c,a; *Rossow et al.*, 1980; *Schubert*, 1983). More recently, the Venus Express mission has been augmenting our knowledge of gravity waves in Venus' atmosphere by identifying regular cloud patterns as gravity waves (*Markiewicz et al.*, 2007; *Peralta et al.*, 2008). Waves are also observed in vertical variations of infrared temperature soundings, radio occultation temperatures, upper atmosphere number densities, and other atmospheric quantities *Schubert* (e.g. 1983); *Covey and Schubert* (e.g. 1981a,b, 1982); *Kasprzak et al.* (e.g. 1988); *Bougher et al.* (e.g. 1997). In addition to wave mechanisms in Venus' atmosphere, thermal tides have been observed in thermal structure data and in atmospheric circulation (*Schofield and Taylor*, 1983; *Limaye*, 1990). Modeling efforts were employed to fill observational gaps on the dynamical implications (*Pechmann and Ingersoll*, 1984; *Newman and Leovy*, 1992); nonetheless models were not able to reproduce the observations. More information about waves, wave observations, and their implications will be discussed in Chapter 2.

1.4 Outline of Upcoming Chapters

With this quick overview of Venus, this dissertation will now begin focusing strictly on the upper atmosphere (70 km and above). Chapter 2 reviews Venus' upper atmosphere observations and data sets. In this chapter, we will discuss the outstanding questions for Venus' upper atmosphere and subsequently the main question(s) and focus of this dissertation. Chapter 3 is a discussion of previous upper atmosphere modeling efforts, past and present modeling efforts using the VTGCM, and lastly the gravity wave model which is used in coordination with the VTGCM. Chapter 4 discusses the results found from the comparison of various datasets and VTGCM modeling. Lastly, Chapter 5 is a conclusion of this dissertation and shows what future work can be done.

CHAPTER II

Upper Atmosphere Observations and Data Sets (∼70 - 200 km)

2.1 Introduction

Venus has been observed from space and the ground for a long period of time. For this chapter, the time period discussed will be from the 1960's to the present. Most of the past and present Venus missions which observed the upper atmosphere are shown in Figure 2.1 and are plotted with repect to solar flux. Associating the Venus mission observing periods with the solar cycle is very useful for scientists studying solar variability and the impacts on Venus' upper atmosphere. Table 2.1 shows all the successful missions that have contributed to the overall knowledge of Venus. This chapter will discuss the most influential missions and the information they provided about the upper atmosphere of Venus. The following sections review the upper atmosphere data sets with the main focus being the Pioneer Venus missions (Pioneer Venus Orbiter and Pioneer Venus Multiprobe) and the Venus Express mission. The sections are as follows: Mariner missions, Venera missions, Pioneer Venus missions, ground-based observations, Venus Express Mission, and a conclusion with a summary of the remaining questions from all these observations.

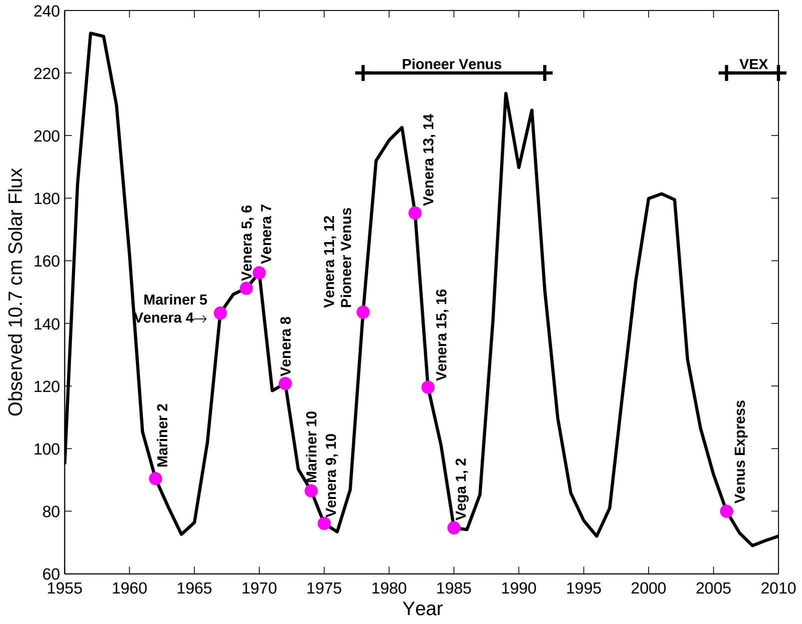

Figure 2.1: Solar flux during the successful missions to Venus

2.2 Mariner Missions

The Americans had the first successful Venus flyby, Mariner 2, in 1962. At this time they were interested in other planetary bodies too. The Mariner 5 and 10 were also American Venus flyby missions, however Mariner 10 was also traveling to Mercury. These were the first two Mariner missions to collect valuable data about the upper atmosphere of Venus. Mariner 5 carried out remote sensing studies, including radio occultation, of the atmosphere. It was also carrying a UV photometer, and several particles and field instruments. Mariner 5 collected data on the magnetic field, atmosphere temperature, and the main atmospheric chemical constituent. More specifically, the radio occultation observations showed a distinct dayside ionospheric layer at ∼140 km with a peak electron density of 5 - 6 x 10^5 cm^{-3}. A secondary (minor) layer was seen about 15 km lower with a peak electron density of ∼2 x 10^5 cm^{-3}. These layers were defined as an F1 and E ionosphere layers, respectively. An F2 layer was ruled out because its creation is based on ion chemistry and vertical diffusion (*Kliore et al.*, 1967). An ionopause was observed to be near 500 km. The

Table 2.1: Successful Missions To Venus

Spacecraft	Launch	Encounter	Type
Mariner 2	Aug. 27, 1962	Dec. 14, 1962	Flyby
Venera 4	June 12, 1967	Oct. 18, 1967	Entry-probe
Mariner 5	June 14, 1967	Oct. 19, 1967	Flyby
Venera 5	Jan. 5, 1969	May 16, 1969	Entry-probe
Venera 6	Jan. 10, 1969	May 17, 1969	Entry-probe
Venera 7	Aug. 17, 1970	Dec. 15, 1970	Lander
Venera 8	March 27, 1972	July 22, 1972	Lander
Mariner 10	Nov. 3, 1973	Feb. 5, 1974	Flyby
Venera 9	June 8, 1975	Oct. 22, 1975	Orbiter/Entry-probe
Venera 10	June 14, 1975	Oct. 25, 1975	Orbiter/Entry-probe
Pioneer Venus 1	May 20, 1978	Dec. 4, 1978	Orbiter
Pioneer Venus 2	Aug. 8, 1978	Dec. 9, 1978	Bus/Entry-probes
Venera 11	Sept. 9, 1978	Dec. 25, 1978	Flyby/Entry-probe
Venera 12	Sept. 14, 1978	Dec. 21, 1978	Flyby/Entry-probe
Venera 13	Oct. 30, 1981	March 1, 1982	Flyby/Entry-probe
Venera 14	Nov. 4, 1981	March 5, 1982	Flyby/Entry-probe
Venera 15	June 2, 1983	Oct. 10, 1983	Orbiter
Venera 16	June 7, 1983	Oct. 14, 1983	Orbiter
Vega 1	Dec. 15, 1984	June 11, 1985	Balloon
Vega 2	Dec. 21, 1984	June 15, 1985	Balloon
Venus Express	Nov. 9, 2005	April 11, 2006	Orbiter

ionopause is the location where the solar-wind ram pressure balances the ionospheric plasma pressure. The UV photometer observed an UV nightglow on the dark limb and a Lyman-alpha airglow (*Barth et al.*, 1967). The Lyman-alpha airglow confirmed the presence of atomic hydrogen in Venus' atmosphere and the variation as a function of altitude suggested Venus' upper atmosphere (exosphere) temperature is lower than the Earth's. Lower altitude temperature profiles in the thermosphere and mesosphere were derived by the refractivity data and also from the 423.3 MHz amplitude data by assuming a mixed atmosphere in hydrostatic equilibrium. On the nightside both sets gave similar results; near 40 km the temperature is ∼450 K and up near 90 km it ranges from 150 K to 250 K. For comparison, Earth's average temperature near 40 km is ∼270 K and near 90 km the average temperature is ∼180 K (e.g. *Gombosi*, 1998).

Mariner 10 conducted remote sensing of Venus in the IR and UV, imaging of the clouds, and space physics experiments. This mission was the first to provide high-resolution UV images of Venus and the images provided information about the general circulation near the cloud tops. The images showed the flow to be symmetrical between north and south hemispheres, the angular velocity to increase towards the poles, and near the equator the zonal wind was determined to be approximately 100 m s^{-1} (*Murray et al.*, 1974). The spectrometer on Mariner 10 provided the first detection of helium, atomic oxygen, and atomic carbon airglow (*Broadfoot et al.*, 1974). The observation of atomic oxygen changed how scientists viewed the ionosphere. With atomic oxygen present, CO_2^+ was eventually determined not to be the dominant ion but instead was quickly transformed by atomic oxygen to O_2^+ which is the dominant ion for the altitude range of ~120 km to 200 km (*Schunk and Nagy*, 2009). With a second look by Mariner 10, *Bauer and Hartle* (1974) claimed the existence of two ledges above the peak electron density and attributed the top ledge near 250 km to the solar-wind "scavenging" of the ionosphere, thereby creating the ionopause. The second ledge was seen near 180 km and was referred to as the F2 peak due to the presence of O^+, similar to that observed by Mariner 5. The F1 peak, which is the main peak, is near 140 km and has a peak electron density value of ~5 x 10^5 cm^{-3}, very similar to Mariner 5 data (*Bauer and Hartle*, 1974). *Fjeldbo et al.* (1975) used the same data and claimed an abrupt drop in density from 335 km to around 360 km. This signature in the electron density is started to mark the location of the ionopause, which is ~100 km higher than suggested by the *Bauer and Hartle* (1974) interpretation. On the nightside Mariner 10 revealed a double peak electron density profile. The upper peak was located near 140 km with a density ~10^4 cm^{-3} and the lower peak was located near 120 km with a slightly lower density than the upper peak (*Bauer and Hartle*, 1974; *Fjeldbo et al.*, 1975). With some assumptions, *Fjeldbo et al.* (1975) estimated a CO_2 density of 2 x 10^{10} cm^{-3} at 140 km. They also derived an exosphere temperature of 400 K from the plasma scale height; this temperature is similar to the value from the UV spectrometer (*Broadfoot et al.*, 1974).

2.3 Venera Missions/Vega Missions

The Venera missions were designed and executed by the USSR. They often employed the strategy of launching two of the same spacecraft within days of each other and designed both missions to make similar observations. This section will provide short descriptions of the successful Venera missions that made major contributions in understanding Venus' upper atmosphere.

Venera 4 (launched in 1967) was the first successful mission to probe a planetary atmosphere in situ. The probe successfully separated from the spacecraft bus and made measurements for ∼94 minutes in the altitude range of 25-55 km on the nightside. It measured temperature, pressure, wind velocity, and chemical content (CO_2, N_2, and H_2O). The spacecraft bus carried plasma and UV radiation experiments and the bus eventually entered Venus' lower atmosphere and burned up. In roughly 2 years, Venera 5 was launched as a Venus flyby. It carried out the same science on the nightside as did Venera 4. Venera 5 only transmitted for 53 minutes between altitudes 25-55 km. It eventually died at 18 km. A few days after Venera 5, Venera 6 was launched and it too carried out the same science as Venera 4 and 5. The probe transmitted for 51 minutes and died at 18 km. Venera 5 and Venera 6 did find an atmospheric composition of 93-97% CO_2, 2-5% N_2, and less than 4% H_2O.

The probes were proving to be successful and the USSR worked on developing a lander for Venus. Venera 7 (launched August 17, 1970) was the first successful planetary lander. It landed on the nightside of Venus and transmitted for 23 minutes from the surface. It provided a surface temperature measurement of 747 K but no pressure measurements before it failed due to the temperature and pressure. A few years later Venera 8 landed on the dayside of Venus and returned information on atmospheric temperatures, pressure, wind speed, composition and light levels during the descent. Once on the surface, it transmitted for 50 minutes and measured a surface temperature of 734 K, a pressure of 93 bar, and light levels similar to an overcast day on Earth.

The next Venera series focused on the combination of an orbiter and lander, where the orbiter served as a relay for the lander. On October 22 1975, Venera 9 became the first orbiter of Venus and the lander mission provided the first pictures from the surface. The lander operated on the dayside and transmitted for 53 minutes. The lander measured atmospheric composition, structure, and photometry on the descent and obtained black and white images from the surface. The orbiter returned images, IR-radiometry, spectrometry, photopolarimetry, radio occultation, and plasma data.

Venera 10 arrived at Venus a few days after Venera 9 having the same design and suite of instruments. Between the two missions, the lower boundary of the clouds was discovered and the structure of the clouds was examined and better defined. The lower boundary was identified at 49 km and there were 3 distinct cloud layers at altitudes of 57-70 km, 52-57 km, and 49-52 km. Both 9 and 10 observed O_2 Herzberg II nightglow at visible wavelengths (400-800 nm) for the first time on Venus (*Krasnopolsky*, 1983, and references within). The integrated intensity, for solar minimum, was 2.7 kilo-Rayleighs (kR $= 10^{10}$ photons cm^{-2} s^{-1} into 4π sr) in an altitude range of $\sim$90 to 115 km. This nightglow will be discussed further in the Pioneer Venus section of this chapter.

A few years after Venera 9 and 10, Venera 11 performed a flyby and released a lander, which descended on the dayside. It measured atmospheric temperature, pressure, wind velocity, spectra of short wavelength radiation, chemical and isotope composition, and aerosols. The surface imaging and analysis system failed. The lander transmitted for 95 minutes on the surface. The flyby bus carried a UV spectrometer, plasma instruments, and relayed communications from the lander. Venera

12 was the same design and provided the same science as Venera 11, except the science also measured cloud particle composition. The surface imaging failed on Venera 12 too. It transmitted for 110 minutes and was cut off because the flyby bus went below the horizon.

Venera 13 was a flyby/lander combination and arrived at Venus on March 1, 1982. The lander descended on the dayside ∼4 years after Venera 12. It performed atmospheric and cloud science experiments and provided both black and white and colored images of the surface. The surface analysis found leucite basalt, which is rare on Earth. In total the lander survived 127 minutes. Venera 14 was the same design and science as Venera 13. It landed a few days after Venera 13 and its surface analysis found tholeiitic basalt which is similar to the mid-ocean ridge on Earth. The lander survived for 63 minutes.

Thereafter, the USSR returned to orbiter missions. Venera 15 arrived on October 10, 1983 and orbited Venus for 8 months. It returned radar images of the planet from 30N to the north pole at 1-2 km resolution. There was an IR spectrometer onboard to examine the middle atmosphere and clouds. Venera 16 followed Venera 15 within a few days. It was the same mission as Venera 15 and it used the same radar mapper over the same areas with the same resolution. Unfortunately the Venera 16 IR instrument failed.

The last USSR Venus missions were Vega 1 and Vega 2, a triple combination (each) of flyby, lander, and balloon. Vega 1's destination was Halley's Comet. During the flyby it deployed an entry vehicle that positioned the balloon and lander on the nightside. During the descent, the lander obtained atmospheric measurements and the balloon was released. The lander conducted very little surface analysis because the x-ray fluorescence instrument failed. The balloon floated for 48 hours over approximately 10,000 km at an altitude of 54 km. It measured downdrafts of 1 m s^{-1} and average horizontal winds of 69 m s^{-1}. The Vega 2 mission had similar results as the Vega 1 mission. The surface analysis did show evidences of anorthosite-troctolite, which is seen in the lunar highlands but very rare on Earth. The Vega 2 flyby bus continued on to Halley's Comet as well.

The USSR carried out a very extensive suite of observations over a couple of decades. America had sent a few key missions as well. A few of them have already been discussed (Mariner 5 and Mariner 10) but the biggest American Venus missions during this time period were the Pioneer Venus missions. These missions (orbiter and multiporbe) arrived at Venus between Venera 10 and Venera 11. The next section will go into more detail about the missions and the actual data retrieved.

2.4 Pioneer Venus Missions

The Pioneer Venus (PV) missions together comprised one of the longest lasting missions to Venus. It consisted of two missions; an orbiter (PVO) mission and a multiprobe (PVM) mission. In this section there will be a brief description of the missions' orbital information and experiments. Subsequently, the upper atmospheric science that was discovered will be discussed.

PVO was launched on May 20, 1978 and inserted into orbit around Venus on December 4, 1978. The spacecraft carried 12 instruments and performed 17 experiments, which are all listed in Table 2.2. The mission lasted a total of 14 years, when originally only planned for 243 days. PVO had an orbital period of 24 hours with an inclination 105° (75° retrograde). The periapsis distance varied over the entire mission. From insertion to July 1980, the periapsis was held between 142 km and 253 km to make radar and ionospheric measurements. Thereafter, it was raised to 2290 km and allowed to fall to conserve fuel until the final phase of the mission. The final phase of the mission started in May of 1992 and the periapsis was held in the range of 150 km and 250 km. This was done till the orbiter ran out of fuel and was destroyed by atmospheric entry in August 1992. More information about the orbit parameters is given by *Colin and Hall* (1977), *Colin and Hunten* (1977), and *Colin* (1980).

Table 2.2: Pioneer Venus Orbiter Mission Payload

Instrument	Experiment
Orbiter Neutral Mass Spectrometer (ONMS)	- To determine the composition of the upper atmosphere
Orbiter Ion Mass Spectrometer (OIMS)	- To characterize the ionospheric ion population
Orbiter Retarding Potential Analyzer (ORPA)	- To study ionospheric particles
Orbiter Electron Temperature Probe (OETP)	- To study the thermal properties of the ionosphere
Orbiter UltraViolet Spectrometer (OUVS)	- To measure scattered and emitted UV light
Orbiter solar wind Plasma Analyzer (OPA)	- To measure properties of the solar wind
Orbiter MAGnetometer (OMAG)	- To characterize the magnetic field at Venus
Orbiter Infrared Radiometer (OIR)	- To measure the IR emissions from the atmosphere
Orbiter Cloud PhotoPolarimeter/imager (OCPP)	- To measure the vertical distribution of the clouds
Orbiter RADar altimeter (ORAD)	- To determine topography and surface characteristics
Orbiter Electric Field Detector (OEFD)	- To study the solar wind and its interactions
Orbiter Gamma Burst Detector (OGBD)	- To record gamma ray burst events
S-band and X-band radio signals - Orbiter Celestial Mechanics (OCM)	- To determine the gravity field of Venus (2 experiments)
S-band and X-band radio signals - Orbiter Radio Occultation (ORO)	- To characterize the atmosphere
S-band and X-band radio signals - Orbiter Atmospheric Drag (OAD)	- To study the upper atmosphere
S-band and X-band radio signals - Orbiter TURbulence (OTUR)	- To measure the intensity variation of turbulence with altitude and the distribution of scale sizes in the atmosphere

The mulitprobe (PVM) mission consisted of a bus carrying one large probe and three identical small probes. The large probe detached from the bus on November 16, 1978 and the three small probes detached on November 20, 1978. A few days after the release of the small probes and after the bus reoriented itself, the bus aimed for Venus on a shallow entry angle.

The large probe entered on the dayside of the planet near the equator. It took about 1.5 hours to descend through the atmosphere. It had seven instruments and eight experiments all shown in Table 2.3.

Table 2.3: Pioneer Venus Large Probe Payload

Instrument	Experiment
Large Neutral Mass Spectrometer (LNMS)	- To measure the atmospheric composition
Large Gas Chromatograph (LGC)	- To measure the atmospheric composition
Large Solar Flux Radiometer (LSFR)	- To measure solar flux penetration in the atmosphere
Large Infrared Radiometer (LIR)	- To measure distribution of infrared radiation
Large Cloud Particle size Spectrometer (LCPS)	- To measure particle size and shape
Large Nephelometer (LN)	- To search for cloud particles
Radio signals - Differential very-Long Baseline Interferometer (DLBI)	- To infer upper limits on winds speeds in the lower atmosphere
Temperature sensor, pressure sensor, and accelerometer - Large Atmospheric Structure (LAS)	- To measure temperature, pressure, and acceleration to construct a profile of atmosphere state properties; to determine vertical wind velocity, horizontal wind velocity, and turbulence

The small probes were named corresponding to their landing areas; North probe, Night probe, and Day probe. The North probe entered on the nightside around 60°N and the Night probe entered on the nightside around 30°S. The Day probe landed on the dayside around 30°S and was the only probe to continue transmitting information after impact and did so for over an hour. Each small probe had the same three instruments and five experiments listed in Table 2.4.

The bus carried two spectrometers; the Bus Ion Mass Spectrometer (BIMS) and the Bus Neutral Mass Spectrometer (BNMS). The BIMS provided information about the solar wind interaction with Venus, upper atmosphere photochemistry, and the mass and heat transport characteristics of the atmosphere. The BNMS provided information on the upper atmosphere neutral densities, on the origin and evolution of Venus' atmosphere, on the present energy balance and the dynamics of the upper atmosphere, and on the interaction of the upper atmosphere with the solar radiation and the interplanetary medium. These measurements continued until the bus over heated from atmospheric entry at around 165 km.

Table 2.4: Pioneer Venus Small Probes Payload

Instrument	Experiment
Small Neutral Mass Spectrometer (SNMS)	- To measure the atmospheric composition
Small Net Flux Radiometer (SNFR)	- To measure solar flux penetration in the atmosphere
Small Nephelometer (SN)	- To search for cloud particles
Radio signals - Differential very-Long Baseline Interferometer (DLBI)	- To infer upper limits on winds speeds in the lower atmosphere
Temperature sensor, pressure sensor, and accelerometer - Small Atmospheric Structure (SAS)	- To measure temperature, pressure, and acceleration to construct a profile of atmosphere state properties; to determine vertical wind velocity, horizontal wind velocity, and turbulence

2.4.1 Understanding of the Thermal Structure

Venus' thermal structure from the cloud tops to ~100 km was observed by PV with three different techniques; PVO infrared radiometry (*Taylor et al.*, 1980), PVO radio occultations (*Kliore and Patel*, 1980), and in situ measurements by PVM (*Seiff and Kirk*, 1982). The three probes measured similar temperature profiles below 100 km. At 60 km, the common temperature was ~260 K and the temperature decreased to ~180 K near 100 km. Above 100 km, the three probe profiles diverge. The Night probe decreases to ~120 K near 120 km and the Day probe increased to ~210 K near 120 km. The temperature profiles obtained from infrared radiometry and radio occultation were slightly different, due to the sampling locations. However, they were in agreement with the probe data within ~10 K (*Seiff*, 1983). *Taylor et al.* (1979) stated that Venus' middle atmosphere, 70 km - ~90km, is generally warmer in the higher latitudes than at the low latitudes. If middle atmosphere temperatures were maintained by solar heating, the equator would be warmer than the higher latitudes. Hence, high latitude warming may be the result of dynamics controlling the temperatures. Within these observations, the diurnal variations were less than the temporal variations (*Taylor et al.*, 1979, 1980; *Seiff*, 1983). The significant variability gave rise to the question of the presence of waves in the atmosphere.

Above 100 km, the temperature structure is much different. Two techniques were used to gather temperature data above 100 km. One utilized the orbiter atmospheric drag (OAD) measurements, and monitored the decay of the orbiter's orbit (*Keating et al.*, 1979b,c, 1980). The second measured species number density using two neutral spectrometers: a) the bus (BNMS) which sampled at a single local Venus time (*von Zahn et al.*, 1979, 1980); b) the Orbiter Neutral Mass Spectrometer (ONMS) which obtained data at all local solar times near 16°N (*Niemann et al.*, 1979, 1980). With these two techniques, two astonishing features where discovered. Venus' exosphere temperature is observed to be very low when compared to Earth. Dayside observations produced values around 300 K, which were much cooler than previous observations from atmospheric species' emissions (400 K). By contrast, on Earth, the exosphere temperature is ∼1000 K (*Barth*, 1968; *Rottman and Moos*, 1973; *Strickland*, 1973; *Kumar and Broadfoot*, 1975; *Anderson*, 1976; *Gombosi*, 1998). The second astonishing feature is the strong diurnal variation. On the dayside, above the cloud tops, the temperature generally increases with height to exospheric temperatures around 300 K, while on the nightside above the cloud tops the temperature decreases to an exospheric temperature of ∼100 - 120 K (*Keating et al.*, 1979a; *Schubert et al.*, 1980). *Keating et al.* (1979a) and *Schubert et al.* (1980) named the unusually cold nightside thermosphere a "cryosphere". Possible reasons for the observed cryosphere were a combination of radiative cooling and the long Venus day and night period. A detailed summary of PV's findings of the thermal structure can be found in *Seiff* (1983).

2.4.2 Understanding of the Neutral Gas Composition

The neutral atmosphere was mainly observed by ONMS (above 140 km). Data for major species (CO_2, CO, N_2, O_2, O, NO, and He) are described and illustrated in *Niemann et al.* (1980). Variations are seen throughout the data, especially diurnal variations. The density distribution for a given altitude is greatest on the dayside and is smallest at night, due to the very cold nightside atmosphere. This strong diurnal distribution is mainly seen in heavier species such as CO_2, O, CO, N_2, and N. The distribution across the dayside is symmetrical. For the lighter species, such as He and H, the distribution is reversed; the maximum build up is on the nightside instead of the dayside. The lighter species are subject to thermospheric transport. For example at 170 km, atomic O and CO_2 peak around noon ($\sim 10^9$ cm^{-3} and $\sim 10^8$ cm^{-3}, respectively) and display a minimum near midnight ($\sim 5 \times 10^7$ cm^{-3} and $\sim 10^6$ cm^{-3}, respectively). Conversely, He at 170 km shows a minimum ($\sim 10^6$ cm^{-3}) at noon and peaks around 0300 local time ($\sim 5 \times 10^7$ cm^{-3}). See figures 17 and 18 in *von Zahn et al.* (1983) for a more complete distribution from dayside to nightside. The shift in the He peak on the nightside suggests the presence of the superrotating zonal winds at higher altitudes and not just at the cloud tops.

With the vast information from PVO, there were still gaps in the overall knowledge of the upper atmosphere. Therefore, scientists built models to employ the observations and extrapolate the data to derive a better understanding. These models are known as empirical models and are briefly discussed in this section; however Chapter 3 provides a more thorough explanation. *Niemann et al.* (1980) discusses an empirical model built from PVO data and shows results for mass densities near the equator for noon and midnight in their figure 9. The model is based upon *Hedin et al.* (1977a,b) with a density correction factor of 1.63 employed. An important constraint for numerical models is the O/CO_2 ratio on the dayside. Atomic oxygen is largely produced via dayside photodissociation of CO_2 and subsequent ion-neutral chemical reactions. This ratio is usually taken at the altitude of the dayside (low Solar Zenith Angle (SZA)) ionospheric peak ($\sim$140 km). Since PVO did not make measurements at the altitude of 140 km, the dayside ratio was taken from empirical models based upon PVO data, yielding values from 0.15 to 0.20 depending on the SZA (*von Zahn et al.*, 1980; *Keating et al.*, 1980; *Hedin et al.*, 1983). These values are in agreement with previous measurements before PVO. It is also important to understand how the thermosphere transitions from a well mixed region (homosphere) to a diffusive equilibrium region (heterosphere) across a boundary known as the homopause. BNMS was able to make neutral gas measurements from ~650 km to 130 km. The data provided the only in situ observations of the homopause, where the homopause was calculated using N_2 (He) to be near 136 km (130 km) (*von Zahn et al.*, 1980). Also the data provided information to determine an eddy diffusion coefficient, which is an important variable for models. The processes responsible for atmospheric mixing are too complex to model in detail; therefore atmospheric modelers generally treat atmospheric mixing by parameterizing a diffusion rate known as the eddy diffusion coefficient. Through modeling, *von Zahn et al.* (1980) produced an eddy coefficient K in $cm^2\ s^{-1}$ as [$K = 1.4 \times 10^{13} n^{-1/2}$], where n is the total number density. For more details on the neutral gas composition see *von Zahn et al.* (1983).

2.4.3 Understanding of the Night Airglow

Upper atmospheres of planets emit photons in the UV, Visible and IR regions of the electromagnetic spectrum. These emissions may be classified as airglow, which includes dayglow or nightglow (night airglow), or aurorae. Dayglow is luminosity that arises ultimately from the more or less direct interaction of solar photons and photoelectrons with atmospheric gases during the daytime. Nightglow encompasses emissions that arise from reactions of species that originate on the dayside or are transported from the dayside to the nightside. Aurorae are emissions that arise from the interaction of energetic particles other than photoelectrons with atmospheric gases. The source of these emissions is usually the transition of the excited electronic state of a gas to a lower state, which may or may not be the ground state.

In connection with this dissertation, the nightglow emissions serve as effective tracers for Venus' middle and upper atmosphere global wind system due to their variable peak brightness and horizontal distributions. There are several sources of nightglow detected by missions to Venus. The discussion below addresses four specific nightglow emissions observed by the PV mission.

O_2 Herzberg II (400-800 nm): PVO's star tracker made observations of the O_2 visible night airglow during three observing seasons associated with different parts of the solar cycle; season 16 (F10.7 = 150), season 18 (F10.7 = 200), and season 19 (F10.7 = 240). F10.7 is an index for the 10.7 cm wavelength flux transmitted from the Sun measured at Earth's orbit. This index is often used to serve as a proxy for variable solar EUV-UV fluxes, which are absorbed in the Venus thermosphere. The observations for the three different observing times were binned and averaged to create maps for comparisons with modeling simulations; e.g. the Venus Thermospheric General Circulation Model (VTGCM). These results were shown and described in *Bougher and Borucki* (1994). The maps represented average conditions instead of individual snapshots. The map for season 16 had a range of intensities from 1.5 kR to 3.9 kR for 40°S and 45°N, respectively, with the midnight intensity near 3.3 kR at the equator (*Bougher and Borucki*, 1994). For season 18, the peak intensity ranged from 3.6 to 3.8 kR at 01:00 local time (LT) near the equator (*Bougher and Borucki*, 1994). The last map for season 19 had much higher intensities. Due to minimal coverage at all latitudes the intensity ranged form 4 - 6 kR and was near 00:00-02:00 LT (*Bougher and Borucki*, 1994). The reason for the discrepancy in intensities over these three seasons was attributed to changes in incoming solar radiation (*Bougher and Borucki*, 1994).

NO UV (190 - 270 nm): The NO ultraviolet (UV) airglow was observed by the PVO Ultraviolet Spectrometer (OUVS) during a solar maximum period on the nightside of Venus. NO emits at both the delta (190 - 240 nm) and gamma (225 - 270 nm) bands; with the (0,1) delta band being the strongest. A mean statistical map had been created from observations and suggested the brightest emission patch reached 1.9 ± 0.6 kR slightly south of the equator at 02:00 LT (*Bougher et al.*, 1990; *Stewart et al.*, 1980). Although there is a statistically average bright region for the mean map, the individual scans showed high variability on a day to day basis both spatially and temporally. See figure 2 from *Bougher et al.* (1997). The peak altitude of the emission was calculated to be 115±2 km (*Gérard et al.*, 1981).

Atomic Oxygen (130.4 nm): Pioneer Venus OUVS made observations of atomic oxygen airglow which is produced by the resonance transition between $^3S^0$ and the ground state. This emission brightness is very sensitive to the O/CO_2 ratio in the region of 130 to 250 km and peaks near 155 km at ∼10 kR. It is observed in every observation solar locked on the dayside. *Alexander et al.* (1993) analyzed the observations and explained the important physics in understanding these measurements. The statistically averaged map of the observations showed sharp gradients poleward of ∼30 degrees with respect to local time, which suggested oxygen mixing ratios were a factor of 2.5 higher at the evening terminator than at the morning terminator (*Alexander et al.*, 1993). An explanation suggested by *Alexander et al.* (1993) indicated the averaged map was consistent with asymmetric mixing (as a function of local time) due to breaking waves that originated at cloud levels.

Lyman-α (121.6 nm): H-Lyman-α was observed by Mariner 2, but was consistently observed with the Pioneer Venus OUVS (*Paxton*, 1988; *Paxton et al.*, 1988). These observations help constrain the behavior of H in Venus' upper atmosphere, while providing information on the global circulation. *Paxton* (1985, 1988) and *Paxton et al.* (1988) found an H-bulge past midnight, toward the morning terminator. The consistent post-midnight shift supports a theory of an asymmetrical zonal wind system above 150 km. Lastly, the H-bulge was also sensitive to solar activity; the H-bulge increased in magnitude with a decrease in solar activity.

2.4.4 Understanding of the Ionosphere

The ionized region of the upper atmosphere, the ionosphere, was observed six different ways utilizing six different PVO instruments. These instruments include: Ion Mass Spectrometer (OIMS), Neutral Mass Spectrometer (ONMS), Retarding Potential Analyzer (ORPA), Electron Temperature Probe (OETP), Radio Occultation (ORO), and Plasma Analyzer (OPA) (*Brace and Kliore*, 1991). The ionosphere peak density occurs at the altitude where the optical depth is unity. This peak on the dayside is located near 140 km and as the SZA increases the peak altitude rises and becomes more variable. See figure 10 in *Brace and Kliore* (1991) for the peak altitude with respect to SZA. The nightside ionosphere is unlike the dayside and is more structured and varied greatly from orbit to orbit. The varying nightside ionosphere is maintained and driven by at least two processes: (a) day to nightside ion transport and (b) electron precipitation. The debate as to the relative importance of these two processes continues today (*Fox and Kliore*, 1997; *Schunk and Nagy*, 2009).

The composition of the ionosphere is dependent on altitude and day to night processes. On the dayside above 190 km, O^+ is the major ion while below 190 km ${O_2}^+$ dominates. For most cases H^+ is a major ion on the nightside for higher altitudes. It is interesting to note that ${CO_2}^+$ is a minor ion in a CO_2 dominate atmosphere, owing to the fast ${CO_2}^+ + O \rightarrow {O_2}^+ + CO$ reaction.

The outer boundary of the ionosphere (ionopause) was determined to exhibit an average altitude of ~290 km, which varies with respect to SZA. As the SZA increases, the solar wind pressure decreases enabling the ionopause to extend farther away from the solid body. Although an average altitude was determined, the ionopause position is highly dependent on the solar wind; i.e. there was a range of variability for the ionopause altitude (200 to >3000 km) (*Brace et al.*, 1983). For more details and information about the PV discoveries of the ionosphere see *Brace et al.* (1983) and *Brace and Kliore* (1991) and references within.

2.4.5 Understanding of Gravity Waves

Gravity waves are a suggested source for the deceleration of Venus' zonal flow. There have been very limited observations; however evidence of gravity waves exists in PV probe and OAD data (*Seiff*, 1991), and PV ONMS data (*Kasprzak et al.*, 1988, 1993). *Kasprzak et al.* (1988) examined the PV ONMS data and found wave structures with a wavelength range from 100 to 600 km and the amplitudes varied depending on the molecular weight of the species (He, N, O, N_2, and CO_2). Later, with additional data, they were able to see gravity wave signatures, specifically, in the CO_2 data. The CO_2 data amplitude would grow to at least 120 km - 130 km and then saturation would occur near 140 to 150 km in altitude. Other observation by PV probes and bus were minimal and only able to detect wave perturbations but not characterize them (*Seiff et al.*, 1980; *Seiff*, 1991; *von Zahn et al.*, 1980). Moreover, vertical wavelengths above the cloud tops ($\sim$20 km) and below ($\sim$5-10 km) were deduced from temperature observations (*Taylor et al.*, 1980). Other evidence of waves is visually seen in cloud observations, as briefly discussed in Chapter 1. These waves have been observed with a wide horizontal scale from 100 km to hundreds of km and have periods of 4 to 6 days (*Schubert*, 1983). More details on waves from PV observations are discussed in *Schubert* (1983).

2.5 Ground-based Observations

Ground-based observations complement and augment spacecraft observations. Ground-based observers are able to use different techniques at different wavelengths that are not part of an instrument package on any spacecraft. Furthermore, they can also obtain simultaneous measurements, which can be used for cross-validation with the spacecrafts observations. Most ground-based observations of Venus are focused on the region above the cloud tops and measure winds, nightglow, and specific composition which also contribute to the derivation of temperatures. This section will discuss the ground-based observations and their contributions to the knowledge of Venus' temperatures, winds, and night airglow.

2.5.1 Ground-based Nightside Temperature Observations

Ground-based observations have shown significant variations in nightside temperatures for the 95-100 km region. *Connes et al.* (1979) was one of the first to derive a nightside temperature from their O_2 IR observations with a high-resolution Fourier transform spectrometer. They derived a temperature of 185±15 K for an altitude of ~90 km. *Clancy and Muhleman* (1991) used CO millimeter measurements and observed large variations of the nightside temperature from year-to-year near 95 km (165 - 210 K). Later, the CO millimeter measurements were supplemented with another sampling of nightside temperatures around 95 km (165 - 178 K) by *Clancy et al.* (2003).

Most recently, there has been a collective effort to observe Venus' nightside temperatures in collaboration with the Venus Express mission. *Rengel et al.* (2008) published preliminary sub-millimeter measurements of CO as part of a ground-based observing campaign in support of VEX and MESSENGER. This study compared a single temperature profile from one observation (June 8, 2007) with past nightside temperature profiles and *Bertaux et al.* (2007) profiles. *Bertaux et al.* (2007) observations will be discussed in detail in the VEX section. However they have made stellar occultation measurements with the Spectroscopy for Investigation of Characteristics of the Atmosphere of Venus (SPICAV) instrument. Their measurements show high variability within 95 to 100 km with temperatures ranging from ~185 K to 240 K. The *Rengel et al.* (2008) measurement of ~185 K at 100 km is consistent with the lower range of *Bertaux et al.* (2007)'s observations. *Clancy et al.* (2008) also performed sub-millimeter line measurements of CO in support of the VEX and

MESSENGER ground-based observation campaign. Over four days (June 2, June 3, June 6, and June 11, 2007) of observations, *Clancy et al.* (2008)'s limb profiles near the equator at 20:30 LT show temperatures ranging from 170 - 175 K near 100 km. These temperatures are much cooler than those of *Rengel et al.* (2008) and *Bertaux et al.* (2007). *Clancy et al.* (2008) suggests the temperature increase is caused by a diurnal radiative balance, while *Bertaux et al.* (2007) suggests the localized warming is due to localized compressional heating from the downwelling of the day to night circulation.

Bailey et al. (2008) created nightside temperature maps from O_2 ($a^1\Delta_g$) airglow observations with the Anglo-Australian Telescope. Their results also show night-to-night variations. For three days in July 2004, the intensity weighted mean temperature ranged from 195 to 196 K at $\sim$97km. During three other days in December 2005, the intensity weighted mean temperature varied from 181 to 190 K at $\sim$97 km. *Bailey et al.* (2008) provides a summary of available nightside temperature measurements at $\sim$95 km, which has been adapted in this study as shown in Table 2.5. Furthermore, *Ohtsuki et al.* (2005) and *Ohtsuki et al.* (2008) derived nightside temperatures from O_2 IR nightglow. They observed temperatures ranging from $\sim$183 - $\sim$193 K near 95 km. Both, *Bailey et al.* (2008) and *Ohtsuki et al.* (2008), observe a correlation between the nightside warm layer and the peak O_2 IR nightglow. They make rough estimates of the vertical velocities needed to produce the warm area; *Bailey et al.* (2008) calculate -0.2 m s^{-1} and *Ohtsuki et al.* (2008) calculate -0.05 m s^{-1}. Both measurements are comparable to *Bertaux et al.* (2007) observations leading them to the same conclusion; the nightside temperature enhancement is due to localized compressional heating of downwelling gas from the global thermospheric circulation. With these observations, a climatology encompassing the variability of the nightside temperatures in the upper mesosphere can be assembled.

Table 2.5: Summary of temperature measurements for the Venus nightside near 95 km from *Bailey et al.* (2008)

Method	Temperature (K)	Reference
1.27 μm O_2 airglow	185 ± 15	*Connes et al.* (1979)
Pioneer Venus night probe deceleration	167.2	*Seiff and Kirk* (1982)
Pioneer Venus OIR	170 - 175	*Schofield and Taylor* (1983)
VIRA (based on OIR and probe deceleration)	168	*Seiff et al.* (1985)
CO mm lines	165 - 210	*Clancy and Muhleman* (1991)
1.27 μm O_2 airglow	186 ± 6	*Crisp et al.* (1996)
CO mm lines	165 - 178	*Clancy et al.* (2003)
1.27 μm O_2 airglow	193 ± 9	*Ohtsuki et al.* (2005)
Venera 15 IR Fourier spectrometer	166.4	*Zasova et al.* (2006)
SPICAV Stellar occultation	194 - 240	*Bertaux et al.* (2007)
Sub-millimeter observations with HHSMT	∼160 - 200	*Rengel et al.* (2008)
Sub-millimeter observations with JCMT	∼175 - 180	*Clancy et al.* (2008)
1.27 μm O_2 airglow (intensity weighted mean)	181 - 196	*Bailey et al.* (2008)

2.5.2 Ground-based Wind Observations

Ground-based wind measurements have been made using several different techniques; CO_2 10-μm infrared heterodyne spectroscopy, CO J(1-0) millimeter measurements, CO emission lines at 4.7 μm V(1-0) and V(2-1) and visible observations of reflected solar Frauenhofer lines. Only a few observations will be discussed in this section. Table 2.5.2 summarizes all the ground-based observations. The table was adapted from Table 1 in *Lellouch et al.* (1997) and Tables 2.1 and 2.2 in *Sornig* (2009).

Goldstein et al. (1991) observed (December 1985 and March 1987) absolute wind velocities near 110±10 km altitude using the CO_2 10-μm infrared heterodyne spectroscopy technique. The observations provided a SS-AS circulation near 120±30 m s^{-1} along with a small superimposed RSZ wind component of 25±15 m s^{-1}. More recently, *Sornig et al.* (2008) used the same technique in 2007 and made observations at the equator and at higher latitudes. At the equator, there was a small RSZ wind presence (3 ± 7 m s^{-1}) while there were stronger zonal winds at higher latitudes (32 ± 4 m s^{-1}). They also retrieved a smaller SS-AS wind (52 ± 18 m s^{-1}) compared to previous measurements by *Goldstein et al.* (1991). At slightly lower altitudes (∼99 km) CO J(1-0) millimeter measurements were used during late April and early May 1988 by *Shah et al.* (1991). At these times, strong RSZ wind speeds of $\sim130\pm10$ m s^{-1} were dominant, while the SS-AS wind was very small. Other observations have been made, specifically by the CO lines at 4.7 μm at the V(1-0) and V(2-1) bands (*Maillard et al.*, 1995). *Clancy et al.* (2008) used CO mm measurements to derive zonal winds. Due to their geometry, they were unable to separate the RSZ and SS-AS component, but derived zonal winds of 195 ± 70 and 235 ± 70 m s^{-1}. The last type of method used to measure the winds of Venus from Earth is the visible Fraunhofer line scattering by Venus' cloud tops, which *Widemann et al.* (2008) used to make measurements at the equator and near 68 km. Their mean velocity, averaged over four days, of the zonal winds at the cloud tops was 104 ± 10 m s^{-1}. This velocity is consistent with UV cloud tracking measurements.

Furthermore, it can be discerned from Table 2.5.2 that there are very weak trends, if any at all. By looking at the cloud tops (60 - 70 km), an average zonal wind velocity is ∼100 m s^{-1}. Examining the altitude range of ∼100 to 105 km, both RSZ and SS-AS winds have very wide ranges from just being present to ∼130 m s^{-1} and ∼300 m s^{-1}, respectively. At 110 km, the general trend is the RSZ winds are present but are usually weak, while the SS-AS winds are ∼120 m s^{-1}. This provides strong evidence of Venus' highly varying winds and complex dynamics between ∼70 km and 110 km. Wind measurements are important to help constrain global circulation models which help to provide a better overall understanding of Venus' upper atmosphere. More information on ground-based wind measurements can be found in *Lellouch et al.* (1997) and within the references listed in Table 2.5.2.

Table 2.6: Ground-based equatorial wind measurements adapted from *Lellouch et al.* (1997) and *Sornig* (2009)

Alt. (km)	Date	Wind Velocity Zonal[a] (SS-AS)[b] (m s^{-1})	Method	Reference
66	1/03	66±5 - 91±6	Visible/solar rad.	*Gabsi et al.* (2008)
67	7/07	151±16	Visible/solar rad.	*Gaulme et al.* (2008)
68	6/07	92±14 - 155±39[d]	Visible/solar rad.	*Widemann et al.* (2008)
68	8/07	104±20[d]	Visible/solar rad.	*Widemann et al.* (2008)
74	2001, 2002	83±27[d]	Visible/CO$_2$	*Widemann et al.* (2007)
74	2001, 2002	67±21[e]	Visible/solar rad.	*Widemann et al.* (2007)
∼70 - 80	4-5/77	94±6 (-35±6[c])	10 μm heterodyne	*Goldstein* (1989)
∼100	2-4/77, 1978	(Present)	CO mm.	*Gulkis et al.* (1977); *Schloerb et al.* (1980)
∼90-105	1977 - 1982	Weak (Present)	CO mm	*Clancy and Muhleman* (1985)
∼90 - 105	3/85, 588, 2/90	Weak (Present)	CO mm	*Clancy and Muhleman* (1991)
∼90 - 105	12/86, 4-5/88	Strong	CO mm	*Gurwell et al.* (1995)
99±6	4-5/88	132±10 (≤40)	CO mm	*Shah et al.* (1991)
94.5±6	8/91	35±15 (45±15)	CO mm	*Lellouch et al.* (1994)
102	6/07	131±13 - 147±3[f] (290±44 - 322±25[f])	CO mm	*Lellouch et al.* (2008)
102	6/07	46±19 - 63±10[g] (114±41 - 151±19[g])	CO mm	*Lellouch et al.* (2008)
102	8/07	-30±53 - 120±36[f] (55±53 - 120±36[f])	CO mm	*Lellouch et al.* (2008)
102	8/06	40±30 - 120±90[fg] (40±45 - 110±25[fg])	CO mm	*Lellouch et al.* (2008)

---

[a] Zonal retrograde flow, equatorial velocity

[b] Subsolar-to-anti-solar flow, cross terminator velocity

[c] Anti-solar-to-subsolar

[d] Equatorial mean zonal winds

[e] Higher latitudes

[f] Nightside

[g] Dayside

[h] Combined RSZ and SS-AS

Table 2.7: Ground-based equatorial wind measurements continued from Table 2.6.

Alt. (km)	Date	Wind Velocity Zonal[a] (SS-AS)[b] (m s^{-1})	Method	Reference
103	6/07	195±70, 235±70[efgh]	CO mm	*Clancy et al.* (2008)
105±9	8/91	95±10 (90±15)	CO mm	*Lellouch et al.* (1994)
∼90-105	8/91	Equal Magnitude	CO mm	*Lellouch et al.* (1994)
∼90-105	5-6/93	SS-AS moderately stronger	CO mm	*Rosenqvist et al.* (1995)
94.5±6	11/94	45±30 (50±35)	CO mm	*Rosenqvist et al.* (1995)
105±9	11/94	75±20 (110±20)	CO mm	*Rosenqvist et al.* (1995)
109±10	12/85, 10/86, 3/87	25±15 (120±20)	10 μm CO$_2$ heterodyne	*Goldstein et al.* (1991)
110	1990	40±3 (119±2)	10 μm CO$_2$ heterodyne	*Schmülling et al.* (2000)
110	1991	35±1 (129±1)	10 μm CO$_2$ heterodyne	*Schmülling et al.* (2000)
110	6/07	68 - 280[g]	CO mm	*Rengel et al.* (2008)
110	6/07	205 - 355[f]	CO mm	*Rengel et al.* (2008)
110	2007	3±7 (52±18)	10 μm CO$_2$ heterodyne	*Sornig et al.* (2008)
110	2007	18±4 - 32±4[e]	10 μm CO$_2$ heterodyne	*Sornig et al.* (2008)
∼95-110	7-10/91, 3-5/93	Variable	O$_2$ IR nightglow	*Crisp et al.* (1996)
∼100-110	9/94	Veq + 0.7 x Vter = 140 ± 45	CO 5 μm, winds	*Maillard et al.* (1995)
∼125-145	9/94	Veq + 0.7 x Vter = 200 ± 50	CO 5 μm, winds	*Maillard et al.* (1995)

---

[a] Zonal retrograde flow, equatorial velocity

[b] Subsolar-to-anti-solar flow, cross terminator velocity

[c] Anti-solar-to-subsolar

[d] Equatorial mean zonal winds

[e] Higher latitudes

[f] Nightside

[g] Dayside

[h] Combined RSZ and SS-AS

2.5.3 Ground-based CO Observations

Early observations by *Gulkis et al.* (1977) and *Schloerb et al.* (1980) with CO millimeter measurements discovered variations in the CO mixing ratio; specifically, the mixing ratio was larger on the nightside above ∼100 km. At ∼80 - 85 km altitude, the day-to-night variation was a factor of 10. This variation supported the existence of a SS-AS flow modeled by *Dickinson and Ridley* (1975, 1977). *Clancy and Muhleman* (1991) did an extensive study and found (during 1985 - 1986) the nightside CO bulge to vary by a factor of 4 above ∼86 km altitude. However, measurements from microwave spectra resulted in the CO mixing ratio varying by 1 - 2 orders of magnitude above ∼86 km and near 03:00 LT. *Gurwell et al.* (1995) also made extensive observations of the CO variation. They created maps of the CO mixing ratio at 90 km, 95 km, and 100 km altitude and showed a consistent 3 hour shift in the CO nightside peak; the measured mixing ratios were greater than 10^{-4} with sharp drop offs near the terminators. *Gurwell et al.* (1995) claims to have a bulge-to-late morning ratio of CO abundance to be between 20 - 30 near 100 km. More recently, *Clancy et al.* (2003) and *Clancy et al.* (2008) have provided more CO mixing ratio observations. They measured increase day-to-night variations at altitudes of 90-100 km by factors of 2 - 5 (*Clancy et al.*, 2003). Once again, between 85 - 95 km altitude, the CO mixing ratios varied 30-50% from the afternoon (13:30-16:30 LT) to evening (17:30 - 22:30 LT) (*Clancy et al.*, 2008). More details will be discussed in comparison to the Venus Thermospheric Circulation Model's results in Chapter 4.

2.5.4 Ground-based Airglow Observations

Ground-based observations are only able to observe the strongest emissions, and are usually limited to the O_2 IR (1.27μm) emission. The O_2 IR airglow was discovered by *Connes et al.* (1979) with a Fourier Transform Spectrometer. Total intensities, after removal of backscatter from the clouds, were determined to be 1.5 MegaRayleigh

(MR = 10^{12} photons cm^{-2} s^{-1} into 4π sr) for the dayside and 1.2 MR for the nightside. This emission is produced by the three-body recombination of two oxygen atoms and carbon dioxide. These O atoms are transported by the global thermospheric circulation from the dayside to the nightside. Observational campaigns continued with different telescopes and had similar conclusions (e.g. *Allen et al.* (1992); *Crisp et al.* (1996)). The O_2 IR nightglow displayed variations in the emission rates; spatially (up to a factor of 4) and temporally (up to a factor of 6). The intensity had a maximum up to 6 MR and was broadly distributed from near midnight to the early morning (01:00 to 03:00 LT). Most recently, *Bailey et al.* (2008) and *Ohtsuki et al.* (2005, 2008) have made observations of O_2 IR airglow in connection with temperature estimates. *Bailey et al.* (2008) observed an airglow peak near midnight or shifted towards the morning terminator. The peak emission rate ranged from 1.5 MR to 4.8 MR. *Ohtsuki et al.* (2005, 2008) made measurements of the O_2 IR airglow distribution near midnight with a maximum intensity of 5 MR. However, the distributions changed dramatically from day to day as *Crisp et al.* (1996) had indicated.

In addition to the O_2 IR airglow, *Krasnopolsky* (2010) observed the OH IR nightglow for the first time from the ground. He observed the (1-0) P1(4.5) at 2.8 μm and (2-1) Q1(1.5) at 2.94 μm nightglow lines. The observed slant intensities at 21:30 LT were 7.2±1.8 kR and <1.4 kR, respectively. Furthermore, at 04:00 LT the intensities were 15.5±2 kR and 4.7±1 kR, respectively. Both of these OH IR nightglow emissions peaked near 100 km.

To conclude, ground-based observations will be discussed in comparison with VT-GCM results in Chapter 4. As mentioned previously, ground-based observations are used to complement spacecraft observations and help constrain modeling efforts for a complete study and understanding of the dynamics in Venus' upper atmosphere.

2.6 Venus Express Mission

Venus Express (VEX) mission is operated by the European Space Agency (ESA). The orbiter was launched on November 9, 2005 and was placed into orbit around Venus on April 11, 2006. Originally, the mission was for two Venus days (∼500 Earth days) but has been extended until December 31, 2012. VEX has a high inclination elliptical orbit with a 24 hour period. The inclination is ∼90° with a periapsis altitude of 250 km and an apoapsis altitude of 66,000 km. The periapsis latitude is 80°S, near the south pole. VEX carries seven instruments listed in Table 2.8.

New VEX observations have begun augmenting the previous Venus upper atmosphere observations with measurements of key nightglow distributions (e.g., NO, O_2) and vertical structure measurements, both contributing to a growing climatology of the inferred SS-AS and RSZ wind components and their variations (*Bougher et al.*, 2006; *Svedhem et al.*, 2009).

There are two specific instruments on VEX that focus on upper atmosphere measurements (i.e. nightglow, temperature, composition): Spectroscopy for Investigation of Characteristics of the Atmosphere of Venus (SPICAV) and Visible and InfraRed Thermal Imaging Spectrometer (VIRTIS). SPICAV is an instrument with three different spectrometers; UV (110 - 310 nm), VIS-IR (0.7 - 1.7 μm), and Solar Occultation IR (SOIR) (2.2 - 4.3 μm). The SPICAV UV spectrometer provides airglow (nadir and limb) observations of NO (190-270 nm) emissions, which contribute to creating statistical maps. Furthermore, SPICAV provides repeated measurements of vertical profiles of atmospheric density (and inferred temperatures) over ∼80-180 km (dayside) and ∼80-150 km (nightside) via stellar and solar occultations (*Bertaux et al.*, 2007). VIRTIS is an imaging spectrometer with three channels: VIRTIS-M-VIS (imager; 0.3 - 1 μm), VIRTIS-M-IR (imager; 1 - 5 μm), and VIRTIS-H (high-resolution; 2 - 5 μm). Its observations address upper atmosphere dynamics by: (1) measuring the 3-D temperature and derived thermal wind fields (∼60-90 km) on the nightside,

Table 2.8: Venus Express Mission Payload

Instrument	Experiment
Analyser of Space Plasmas and Energetic Atoms (ASPERA-4)	- Studies energetic neutral atoms, ions and electrons
Magnetometer (MAG)	- Makes measurements of magnetic field strength and direction
Planetary Fourier Spectrometer (PFS)	- An infrared spectrometer that operates in the 0.9 μm to 45 μum wavelength range and is designed to perform vertical optical sounding
Spectroscopy for Investigation of Characteristics of the Atmosphere of Venus (SPICAV)	- An imaging spectrometer for UV and IR radiation.
Solar Occultation at Infrared (SOIR)	- Part of the SPICAV instrument; observes the Sun through Venus' atmosphere at IR wavelengths
Venus Radio Science (VeRa)	- A radio sounding experiment that is used to examine the ionosphere, atmosphere, and surface of Venus
Visible and Infrared Thermal Imaging Spectrometer (VIRTIS)	- An imaging spectrometer that operates in the near UV, VIS, and IR parts of the electromagnetic spectrum (0.25 to 5 μm)
Venus Monitoring Camera (VMC)	- A wide angle, multi-channel CCD camera that, using four narrow band filters, operates in the UV, VIS, and near IR.

and (2) mapping the O_2 IR nightglow as a tracer of the wind system over ~90 to 130 km. Repeated measurements over several orbits provide a monitor of the IR nightglow variability at different time scales (*Drossart et al.*, 2007).

2.6.1 VEX Temperature Observations

An important diagnostic for upper atmosphere dynamics is the thermal structure, which is being revealed by VEX. A distinctly warm layer on the nightside (~100 km) has been discovered by stellar occultation measurements with the SPICAV instrument (*Bertaux et al.*, 2007). The SPICAV observations suggest the temperatures between 95 and 100 km are highly variable, with an observed temperature range of ~185 K to ~240 K. *Bertaux et al.* (2007) also deduced vertical velocities on the nightside to be near -0.43 m s^{-1}. These authors state that continued measurements are needed to establish a climatology of these temperatures and confirm a representative mean value in this nightside altitude region.

The Venus Express Radio Science (VeRa) observations provide temperature profiles and temperature maps of the mesosphere (above ~50 km and below ~90 km) (*Pätzold et al.*, 2007). VIRTIS has measured dayside CO_2 Non-Local Thermodynamic Equilibrium (NLTE) emission at 4.3 μm up to 160 km and 2.7 μm up to 130 km, also CO NLTE emission at 4.3 μm up to 120 km (*López-Valverde et al.*, 2007; *Drossart et al.*, 2007; *Gilli et al.*, 2009).

2.6.2 VEX Wind Observations

The cloud morphology is also being monitored by VIRTIS and the Venus Monitoring Camera (VMC) in the UV to help provide more information about the dynamics of Venus' atmosphere. Sequences of images are being used to track the motions of cloud features. Derived wind speeds near the cloud tops (50 - 70 km) can be deduced from the motion of cloud features (*Markiewicz et al.*, 2007; *Moissl et al.*, 2009; *McGouldrick et al.*, 2008; *Sánchez-Lavega et al.*, 2008). The VIRTIS instrument made wind measurements from cloud tracking at three different altitudes layers in the Southern hemisphere. At the cloud tops (~66 km), near the low latitudes, the zonal winds were measured as westward at 105 m s^{-1} and nearly constant with respect to latitude (*Sánchez-Lavega et al.*, 2008). The cloud base (~47 km) winds were measured to be 60 - 70 m s^{-1}. The zonal winds at higher latitudes decreased poleward and values were lower than 15 m s^{-1} (*Sánchez-Lavega et al.*, 2008). The more recent discussion is by *Moissl et al.* (2009) and they use observations from VMC and VIRTIS. *Moissl et al.* (2009) claimed, at latitudes higher than 60°S, winds are difficult to track because of low contrast and scarcity of features. However, they continue to collect data and extend the latitudinal coverage (*Moissl et al.*, 2009).

2.6.3 VEX Night Airglow Observations

VEX has observed three different night airglow emissions (O_2 IR, NO UV, and OH IR). As mentioned previously, night airglows serve as chemical tracers of the global thermospheric circulation. Therefore, understanding the nightglow will aid the characterization of Venus' upper atmosphere global wind system. Furthermore, statistical nightglow distribution maps provide important constraints in modeling Venus' atmospheric dynamics.

Sufficient observations of the O_2 IR night airglow from May 16, 2006 to April 7, 2007 (1225 images) were used to create an averaged statistical map which is presented in *Gérard et al.* (2008c). Their results show that the maximum emission approaches $\sim$3 MR and the mean hemispheric vertical intensity is approximately 1.3 MR. The limb observations indicate a mean production peak for the airglow near 96 km, but the peak altitude can range from $\sim$90 - 110 km. Due to the VEX's trajectory, the southern hemisphere is mainly sampled for the O_2 IR night airglow. Nevertheless, observations discussed earlier strongly indicate the airglow to concentrate near the equator at midnight. Recently, *Soret et al.* (2010a) re-compiled the VIRTIS-M data and merged the nadir and the limb O_2 airglow observations. Their results confirm that the bright spot is statistically centered near midnight on the equator. The O_2 IR nightglow has a maximum local intensity of 1.6 MR and a hemispheric average of 0.47 MR. These values are less than previously published by *Gérard et al.* (2008c), who subtracted a smaller amount of thermal background emission at 1.27 μm from the nadir observations. The mean value for the O peak density derived from the Abel inversion of the O_2 emission limb profiles is about 2 x 10^{11} cm^{-3} with a mean altitude of 103 - 104 km (*Gérard et al.*, 2009b; *Soret et al.*, 2010a). Individual limb profiles revealed the O density peak altitude to range between 95 - 115 km and the density peak to vary between 1 - 5 x 10^{11} cm^{-3}.

Alternatively, *Piccioni et al.* (2009) used VIRTIS limb measurements from 42 orbits to study the statistical characteristics of the 1.27 μm emission. From the analyzed retrieved profiles, the peak altitude of the volume emission rate is observed between 95 and 100 km with a mean of 97±2.5 km. This is very similar to *Gérard et al.* (2010) who analyzed 1843 limb profiles and found an average peak brightness along the line of sight of 28±23 MR at 96±2.7 km. From *Piccioni et al.* (2009)'s vertical profiles, they calculated a hemispheric average value for the integrated emission rate to be 0.52 MR. However, the distribution map has a localized peak vertical emission rate of 1.2 MR located at midnight and slightly south of the equator. While the hemispheric average value is very similar to *Soret et al.* (2010a), the localized peak intensity is reduced but within ranges previously observed. Finally, from visually tracking the O_2 IR nightglow brightest features, mean zonal and meridional velocities can be detected (*Hueso et al.*, 2008). These observations of the O_2 IR nightglow provide information about the global circulation in the altitude range of ~90 to 100 km.

Additionally, the NO Ultraviolet (UV) night airglow has been measured by SPICAV and provides information about the global circulation from 95 km to 132 km. At this time, the UV spectrometer has rather limited spatial and temporal coverage compared to the O2 IR data. Statistical mean maps of the NO nightglow are presently being developed (*Cox*, 2010). SPICAV has made limb observations in both the δ (190-240 nm) and γ (225-270 nm) bands. At the time of *Gérard et al.* (2008b)'s paper, only 17 SPICAV orbits and 201 SPICAV limb scans have been obtained providing acceptable NO UV night airglow scans. These orbits already show large fluctuations in emission intensity and location. Early results from nadir observations with SPICAV (*Cox*, 2010) confirm the pattern previously observed at solar maximum with Pioneer Venus, (i.e. the statistically averaged NO UV airglow emission peaks near the equator around 02:00 LT) (*Stewart et al.*, 1980).

VEX observations have begun to characterize the variability of the two (O_2 IR and NO UV) nightglow layers (i.e. both horizontal and vertical distributions) (*Hueso et al.*, 2008; *Gérard et al.*, 2008b,c, 2009a,b, 2010; *Piccioni et al.*, 2008). The O_2 nightglow statistical bright emission has been observed from 95 - 105 km, ranging from 22:00- 01:00 LT, at latitudes from 20°S to 30°N, with corresponding varying vertical intensities 0.5 MR to 3 MR. The NO nightglow has been observed from 95 - 132 km, ranging from 22:00 - 03:00 LT, located at 30°S to 60°N, with varying vertical intensities of 1 - 6 kR. These changes have been seen on very short timescales.

Furthermore, *Gérard et al.* (2009a) have shown the first concurrent observations of the O_2 IR and NO UV night airglow with VIRTIS and SPICAV data. They concluded that the two nightglow emissions are not spatially correlated, giving rise to the idea that each emission is controlled by different dynamical processes (*Collet et al.*, 2010). Recent publications (*Gérard et al.*, 2008b,c, 2009a,b, 2010; *Bertaux et al.*, 2007; *Piccioni et al.*, 2009) detailing observations made by these instruments will be discussed later in comparison with VTGCM results in Chapter 4.

Finally, the OH IR nightglow on Venus was first observed with VIRTIS on VEX by *Piccioni et al.* (2008). The bands of V(1-0) at 2.8 μm, V(2-1) at 2.94 μm, and V(2-0) at 1.43 μm were identified with evidence of additional bands in the Δv = 1 sequence. Due to the weak emission the nightglow is only observed at the limb. The integrated intensity for (1-0) band was 0.88±0.09 MR located at 96±2 km (*Piccioni et al.*, 2008). The data has been studied by *Gérard et al.* (2010) for correlations between the OH (Δv = 1) and the O_2 IR nightglow and then by Soret et al. (2010b) to determine the global distribution of OH (Δv = 1). Gerard et al. (2010) conducted a preliminary study and found an average brightness near 0.41±0.37 MR peaking at 95.3±3 km. A correlation with the O_2 IR nightglow was noted. More recently, *Soret et al.* (2010b) has utilized 3328 limb profiles to find a mean peak of the OH (Δv = 1) emission as $0.35^{+0.53}_{-0.21}$ MR with a location near 96.4±5 km. The intensity is highly variable; it has been observed as low as <20 kR and as high as 2 MR (*Soret et al.*, 2010b). In addition the intensity tends to be higher near the antisolar point rather than towards the poles. *Soret et al.* (2010b) also noted a correlation of the OH IR and the O_2 IR nightglow emissions. This is anticipated since both nightglows production mechanisms are dependent on the same reactant, atomic O, which is created on the dayside and transported to the nightside by the global wind system.

2.6.4 VEX Gravity Wave Observations

Perturbations in density, temperature, and cloud structures are observed by VEX and are thought to be a source of variability in Venus' upper atmosphere. The actual source of these perturbations is unknown; however gravity waves are commonly implicated. Specifically, VIRTIS has detected perturbations in CO_2 NLTE emissions (*Garcia et al.*, 2009). From these observations they are able to obtain wave structures with horizontal wavelengths ranging from 90 - 400 km. Additionally, derived horizontal phase velocities (magnitude and direction) are consistent between orbits and are on average of 70 m s^{-1} westward and 30 m s^{-1} northward (*Garcia et al.*, 2009). *Garcia et al.* (2009) claim these observed waves are generated from the polar vortex. Moreover, VIRTIS and VMC observed visible trains of oscillating cloud brightness in the UV for an upper cloud layer (∼66 km) on the dayside and thermal radiation for the lower cloud layer on the nightside (*Peralta et al.*, 2008). Wavelengths and phase speeds are also derived from these observations. *Peralta et al.* (2008) observe wavelengths of 60 - 150 km, which propagate westward with phase velocities similar to the zonal flow and are confined to horizontal wave packets of 400 to 1800 km. They find no correlation between the waves and surface topography, latitude, LT, or wind structure. The perturbations in the observations help provide information on gravity waves in Venus' atmosphere, which are very important in constraining gravity wave formulations within 3-D models.

2.7 Outstanding Problems and Unresolved Issues

This chapter has briefly discussed the upper atmosphere observations and datasets from Venus missions and ground-based observations. These efforts are translated into modeling constraints. For a three-dimensional model, the unique dayside and nightside constraints are listed in Table 2.9. With this, our knowledge of Venus' upper atmosphere has grown dramatically. However, there are still many unresolved issues to be addressed in future research. The remaining broad upper atmosphere issues are briefly discussed.

The source of variability in the upper atmosphere (thermal and dynamical) is still not well understood. Additionally, what is driving the variations in the RSZ winds, which augment the SS-AS winds? Understanding the RSZ winds would provide insight into the latitudinal distribution of trace species (CO, He, H). How is wave activity, especially gravity waves, impacting the global circulation and temperatures? More observations are needed to characterize the meridional winds; to understand how they change with respect to altitude and how they are impacted by the RSZ winds. Furthermore, for modeling purposes, more information is needed to know if cyclostrophic balance is a good assumption for the mesospheric momentum balance. With the VEX polar orbit, data is becoming available to support the questions about the origin of the "cold collar" inversions and the mechanisms generating the polar dipole structure. Lastly, upper atmosphere modeling is not capable of addressing all these unresolved issues. A few items which could be addressed is the upper boundary and lower boundary conditions. At the upper boundary, the influences of exospheric transport and/or the connection with the solar environment could be investigated. While at the lower boundary, the effects of the lower atmosphere by incorporating gravity wave propagation and/or other wave mechanisms could be examined. Nonetheless, for modeling to address these issues there is a need for more measurements above 100 km (wind, temperature, and composition) to fully develop

Table 2.9: Three-Dimensional modeling constraints from observations

Dayside	**Nightside**
- Atomic oxygen and nitrogen profiles (e.g. O/CO_2 ratio at 140 km)	- Three nightglow emissions: peak intensity and altitude of layers (NO UV, O_2 IR, and OH IR)
- O and N(4S) column production	- O, $N(^4S)$, CO profiles (i.e. peak density and altitude (day-night variation))
- Measured trace specie distribution at low altitudes	- O and $N(^4S)$ column destruction
- Exosphere and 110 km temperatures	- Trace species distribution at low altitudes
- Peak electron density and altitude (SZA variation)	- Nightside cryosphere temperatures
	- Variable warm temperatures near ∼100 km (and vertical velocities)
	- SS-AS and RSZ wind components (time averaged and variability)

the climatology of Venus' upper atmosphere.

Correspondingly, this dissertation aims to address some of these unresolved issues utilizing numerical simulations to contribute to an expanded knowledge of Venus' upper atmosphere. The first issue to be addressed is the variability of the night airglow. More specifically, sensitivity tests will be performed to show how sensitive the NO UV and O_2 IR nightglow emissions are to specific parameters and to understand the connection between the two nightglows. The second issue is the production of the nightside warm spot and the possible sources of its variability, by performing similar sensitivity tests. Lastly, the issue being addressed fundamentally is the impact gravity waves have on the global circulation system; the night airglow distributions and the night warm spot. Furthermore, the understanding of cloud top generation of these gravity waves, their vertical propagation, and their momentum influenced at thermospheric heights.

In summary, the two primary goals are: (1) to benchmark the Venus Thermospheric General Circulation Model against available observations and data sets, and (2) to explore the specific unresolved issues (previously mentioned) with the Venus

Thermospheric General Circulation Model and provide insight into Venus' upper atmosphere dynamics.

To support these two goals, the next chapter (Chapter 3) will discuss the history of modeling Venus' upper atmosphere which has led to the main numerical tool used in this dissertation (Venus Thermospheric General Circulation Model). Chapter 4 will compare modeling results with the most recent observations and examine the specific unresolved issues. Lastly, Chapter 5 will provide the concluding points of this dissertation's work and point the way forward to future research.

CHAPTER III

Numerical Modeling of Venus

3.1 Introduction

Numerical modeling is a tool for atmospheric scientists, more importantly it is an experimental laboratory. This tool is used to gain insight into the important physics controlling an atmospheric system. The next sections will discuss different types of Venus upper atmosphere numerical models which, combined with observations, have lead to the understanding of what is currently known today. Figure 3.1 (adapted from figure 13 in *Bougher* (1985) provides a block diagram of ongoing theoretical modeling of Venus upper atmosphere, and most of them will be briefly discussed in this chapter. The sections will progress through one-dimensional models, two-dimensional models, three-dimensional models, and will finish with a detailed description of the numerical model used in this dissertation.

3.2 One Dimensional Empirical Models

Empirical models are best used to describe a standard atmosphere. They incorporate actual data and then employ extrapolations and spherical harmonics to produce the needed coverage. The empirical models discussed in this section are mostly developed from the data provided by the PVO mission and are still currently used in

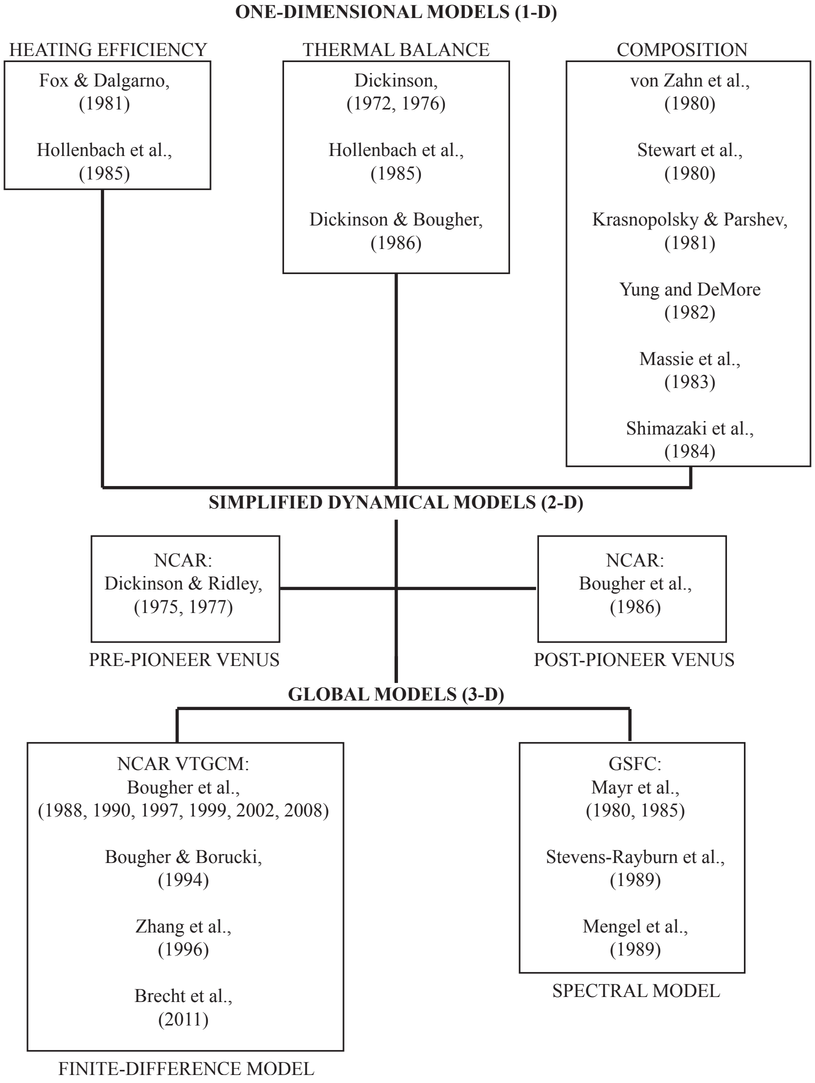

Figure 3.1: Block diagram illustrating previous Venus models which have led to the present three-dimensional model adapted from *Bougher* (1985).

the Venus numerical modeling community.

The Pioneer Venus Orbiter Neutral Mass Spectrometer (PV ONMS) measured gas density and composition in the thermosphere of Venus. The data sets represented nearly three diurnal cycles on Venus. These data were taken from an altitude range of 145 km to 250 km and roughly 16°N latitude. The data were employed to develop a global empirical model of Venus' thermosphere (*Niemann et al.*, 1980; *Hedin et al.*, 1983). The model utilizes a spherical harmonic expansion in local time and latitude, but was limited to five harmonics. The harmonic limitation resulted in inaccurate representation near the terminators where dramatic atmospheric changes from day to night exist. The model extrapolates down to 100 km and goes up to 250 km. It carried six chemical species; CO_2, CO, N_2, O, N, and He. Additional information on vertical profiles was provided by entry probe densities above 100 km (*Seiff et al.*, 1980). Below 180 km, CO_2 and He data was incorporated from the BNMS of *von Zahn et al.* (1980). Temperatures were derived from atomic oxygen scale heights in order to reduce errors from chemical recombination and also temperature gradient effects by limiting the data selected to the altitude range 150 - 250 km (170 - 250 km) for night (day). Model results are represented in *Hedin et al.* (1983), more specifically densities versus altitude for solar maximum conditions (F10.7 = 200) at midnight and noon are represented in *Hedin et al.* (1983) Table 3. When the model was first employed, density values were found to be much smaller than experimental measurements by OAD and BMNS (*Niemann et al.*, 1980; *Keating et al.*, 1980; *von Zahn et al.*, 1980). *Hedin et al.* (1983) claimed the discrepancy between the different observations to be a calibration error with the ONMS data and used an enhancement of 1.6 in the model. *Hedin et al.* (1983)'s version of the model is currently referred to as VTS3. The purpose of these modeling efforts was to represent the average behavior of the data. Overall, VTS3 was able to represent thermospheric observations, specifically the asymmetries, and is still used to this day.

Another empirical model was created by merging a few models together to create the Venus International Reference Atmosphere (VIRA) model, which extends from Venus' surface to 100 km (*Kerzhanovich et al.*, 1983; *Seiff*, 1983; *Schofield and Taylor*, 1983) and from 100 to 250 km (*Keating et al.*, 1985). The lower atmosphere section of VIRA (surface to 100 km) provides information for the lower boundary of upper atmosphere models. The merged models are based upon probe and orbiter data from US and USSR Venus missions, including PVO data from OIR and radio occultations. When the models were merged they had to reconcile temperature differences of ∼10 K and poor vertical resolution of ∼10 km. Latitude effects were found in the data at lower altitudes (∼30 km), thus certain models were used for the "deep atmosphere" and latitude-dependent models were used at higher altitudes (*Seiff et al.*, 1985). For a mean state, VIRA's uncertainties are <5 K below 80 km and <10 K up to 100 km. Even with the mean state, there are variabilities in the middle atmosphere reproduced in the modeling. Variation is observed due to propagating waves and above ∼95 km, diurnal variability is indicated due to the beginning of the strong diurnal differences from the upper atmosphere (*Seiff et al.*, 1985). VIRA is the best empirical representation of Venus lower to middle atmosphere and is still used for comparisons.

The upper atmosphere section of VIRA (100 - 250 km) is based primarily on in situ mass spectrometer and drag measurements and for altitudes with very little data the model is based upon theory and extrapolation (*Keating et al.*, 1985). VIRA was able to reproduce the observed variations with respect to solar zenith angle as well as solar activity (the change in 10.7 cm flux). However, near 100 km, VIRA does not necessarily capture the substantial latitudinal, semidiurnal, and diurnal variations in all of its complexity due to the lack of data. Observations and modeling have proven Venus' temperature and composition to be very sensitive to these variations. For more details on the upper atmosphere section of VIRA, such as comparison tables and figures, see *Keating et al.* (1985).

The empirical models provide insight for Venus' vertical structure, mainly density and temperature variations with respect to altitude. This information is crucial for the beginnings of other modeling and provides a basis for comparison.

3.3 One Dimensional Theoretical Models

One-Dimensional (1-D) modeling is important to examine vertical structure at certain local times. This section will discuss a few 1-D models that made large contributions in understanding the vertical distributions of neutral densities; such as the impacts of eddy diffusion (*von Zahn et al.*, 1980; *Stewart et al.*, 1980; *Massie et al.*, 1983).

von Zahn et al. (1980) created a model to examine the importance of eddy mixing and for comparisons with PV observations. The model was referred to as the morningside (MS) model due to the model addressing the analysis at 60° SZA for the upper atmosphere (100 - 225 km). The MS model was a coupled continuity-diffusion model and predicted densities for several species (CO_2, N_2, CO, O, and He). Overall, the MS model was in agreement with BNMS and OAD observations above 130 km, but for ONMS, the MS model produced higher number densities. The main contribution provided by this model was insight into the eddy diffusion coefficient. The analytical representation of the eddy diffusion coefficient profile was taken from *Lindzen* (1971) as $K = A^*n^{-1/2}$ $cm^2\ s^{-1}$, where n is the total number density (cm^{-3}) and A is a constant chosen to be 1.4×10^{13} $cm^{1/2}\ s^{-1}$. A maximum eddy diffusion coefficient (Kmax) is needed to constrain K, but it is difficult to determine due to the density profiles being insensitive to K once the molecular diffusion coefficient exceeds K. Molecular diffusion describes how individual species diffuse through one another, while eddy diffusion expresses the amount of mixing needed to simulate microphysical turbulence. Thus, 5×10^8 $cm^2\ s^{-1}$ was used at the Kmax. However, when an eddy diffusion coefficient was used independently of density, it provided inadequate calculated compositional profiles when compared to observations. The profiles that agreed with observations, specifically N_2 and He, were used to make individual estimates of the homopause altitude, which was calculated to be 136 km and 130 km, respectively. The homopause altitude is the location where molecular diffusion first becomes more important than eddy diffusion. This information has been proven to be important when seeking model constraints and understanding of the Venus upper atmosphere. However, as stated by *von Zahn et al.* (1980), it is not yet clear whether the eddy diffusion coefficient profile is a signature of small-scale vertical mixing or only a reasonable description of compositional variations brought by a global-scale circulation cell.

In continuation of examining Venus' upper atmosphere vertical structure, *Stewart et al.* (1980) utilized a nightside 1-D chemical diffusive model to solve for the density distributions of CO, N, O, O_2, NO, and O_3. This model is similar to *Rusch and Cravens* (1979) 1-D model, where both range from 70 - 140 km. *Stewart et al.* (1980) compared their 1-D results with OUVS airglow observations of the NO UV delta band emission. This comparison was used to provide constraints on the eddy diffusion coefficient and downward fluxes of the nightside of O and N atoms. The eddy diffusion profile was adopted from *von Zahn et al.* (1980). In order to get the best fit for the observed peak nightglow volume emission rate, the corresponding altitude, and the integrated average intensity over the nightside, the eddy diffusion coefficient was chosen to be $K = 1.4 \text{ x } 10^{13} * n^{-1/2}$ and was constrained with an eddy diffusion maximum of $Kmax = 3 \text{ x } 10^{8}$ cm^2 s^{-1} at 140 km. In addition to the eddy diffusion, the prescribed downward flux was adopted from *Dickinson and Ridley* (1977) as 1 x 10^{12} cm^{-2} s^{-1} for O and 1 x 10^{10} cm^{-2} s^{-1} for N. With these parameters, *Stewart et al.* (1980) were able to discern that the peak NO delta band emission altitude was dependent on the eddy diffusion coefficient and the downward flux of O. Additionally, the actual emission is strongly dependent on the downward flux of N atoms since N and the NO nightglow similarly varied with respect to the eddy diffusion coefficient. Although this is a basic study of the nightside atmosphere, it does constrain the odd-N chemistry and the amount of atomic N needed for transport from the dayside and the amount of vertical mixing needed on the nightside to produce the observations. This information is crucial to launch a more complex study of Venus' upper atmosphere.

In addition to *von Zahn et al.* (1980) and *Stewart et al.* (1980), *Massie et al.* (1983) created two 1-D models; one for the dayside (∼60° SZA) and one for midnight. For the dayside model, ionospheric (*Nagy et al.*, 1980) and neutral chemistry were incorporated along with the adoption of NO, N(^{2}D), N(^{4}S) profiles from *Rusch and Cravens* (1979). The coupling of this chemistry and vertical fluxes by continuity-diffusion equations produced dayside profiles of CO_2, CO, O, N_2, He, and O_2 with a mean homopause location of 134 km. The nightside employed the same equations but specified a downward flux, creating a nightside model similar to *Stewart et al.* (1980). Results of the dayside and nightside modeling are tabulated in tables 3 and 8 of *Massie et al.* (1983). These calculations were helpful in understanding the dayside sources and losses of chemistry in specific regions were major chemical reactions occur. Trace chemical species were found to be important in destroying O and CO below ∼110 km. Moreover, CO_2 was mainly destroyed by photodissociation between 110 - 140 km and provided a source for O and CO. Lastly, the ionospheric chemistry has shown to be most important above 140 km. The chemical analysis comparing the Venus dayside and nightside, which would be important for global modeling, showed the need for two different eddy diffusion coefficients to provide a best fit with the observations. *Massie et al.* (1983) used $K = 1.4 \times 10^{13} * n^{-1/2}$ and $Kmax = 5 \times 10^7$ cm^{-2} s^{-1} for the dayside, while using a stronger coefficient for the nightside; $K = 2 \times 10^{13} * n^{-1/2}$ and $Kmax = 5 \times 10^7$ cm^{-2} s^{-1}. Lastly, the prescribed downward fluxes on the nightside were shown to be imperative to calculate the density profiles, as previously shown in *Stewart et al.* (1980).

The last 1-D model to be briefly described was employed to help understand the global mean temperatures from 90 - 130 km (*Dickinson*, 1972, 1976), unlike the previous compositional models. Specifically, *Dickinson* (1972) built a NLTE radiative transfer model which solved the thermodynamic equation. The NLTE condition exists where collisions between molecules are rare; usually at higher altitudes. This condition has been proven crucial in modeling temperatures in Venus' upper atmosphere since the local thermodynamic equilibrium condition over estimates the 15 μm cooling. *Dickinson* (1972) calculated the sources and sinks of radiative energy in the upper atmosphere where vibrational-rotational bands of CO_2 controlled the infrared absorption and emissions of the equilibrium temperature. These calculations provided detailed 15 μm cooling and infrared heating rates with respect to SZA. However, the EUV heating efficiency and other parameterizations were not well constrained. *Dickinson* (1976) took this opportunity to address these not well constrained parameters and perform sensitivity tests with the heating efficiency, eddy mixing, and collisions of O with CO_2. For instance, he found exospheric temperatures ranging from 250 to 475 K when the EUV heating efficiency varied from 2 - 30%. Conversely, larger eddy mixing impacts the temperatures by cooling. Another sensitivity test resulted in temperatures being lower when atomic O abundances increased in the atmosphere; this enhanced the collisional excitation of CO_2 vibrations and subsequent CO_2 15 μm emission, when NLTE conditions prevailed. With these explicit 1-D heating and cooling calculations, they provided the first global mean temperatures, which were later used in the *Dickinson and Ridley* (1975, 1977) 2-D model.

All of these 1-D models have proven to be valuable in understanding Venus' vertical structure. However, they lack the ability to simulate and understand impacts from dynamical processes such as large scale winds. The 1-D models do show how complex Venus' upper atmosphere can be and the strong need for a more comprehensive, multi-dimensional model.

3.4 Two Dimensional Theoretical Models

Two-dimensional (2-D) modeling provides more complexity when compared to the 1-D models. The 2-D models are able to solve for winds, composition, and temperatures. This section will discuss the main development of the Venus 2-D model, which were first presented by *Dickinson and Ridley* (1977) and later continued by *Dickinson and Bougher* (1986).

Dickinson and Ridley (1977) developed a nonlinear hydrodynamic 2-D model which solved the primitive equations and calculated composition (*Dickinson and Ridley*, 1972; *Dickinson*, 1976; *Dickinson and Ridley*, 1975). The model extended vertically from ∼95 km to 200 km with a $\Delta z = 0.125$ km and the horizontal coordinate was SZA ($\Delta\theta = 5°$). This was a tool to examine the winds, the temperature, and the composition in Venus' mesosphere and thermosphere. The model incorporated three atmospheric constituents (CO_2, CO, and O) and was driven by absorption of solar EUV and UV radiation. It employed routines for radiative transfer and energy and mass transport by the large scale circulation. Small scale transport, such as eddy diffusion, was neglected. *Dickinson and Ridley* (1977) addressed two specific cases. One incorporated a high heating efficiency (100%) and the other used a low heating efficiency (30%). The high (low) case yielded exospheric temperatures >600 K to <250 K (∼300 K to <180 K) for the day to nightside respectively. However, neither case reproduced the observed day-night temperature contrasts, specially the cold nightside temperatures observed by Pioneer Venus. The horizontal winds for these cases were on the order of a few hundred m s^{-1} and did result in dayside depletion and nightside enhancement of atomic O. *Dickinson and Ridley* (1977) addressed the contribution of the large scale dynamics to density and temperature distributions, but the day-night contrasts were much stronger than the actual PVO data revealed.

Dickinson and Bougher (1986) and *Bougher et al.* (1986) used the framework of the *Dickinson and Ridley* (1977) symmetric 2-D model and incorporated upgraded physical processes; i.e. eddy mixing, conduction, 15 μm cooling, and wave drag parameterizations. With this model, they reexamined the circulation and structure of Venus' thermosphere, specifically examining the day-to-night contrasts of temperature and composition. The 2-D model was able to reproduce PVO observations more accurately mainly due to the adoption of the wave drag parameterization and stronger CO_2 15 μm cooling. The drag parameterization was able to weaken the thermospheric circulation system and thereby provide observed day-to-night contrasts in temperatures and composition. The stronger CO_2 15 μm cooling primarily balances solar EUV-UV heating and provides observed temperatures near the exobase and below. *Bougher et al.* (1986) also claimed that eddy diffusion is a minor contributor to the maintenance of day and nightside densities. The eddy diffusion coefficient utilized is much smaller than used previously in 1-D models due to the expanded role of mixing by the global wind system. Overall, Venus' thermospheric mixing is due to small-scale and large-scale dynamical processes.

The 2-D Venus models proved to be valuable in understanding the symmetrical wind system and investigating the impacts the winds have on the thermospheric composition and temperatures. This modeling effort provided an avenue to interpret PVO density and temperature measurements; however, the 2-D model is not capable of representing the asymmetric characteristics also observed by PVO. The 2-D modeling presents a platform for three-dimensional modeling to be employed for the purpose of further understanding of the large-scale dynamics in Venus' upper atmosphere.

3.5 Three-Dimensional General Circulation Models

Three-Dimensional (3-D) modeling provides the capability to globally model an atmosphere. In Venus' case, a 3-D model is necessary to provide a more realistic understanding of the ongoing physical process and how they interact with each other. This section discusses a 3-D spectral transform model which has been developed over time and is used to compare with other 3-D and 2-D models of the Venus upper atmosphere.

In order to examine the upper atmosphere of Venus, *Mayr et al.* (1980)) revised their Earth 3-D spectral transform model for Venus, known as the Goddard Space Flight Center (GSFC) spectral transform model. The GSFC model used Fourier harmonic expansion and vector spherical expansion to produce latitude and local time dependencies; employed as perturbations of a global uniform atmosphere taken from an empirical model (*Niemann et al.*, 1980). They investigated the impact of atmospheric rotation and eddy diffusion upon the global scale diurnal variations of the thermospheric composition. The results were compared to ONMS observations and used to infer information about dynamical properties. The multi-constituent model reproduced the diurnal mode which provides day-night variations of the temperature and the heavier species (CO_2, CO, and O). All chemical species were assumed to be in diffusive equilibrium and the eddy diffusion coefficient was varied parametrically while independent of height ($K = 3 \times 10^7$ cm^2 s^{-1}). Heating and cooling within the model was adopted from *Dickinson* (1972), but was slightly altered to reproduce the observed temperatures. Nonlinear coupling (wind-induced diffusion) was introduced to reproduce the lighter species (He and H) and the smaller asymmetrical signatures in the temperatures. In the tidal model, the higher order modes (P_2^2 and P_3^3) were computed to capture the nonlinear coupling. It was found that a large vertical diffusive mass exchange (eddy diffusion) between the thermosphere and mesosphere is needed to balance the large horizontal advection to produce phases and amplitudes in reasonable agreement with observations; i.e. the dayside O bulge and the small He diurnal variation. Furthermore, to maintain the temperature variations the computed wind velocities were <200 m s^{-1} with a corresponding superrotation of ~50 m s^{-1}

near the equator.

Mayr et al. (1985) continued developing the GSFC spectral transform model (*Mayr et al.*, 1980) to incorporate non-linear processes, higher-order tidal components, and collisional momentum exchange between major species. This development was done to provide insight into diurnal variations in the density, temperature, and wind fields. They reproduced the observed broad dayside densities and the nearly symmetric distributions around the sub-solar point. Moreover, the steep density gradients near the terminators and small difference between dusk and dawn were simulated. The calculated horizontal winds were $\sim$300 m s^{-1} near the terminators and show the winds larger at dusk then dawn, thus resulting in the convergence of the horizontal winds after midnight.

Further development of the GSFC spectral transform model was done by *Stevens-Rayburn et al.* (1989) and *Mengel et al.* (1989). One of the main upgrades was the use of the improved empirical model of *Hedin et al.* (1983) instead of *Niemann et al.* (1980). The other modification was lowering the EUV-UV heating rate efficiency to 20% (*Fox*, 1988) and implementation of Rayleigh friction (as was done by *Bougher et al.*, 1986, which will be discussed in the next section). This permitted slower winds to be simulated, consistent with the observed temperature and major species contrast between day and night. The thermospheric superrotation was found to have little impact on the temperature variation; although it did provide asymmetry in the horizontal winds and impacted the minor species distributions. However, the minor species day-night variations were not well represented until a reduced eddy diffusion coefficient was applied. The diurnal variation in He is dependent on the superrotation rate; i.e. the longer the period, the larger the day to night build up is, along with a shorter time delay of the peak density after midnight. *Mengel et al.* (1989) suggests a period of 6 Earth days best fits the observations. The *Mengel et al.* (1989) model was used in comparison with the National Center for Atmospheric Research (NCAR) model (*Bougher et al.*, 1988) to provide a global interpretation of the most recent observations.

This 3-D modeling effort is a reasonable approach to gain insight into the Venus' upper atmosphere dynamics compared to 1-D and 2-D modeling. This GSFC spectral transform model is able to reproduce asymmetric characteristics observed by PVO. Nevertheless, the model does not solve a total composition equation along with the momentum and thermodynamic equations, but rather utilizes empirical models to prescribe mean composition upon which perturbation values are calculated and total values are finally derived. Therefore, their modeling efforts only provide a diagnostic examination of the observed temperatures, composition, and winds.

3.6 The Three-Dimensional Venus Thermospheric General Circulation Model

The previous modeling sections have led up to the model used for the work in this dissertation. The NCAR Venus Thermospheric General Circulation Model (VTGCM) provides a framework to simulate a global self-consistent upper atmosphere (solves composition equations with the momentum and thermodynamic equations). Observations have suggested asymmetries in composition and airglow, while displaying an extreme change in temperatures from the day to nightside in the thermosphere. Available upper atmosphere data sets imply two wind systems (superrotating zonal wind and subsolar-to-antisolar) and only a 3-D model can properly simulate both these global scale wind components. The main purpose for using this model is to produce simulations that are representative of observations and investigate the underlying processes that maintain and drive variations in Venus' upper atmosphere structure. The next subsections will describe the VTGCM, its numerical formulation, inputs, boundary conditions, and the major chemistry incorporated.

3.6.1 VTGCM Description

The VTGCM is a 3-D, fourth-order, centered finite-difference, hydrodynamic model of the Venus upper atmosphere (e.g. *Bougher et al.*, 1988) which is based on the NCAR terrestrial Thermospheric Ionosphere General Circulation Model (TIGCM). The framework of the NCAR general circulation model is documented in *Washington and Williamson* (1977) and the first developments of the 3-D model were documented in *Dickinson et al.* (1981). The model assumes hydrostatic equilibrium which is a valid approximation for Venus' upper atmosphere due to the lack of sudden intense heating events. The intense heating would produce large vertical velocities, which would create an imbalance between gravity and vertical velocity and resulting in a divergence from the hydrostatic equilibrium assumption (*Deng et al.*, 2008).

VTGCM revisions and improvements have been documented over nearly 2-decades (see *Bougher et al.*, 1988, 1990, 1997, 1999, 2002, 2008; *Bougher and Borucki*, 1994; *Zhang et al.*, 1996; *Brecht et al.*, 2010a,b). The VTGCM code has recently been re-constructed on a new computer platform, the NCAR IBM/SP super computers (*Brecht et al.*, 2007, 2009, 2010a; *Rafkin et al.*, 2007). This new VTGCM code makes efficient use of 4 to 32-processors in a multi-tasking environment. A parallel dynamical solver is implemented, for which assigned 2-D (latitude versus longitude) blocks spanning all altitudes are distributed over the globe (and the processors) to reduce the overall wall clock time for calculations. The VTGCM model has the capability of modeling both hemispheres, instead of mirroring one to the other, enabling small Venus seasonal effects to be simulated. Subroutines from the previous VTGCM code (see review of *Bougher et al.*, 1997) are modified to accommodate the new array structure. The EUV-UV heating, ionization, and dissociation routines are now based on a slant column integration scheme that is optimized; this routine is called every model time-step.

The VTGCM solves the primitive equations for the neutral atmosphere and provides temperatures, major species (CO_2, CO, O, and N_2), several minor species (O_2, $N(^4S)$, $N(^2D)$, and NO) , dayside photochemical ions (CO_2^+, O_2^+, O^+, and NO^+), and the three-component winds (see *Bougher et al.*, 1999). The formulation of the equations will be discussed in the next section. The model covers a 5° by 5° latitude-longitude grid, with 69 evenly-spaced log-pressure levels in the vertical (Z_p = -16 to 18), extending from approximately ~70 to 300 km (~70 to 200 km) at local noon (midnight). The latitudinal points are placed at ±2.5° - ±87.5° in both directions (north and south). Currently, a 30-second time-step is utilized for all new VTGCM simulations to satisfy the Courant-Friedrichs-Lewy (CFL) stability criterion. A double resolution case has been examined; see Section 3.7 for a description and Chapter 4 for the results.

Detailed photochemistry is implemented in the VTGCM in order to address various major and minor species distributions in the Venus upper atmosphere. Dayside O and CO sources arise primarily from CO_2 net dissociation and ion-neutral chemical reactions. The VTGCM ion-neutral chemistry is currently based upon the chemical reactions and rates of *Fox and Sung* (2001), while the electron temperatures are approximated by the *Theis et al.* (1980) empirical model at 60° SZA.

The VTGCM can be used to examine Venus' thermospheric structure and winds from solar maximum to solar minimum EUV-UV flux conditions. Solar fluxes are taken from different sources for different wavelengths (*Torr et al.*, 1979, 1980; *Torr and Torr*, 1985; *Tobiska and Barth*, 1990; *Donnelly and Pope*, 1973; *Nagy et al.*, 1980), see *Dickinson and Bougher* (1986) and *Bougher et al.* (1988) for more details. The EUV and UV heating scheme is based upon *Nagy et al.* (1980). The weighted photoionization and photoabsorption cross sections are also adopted from *Torr et al.* (1979) and now extend from 1 $\mathring{A}$ to 2250 $\mathring{A}$. In addition, the VTGCM is designed to calculate O_2 IR (1.27 μm) and NO UV (δ band 190-290 nm and γ band 225-270 nm) nightglow distributions for comparison with various Venera, PVO, VEX, and ground-based measurements (*Bougher and Borucki*, 1994; *Bougher et al.*, 1990).

Finally, various constants and variables are included such as the reference pressure (P_o= 5 x 10^{-3} μbar at ~130 km), mean gravity (g = 8.4 m s^{-2}), specific heat (C_p) (which is calculated with mixing ratios that change with respect to altitude), molecular viscosity (KM), and thermal conductivity (KT). Molecular viscosity and thermal conductivity for CO and CO_2 correspond to temperatures <300 K and are from the mixed-gas prescription of *Banks and Kockarts* (1973). KT, KM, C_p, and the mean molecular weight are all functions of latitude, local time, and altitude in the thermosphere. Gravity is taken as a constant with the assumption of a shallow atmosphere. The average gravity over the domain is utilized; variations in gravity have been tested and produce very small changes in the model fields.

3.6.2 VTGCM Numerical Formulation

This section will describe the time-dependent primitive equations and the supporting equations. The diagnostic equations (hydrostatic and continuity) will be expressed which solve for Φ (geopotential) and w (vertical motion). Additionally, the prognostic equations (thermodynamic, eastward momentum, northward momentum, and composition) are expressed which solve for steady-state solutions for the temperature, zonal (eastward) velocity, meridional (northward) velocity, and mass mixing ratio of specific species. These formulations have been described in detail by *Bougher et al.* (1988); primed (perturbation) values have now been replaced by total field values. For clarity, a few of the common variables in the upcoming equations are listed.

Z_p = log pressure ($Z_p = \ln(\frac{P_o}{P})$)

P_o = 5 x 10^{-3} μbar (reference pressure)

P = pressure ($P = P_o e^{-Z_p}$)

ϕ = latitude

λ = longitude

h = altitude

f = Coriolis parameter ($2\Omega\sin\phi$; Ω = ~3.23 x 10^{-7} rad s^{-1})

Φ = geopotential

T = temperature (K)

r = radius of Venus (6.05 x 10^6 m)

u = zonal velocity (m s^{-1})

v = meridional velocity (m s^{-1})

w = vertical motion in the log-pressure vertical coordinate system (dz/dt)

g = acceleration of mean gravity (8.4 m s^{-2})

C_p = specific heat at constant pressure (mean = 0.85 J K^{-1} g^{-1})

KT = thermal conductivity (mean ∼1.85 x 10^{-2} J m^{-1} K^{-1} s^{-1}

KM = molecular viscosity (mean ∼14 kg m^{-1} s^{-1})

S = static stability ($\frac{dT_o}{dz} + \frac{RT_o}{C_p m}$)

H = mean pressure scale height (mean ranges 3000 - 5000 m)

R = universal gas constant (8.314 x 10^{15} J K^{-1} mol^{-1})

m = mean molecular weight (mean value ∼30 kg $kmole^{-1}$)

Q = heat source (K Day^{-1})

C = 15 μm cooling (K Day^{-1})

The hydrostatic balance within the VTGCM is enforced by using the geopotential, Φ, and is given by

$$\frac{\partial \Phi}{\partial Z_p} = \frac{RT}{m} \tag{3.1}$$

Moreover,

$$d\Phi = g dh \tag{3.2}$$

where dh is the change in height. The mean bottom of the model is set at 70 km.

The continuity equation becomes a diagnostic relationship for models with constant pressure-based vertical coordinates. It is given by:

$$\frac{1}{r\cos\phi}\frac{\partial}{\partial\phi}(v\cos\phi) + \frac{1}{r\cos\phi}\frac{\partial u}{\partial\lambda} + e^{Z_p}\frac{\partial}{\partial Z_p}(e^{-Z_p}w) = 0 \tag{3.3}$$

.

The VTGCM calculates atmospheric composition by solving the composition equations for mass mixing ratios, Ψ. The major species composition equation is given by:

$$\frac{\partial\Psi}{\partial t} = \underbrace{-e^{Z_p}\tau^{-1}\frac{\partial}{\partial Z_p}[\frac{m}{m_{CO_2}}(\frac{T_{00}}{T})^{0.25}\alpha^{-1}L\Psi]}_{1} + \underbrace{e^{Z_p}\frac{\partial}{\partial Z_p}(\frac{K(Z_p)e^{-Z_p}}{H^2}\frac{\partial\Psi}{\partial Z_p})}_{2} - \underbrace{(\mathbf{V}_h\cdot\nabla_h\Psi + w\frac{\partial\Psi}{\partial Z_p})}_{3} + \underbrace{S - R}_{4} \qquad (3.4)$$

where the terms on the right hand side are: (1) molecular diffusion, (2) eddy diffusion, (3) advection terms, (4) chemical sources and losses.

In the composition equation τ is the diffusion time scale = 9.25 x 10^3 s appropriate to Venus, m_{CO_2} is the molecular weight of CO_2, T_{00} is a reference temperature (273 K) at the characteristic CO_2 scale height (6.14 km), $K(Z_p)$ is the eddy coefficient, α represents a matrix that varies as the inverse of the diffusion coefficients with i = 1, 2, and 3 corresponding to O, CO, and CO_2 (see equations 7 to 11 of *Dickinson and Ridley* (1975) for more details), and L is a matrix operator that is diagonal with elements given by equations 10 and 11 of *Dickinson and Ridley* (1975). The term $\mathbf{V}_h \cdot\nabla_h$ represents the horizontal advection term $(\frac{u}{r\cos\phi}\frac{d}{d\lambda} + \frac{v}{r}\frac{d}{d\phi})$. The last two terms represent chemical sources, S, and chemical losses, R.

The next equations are the momentum equations; zonal (eastward), meridional (northward), and vertical. The zonal momentum equation arises as:

$$\frac{\partial u}{\partial t} = \underbrace{\frac{ge^{Z_p}}{P_o}\frac{\partial}{\partial Z_p}(\frac{K_M}{H}\frac{\partial u}{\partial Z_p})}_{1} + \underbrace{\frac{uv}{r}\tan\phi}_{2} + \underbrace{fv}_{3} - \underbrace{[\mathbf{V}_h\cdot\nabla_h u + w\frac{\partial u}{\partial Z_p}]}_{4} - \underbrace{\frac{1}{r\cos\phi}\frac{\partial\Phi}{\partial\lambda}}_{5} - \underbrace{F_{drag}}_{6} \qquad (3.5)$$

While the meridional momentum equation is given as:

$$\frac{\partial v}{\partial t} = \underbrace{\frac{ge^{Z_p}}{P_o}\frac{\partial}{\partial Z_p}(\frac{K_M}{H}\frac{\partial v}{\partial Z_p})}_{1} - \underbrace{\frac{u^2}{r}\tan\phi}_{2} - \underbrace{fu}_{3} - \underbrace{[\mathbf{V}_h \cdot \nabla_h v + w\frac{\partial v}{\partial Z_p}]}_{4} - \underbrace{\frac{1}{r}\frac{\partial \Phi}{\partial \lambda}}_{5} - \underbrace{F_{drag}}_{6} \tag{3.6}$$

where the terms on the right hand side for both zonal and meridional momentum equations are as follows: (1) molecular diffusion, (2) curvature term, (3) Coriolis term, (4) horizontal and vertical advection, (5) geopotential gradient force, (6) wave drag.

The wave drag term will be discussed throughout the dissertation; however Rayleigh friction is adopted to parameterize wave drag which is thought to result from gravity wave momentum deposition. In particular, $\mathrm{F}_{drag} = \lambda_{RF}$ (u - u_{SR}) where $\lambda_{RF} = 0.5$ x 10^{-4} s^{-1} and u_{SR} is the specified zonal wind speed to approximate the superrotation retrograde zonal wind. The maximum u_{SR} value is set to 75 m s^{-1}. Both the maximum λ_{RF} term and the maximum u_{SR} are specified with an exponential profile; more details are discussed in section 3.6.3.

Due to the VTGCM being a hydrostatic model, the vertical velocity is a diagnostic variable. Instead, horizontal (zonal and meridional) winds are calculated by first solving the zonal and meridional momentum equations and then forcing the divergence of the 3D velocity to be zero ($\nabla \cdot \mathbf{u} = 0$), where $\mathbf{u}$ = (u, v, w) is the velocity. Then by integrating the continuity equation in the vertical direction, the vertical motion w is calculated with units of s^{-1}. In order to finally calculate the vertical velocity, w must be multiplied by the atmospheric scale height, H, to have units of m s^{-1}.

Finally the last remaining equation is the thermodynamic equation.

$$\frac{\partial T}{\partial t} = \underbrace{\frac{ge^{Z_p}}{P_oC_p}\frac{\partial}{\partial Z_p}(\frac{K_T}{H}\frac{\partial T}{\partial Z_p})}_{1} + \underbrace{\frac{ge^{Z_p}}{P_oC_p}\frac{\partial}{\partial Z_p}(K(Z_p)C_p\rho(\frac{1}{H}\frac{\partial T}{\partial Z_p} + \frac{g}{C_p}))}_{2} -$$

$$\underbrace{w(S+\frac{RT}{C_pm}+\frac{\partial T}{\partial Z_p})}_{3}-\underbrace{[\mathbf{V}_h\cdot\nabla_h T]}_{4}+\underbrace{\frac{Q}{C_p}}_{5}-\underbrace{\frac{C}{C_p}}_{6} \tag{3.7}$$

where the terms on the right hand side are as follows: (1) molecular thermal conduction, (2) eddy conduction, (3) adiabatic heating and cooling and vertical advection, (4) horizontal advection, (5) IR, EUV, and UV heating, (6) CO_2 15-μm cooling (which is temperature dependent) (*Bougher et al.*, 1999).

For a more detailed mathematical explanation of the governing equations, see *Bougher* (1985) and *Bell* (2008).

The associated boundary conditions are as follows. The top boundary assumes $\frac{dT}{dz} = 0$, $\frac{du}{dz} = \frac{dv}{dz} = \frac{dw}{dz} = 0$ and the composition is in diffusive equilibrium, thus $L\Psi = 0$. The bottom boundary presently assumes all winds are zero and a temperature value of 230 K is prescribed. Both the wind and temperature bottom boundary can be modified consistently to represent available observations. A return flow (night to day) is neglected thus $\Psi_o = 0$ and $\Psi_{co} = 5.8 \times 10^{-5}$ and N_2 is calculated as a simple diffusive equilibrium constituent above Z_p=0. The mass mixing ratio for CO_2 is derived by $\Psi_{co_2} = 1.0 - \Psi_{co} - \Psi_o - \Psi_{n_2}$. The minor species are set according to global averaged values given by *Yung and Demore* (1982) and the ions are in photochemical equilibrium. The leap-frog scheme is chosen for the temporal discretization.

Moreover, the preceding equations require filtering to maintain stability. There are two spatial filters and one temporal filter used within the VTGCM. The first spatial filter is a Fourier filter, which focuses on the polar regions. Near the poles, with a uniform latitude and longitude grid, the grid cells become extremely small and would require a much smaller time-step than presently prescribed (5° = 30 s). Therefore, filtering of shorter wavelength fast moving waves of the prognostic variables in the polar region by Fourier analysis prevents linear instability ($C\Delta t/\Delta x \leq 1$) when using a 30 second time-step. *Williamson and Browning* (1973) tested this method for the shallow water equations, while the tables from *Williamson* (1976) provide the maximum retained longitudinal wavenumber for prognostic variables for different grid sizes. This filter is applied to all prognostic fields at each time-step. The second spatial filter is used to keep the model from developing small-scale noise in the prognostic fields and is based on *Shapiro* (1970). The *Shapiro* (1970) filter is 4th order in the zonal and meridional directions. It is applied to all the prognostic fields and utilizes a smoother constant of 3.0 x 10^{-2}; see *Williamson et al.* (1977) for the formulation. Lastly, the VTGCM includes a temporal filter to control time tendency (used at each time step) and the time computational mode of the leap-frog time stepping scheme (used at time nΔt after the values are computed at time (n+1)Δt). The filter is originally designed by *Robert* (1966) and later studied by *Asselin* (1972). The filter parameter "alpha" utilized is 0.025. Moreover, the filter is only applied to the prognostic variables (T, u, v, and composition fields).

An instability is typically produced by the CO_2 15 μm cooling parameterization due to the strong forcing (*Bougher et al.*, 1988). Previously, the nonlinear temperature dependent 15 μm cooling term was split into two terms (explicit = right hand side and implicit = left hand side) and utilized a 300 second time-step. Now a smaller (30 second) time-step is employed, enabling total CO_2 15 μm cooling to be captured as an explicit term on the right hand side of the thermodynamic equation.

3.6.3 VTGCM Implementation

Formulations for CO_2 15 μm cooling, wave drag, and eddy diffusion are incorporated into the VTGCM (see *Bougher et al.*, 1999, 2008). CO_2 15 μm emission is known to be enhanced by collisions with O-atoms, providing increased cooling in NLTE regions of the upper atmosphere (see *Bougher and Borucki*, 1994; *Bougher et al.*, 1997; *Kasprzak et al.*, 1997). The corresponding collisional relaxation rate adopted for typical benchmark VTGCM simulations is 3 x 10^{-12} cm^3 s^{-1} at 300 K

(*Bougher et al.*, 1999, 2008). This value provides strong CO_2 15 μm cooling that is consistent with the use of EUV-UV heating efficiencies of ∼20-22%, which are in agreement with detailed offline heating efficiency calculations of *Fox* (1988).

Sub-grid scale processes (i.e. eddy diffusion, viscosity, conduction, and wave drag) are not self-consistently formulated in the VTGCM, but rather parameterized using standard aeronomical formulations. For instance, Rayleigh friction is typically used to mimic wave-drag effects on the mean flow. Figure 3.2 is a profile of the prescribed zonal wind (u_{SR}), which is utilized in the formulation of the wave drag term within the VTGCM and Figure 4.20 (Chapter 4) is a longitude-altitude cross section of the calculated wave drag term at the fixed altitude of 2.5°N. For symmetrical winds, the maximum drag is ∼0.012 m s^{-2} near 135 km at the terminators. Rayleigh friction provides a target for comparison to future gravity wave momentum drag schemes applied to Venus' upper atmosphere. Gravity wave drag formulations have been used to simulate possible activity in Venus' atmosphere (*Zhang et al.*, 1996); new gravity wave parameters derived from VEX observations will help constrain these formulations (*McGouldrick and Toon*, 2008; *Peralta et al.*, 2008; *Sánchez-Lavega et al.*, 2008). For more detail on the Rayleigh friction and gravity wave drag formulations see *Bougher et al.* (1988).

The eddy diffusion coefficient is prescribed in the form $K = A^*n^{-1/2}$ with units of cm^2 s^{-1} where n is the total number density and A is a constant estimated to be 6.0 x 10^{12} $cm^{1/2}$ s^{-1} for the nightside (*von Zahn et al.*, 1979). The nightside eddy diffusion has a maximum of 1 x 10^7 cm^2 s^{-1} and the dayside has a constant eddy diffusion coefficient for the entire upper atmosphere of 1 x 10^6 cm^2 s^{-1}.

The research done for this dissertation includes the following upgrades shown in Table 3.1. These upgrades will be discussed through the remainder of Chapter 3 and the corresponding science will be discussed in Chapter 4. The most recent VTGCM model changes are crucial to properly reproduce VEX observations. The

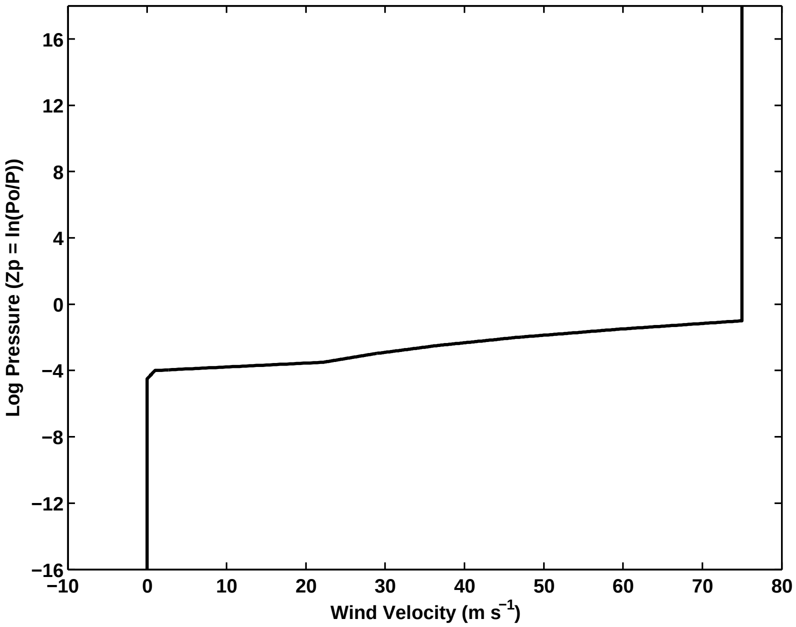

Figure 3.2: The prescribed RSZ (m s^{-1}) wind in the VTGCM as a function of log pressure ($Z_p = \ln(P_o/P)$).

VTGCM lower boundary is now extended downward and the upper boundary is extended upward. The altitude range at local noon currently spans ~70 km to 300 km. This ensures that all the dynamical influences contributing to the NO UV and O_2 IR nightglow layers can be captured. "Exact" (line-by-line radiative transfer model) CO_2 15 μm cooling rates for a given temperature and composition profile are taken from *Roldán et al.* (2000); cooling rates for the simulated VTGCM temperatures and species abundances are calculated (from these exact rates) based upon a slight modification of the parameterization scheme described previously (e.g. *Bougher et al.*, 1986). The near-IR heating term is incorporated using offline simulated look-up tables, updated recently using *Roldán et al.* (2000) rates. The most noticeable improvement from adding the new IR rates is found in the doubling of the 4.3 μm heating around 120 km on the dayside.

Table 3.1: The VTGCM upgrades completed for this dissertation.

- Lowered bottom boundary extended from ∼95km to ∼70km and the upper boundary extended to ∼200 km on nightside; to insure all dynamical influences contributing to the NO and O_2nightglow layers can be captured
- Applied new near-IR heating and CO_2 15-micron cooling rates (*Roldán et al.*, 2000); upgraded 4.3 μm heating
- Implemented both solar photo-dissociation and photoelectron dissociation of N_2 (provided by J.-C. Gérard)
- Updated chemical reaction rates
- Added trace species to the nightside by extracting profiles from *Krasnopolsky* (2010) (Cl, Cl_2, ClCO, ClO, H_2, HCl, HO_2, O_3, OH)
- Incorporated flexible Resolution: 2.5° x 2.5° and 0.25 vertical or 5° x 5° and 0.5 vertical
- Implemented a gravity wave momentum drag scheme based upon the *Fritts and Lu* (1993) scheme for a preliminary study

3.6.4 NO UV Nightglow and N-production

The NO UV nightglow emission and N-atom production have been updated with the application of solar photo-dissociation and photoelectron dissociation rates of N_2 for solar minimum or maximum conditions, based upon detailed 1-D model simulations by *Gérard et al.* (2008a). In these calculations, the cross sections for the N_2 dissociation by solar UV photons are obtained as the difference between the total absorption and the ionization cross sections. High resolution cross sections and predissociation probabilities are needed to quantitatively model the production of atomic nitrogen. *Fox et al.* (2008) have stated this to be important for the highly structured regions of the N_2 photoabsorption spectrum shortward of the ionization threshold at 79.6 nm where predissociation and autoionization compete. Currently high resolution cross sections are being measured and predissociation lifetimes are being calculated. Even with this progress there is still insufficient information (e.g. branching ratios) to compute the production rates of atomic nitrogen or the total photodissociation rate of N_2 (*Fox et al.*, 2008). Instead, the use of lower resolution solar fluxes and cross sections can provide accuracy to a "factor of only a few" (*Fox et al.*, 2008). More accurate rates are presently approximated within the VTGCM by tripling the rates calculated for large wavelength bins (low resolution). These new N-production rates provide proper chemical sources of atomic nitrogen on the dayside coupled with transport to the nightside to produce the NO UV night airglow.

3.6.5 Updated Airglow Chemistry

Another VTGCM modification involves updates of the airglow chemistry with recent reaction rates and yields. Illustrated in Figure 3.3 are sources and sinks for atomic oxygen on the dayside. The selected reactions are listed in order of decreasing importance for atomic oxygen production:

$$CO_2 + h\nu \rightarrow CO + O \tag{RK1}$$

$$O_2^+ + e \rightarrow O + O \tag{R7}$$

$$CO_2^+ + e \rightarrow CO + O \tag{R8}$$

$$O_2 + h\nu \rightarrow O + O \tag{RK2}$$

There are two altitude regions where O is produced. The production peaks for reactions RK1 and RK2 are near 110 km, while reactions R7 and R8 peak near 140 km. The two different altitude source regions are important for the production of the O_2 IR night airglow and the NO UV nightglow, respectively.

Figure 3.4 illustrates the chemical processes, sources and sinks, controlling the dayside atomic nitrogen abundance (*Bougher et al.*, 1990). The main sources of atomic nitrogen come from photo-dissociation and photo-electron impact of molecular

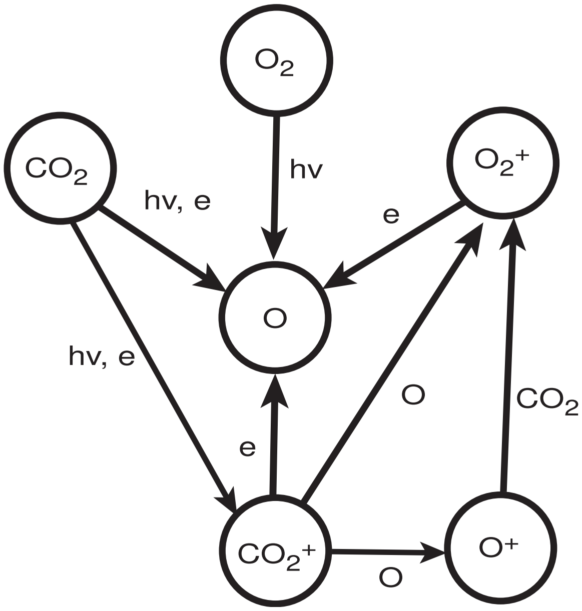

Figure 3.3: VTGCM simplified dayside odd oxygen chemical scheme. This provides the sources for atomic O which is transported to the nightside to produce the O_2 IR and NO UV night airglow emissions.

nitrogen (see section 3.6.4). These reactions can supply both ground state and excited atomic nitrogen, N(^{4}S) and N(^{2}D), respectively. The branching ratio used for N(^{2}D) is f=0.5 (*Bougher et al.*, 1990). There are four selected reactions that regulate dayside atomic nitrogen, plus N(^{2}D) quenching by atomic oxygen and carbon monoxide:

$$N(^2D) + CO_2 \rightarrow NO + CO \tag{R10}$$

$$N(^4S) + O_2^+ \rightarrow NO^+ + O \tag{R14}$$

$$NO + N(^4S) \rightarrow N_2 + O \tag{R15}$$

$$NO^+ + e \rightarrow gN(^2D) + (1-g)N(^4S) \tag{R20}$$

The dissociative recombination of NO$^+$ also supplies ground state and excited atomic nitrogen species; thus a branching ratio of g=0.75 is used for N(^{2}D) (*Bougher et al.*, 1990). The dayside atomic nitrogen production peak is located near the ionospheric peak at 140 km.

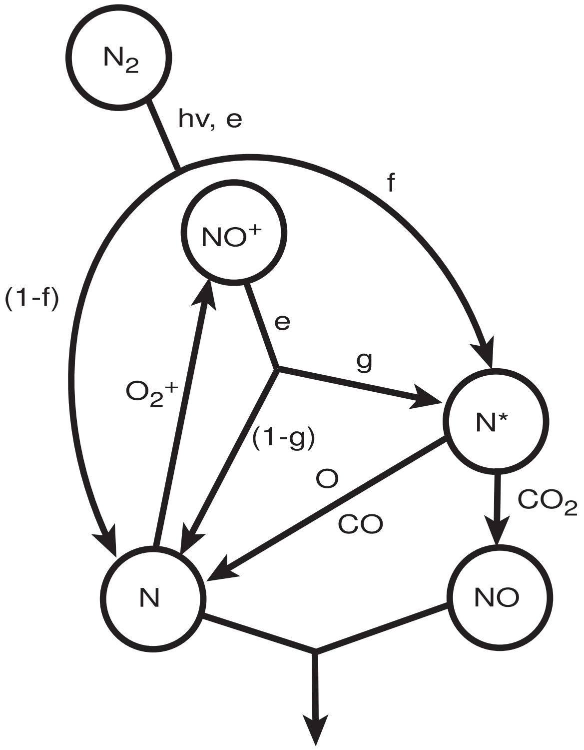

Figure 3.4: VTGCM simplified dayside odd nitrogen chemical scheme. Taken from *Bougher et al.* (1990).

The two dayside produced atomic species, nitrogen and oxygen, are subject to transport by the global thermospheric circulation. Upwelling occurs on the dayside with strong cross terminator horizontal flow and downwelling on the nightside. These species follow the global circulation streamlines to the nightside at different altitudes. The stream lines closely follow constant pressure surfaces. Therefore, the streamlines decrease in altitude from day to night due to the colder nightside temperatures and downwelling of the converging global circulation. The main chemical reaction for O_2 IR night airglow production and the main chemical loss of atomic oxygen on the nightside (above ∼90 km) is:

$$O + O + CO_2 \rightarrow O_2^* + M \qquad \text{(R1)}$$

where a yield of 75% is typically utilized (e.g. *Gérard et al.* (2008c)) for the O_2 IR production. There are other estimated yields, such as *Crisp et al.* (1996), which are based on laboratory studies. They found yields of 0.63 ± 0.19 for $M = N_2$ and ~0.6-0.75 for $M = CO_2$. Another estimated yield was presented by *Huestis* (2002); values of 0.94 - 0.99 were generated for $M = N_2$ and $M = CO_2$ by combining laboratory studies and atmospheric studies. The formulation for the O_2 ($^1\Delta$) 1.27 μm emission is retained from *Bougher and Borucki* (1994). The main chemical loss on the nightside for N(^{4}S) and the main chemical reaction for production of the NO UV night airglow is:

$$N(^4S) + O \rightarrow NO^* \tag{R16}$$

Reaction R16 provides emissions for both delta and gamma bands. This reaction competes strongly with reaction R15.

$$N(^4S) + NO \rightarrow N_2 + O \tag{R15}$$

For a summary of all the reactions, reaction rates, and yields used within the VTGCM for atomic oxygen and atomic nitrogen see Table 3.2.

Table 3.2: Key O_2 IR and NO UV nightglow parameters. Rate coefficients are cm^3 sec^{-1} and three body rate coefficients are cm^6 sec^{-1}

	$O + O + CO_2 \rightarrow O_2$(a state)	75% yield	*Gérard et al.* (2008c)
R1	$O + O + CO_2 \rightarrow O_2$(a state)	2.75×10^{-32}	*Gérard et al.* (2008b)
R2	O_2(a state) + $CO_2 \rightarrow O_2 + CO_2$	2×10^{-20}	*Sander and et al.* (2003)
R3	$O + CO + CO_2 \rightarrow 2CO_2$	$6.5 \times 10^{-33} \times \exp(-2180/Tn)$	*Yung and Demore* (1982)
R4	$O + O_2 + CO_2 \rightarrow O_3 + CO_2$	1.35×10^{-33}	*Yung and Demore* (1982)
R5	$CO_2^+ + O \rightarrow O^+ + CO_2$	9.60×10^{-11}	*Fox and Sung* (2001)
R6	$CO_2^+ + O \rightarrow O_2^+ + CO$	1.64×10^{-10}	*Fox and Sung* (2001)
R7	$O_2^+ + e \rightarrow O + O$	$1.95 \times 10^{-7} \times (300/Te)^{0.7}$	*Mehr and Biondi* (1969)
R8	$CO_2^+ + e \rightarrow CO + O$	$3.5 \times 10^{-7} \times (300/Te)^{0.5}$	*Fox and Sung* (2001)
R9	$O^+ + CO_2 \rightarrow O_2^+ + CO$	1.10×10^{-09}	*Fox and Sung* (2001)
	f	0.5 branching ratio	*Bougher et al.* (1990)
	g	0.75 branching ratio	*Bougher et al.* (1990)
R10	$N(^2D) + CO_2 \rightarrow NO + CO$	2.8×10^{-13}	*Bougher et al.* (1990)
R11	$N(^2D) + O \rightarrow N(^4S) + O$	$2.0\text{x}10^{-11}$	*Bougher et al.* (1990)
R12	$N(^2D) + CO \rightarrow N(^4S) + CO$	$1.9\text{x}10^{-12}$	*Fox and Sung* (2001)
R13	$N(^2D) + N_2 \rightarrow N(^4S) + N_2$	1.7×10^{-14}	*Fox and Sung* (2001)
R14	$N(^4S) + O_2^+ \rightarrow NO^+ + O$	1.00×10^{-10}	*Fox and Sung* (2001)
R15	$N(^4S) + NO \rightarrow N_2 + O$	$2.5 \times 10^{-10}\ (Tn/300)^{0.5}\ \exp(-600/Tn)$	*Fox* (1994)
R16	$N(^4S) + O \rightarrow NO^* + h\nu$	$1.9 \times 10^{-17}\ (300/Tn)^{0.5}\ (1-0.57/Tn^{0.5})$	*Dalgarno et al.* (1992)
R17	$N(^4S) + O + CO_2 \rightarrow NO + CO_2$	$1.83 \times 10^{-32}\ (298/Tn)^{0.5}$	*Campbell and Thrush* (1966)
R18	$N_2 + O^+ \rightarrow NO^+ + N$	$1.2 \times 10^{-12}\ (300/Tn)^{0.45}$	*Fox and Sung* (2001)
R19	$NO + O_2^+ \rightarrow NO^+ + O_2$	4.50×10^{-10}	*Fox and Sung* (2001)
R20	$NO^+ + e \rightarrow g\ N(^2D) + (1-g)\ N(^4S)$	$4.0 \times 10^{-7}\ (300/Te)^{0.5}$	*Fox and Sung* (2001)
RK1	$CO_2 + h\nu \rightarrow CO + O$		Computed in the VTGCM
RK2	$O_2 + h\nu \rightarrow O + O$		Computed in the VTGCM
RK3	$N_2 + h\nu \rightarrow (1-f)\ N(^4S) + f\ N(^2D)$		Computed in the VTGCM

3.6.6 Re-evaluated Chemical Rate Coefficients

In this section two reaction rates will be discussed, R1 (O + O + M) and R17 (N + O + M). Preliminary laboratory measurements and evaluations of these rates are currently available, resulting in updated rates for use in the new VTGCM simulations (see Table 4.3).

Research previously published in the literature uses the rate constant of R1 = 2.75 x 10^{-32} cm^6 s^{-1} (*Gérard et al.*, 2008b; *Nair et al.*, 1994; *Campbell and Gray*, 1973) for Venus and Mars where CO_2 is the background atmosphere. However, this rate constant has only been properly evaluated for the case of the Earth, which has a background atmosphere of N_2, based on *Campbell and Gray* (1973). This rate for M = N_2 is then multiplied by a factor of 2.5 (*Nair et al.*, 1994) for an estimation of the relative efficiency of CO_2 (versus N_2) as the third body. The 2.5 factor is very weakly supported and documented. *Nair et al.* (1994) provide no numerical details about how they derived their factor of 2.5 (*Huestis*, private communication). Recently, a preliminary rate coefficient has been measured and suggested for a predominantly CO_2 background atmosphere (*Huestis*, private communication; *Jamieson et al.*, 2009a,b). This preliminary rate, R1 = 1.8 x 10^{-32} cm^3 s^{-1} at 200 K, is slower than what has been used in the past. This implies that 3-body recombination should occur at a lower altitude (higher CO_2 density) in the Venus atmosphere, with a corresponding lowered O_2 airglow layer as well. A sensitivity test has been completed using the preliminary rate in the VTGCM and the model results are discussed in section Chapter 4.

The other rate recently revisited is R17 (see Table 4.3). In previous VTGCM simulations (*Bougher et al.*, 1990) a rate of 1.1 x 10^{-32} $(300/T_n)^{0.5}$ cm^6 s^{-1} was used from *Stewart and Barth* (1979). Upon closer inspection, the *Stewart and Barth* (1979) rate is based upon measurements conducted by *Baulch et al.* (1973), where M = N_2. As stated above, CO_2 is a more efficient third body than N_2. Previous measurements were also conducted with a CO_2 background for two different temperatures (*Campbell* *and Thrush*, 1966). One measurement for 196 K gave a rate of 2.26 x 10^{-32} cm^6 s^{-1} and the other for 298 K gave a rate of 1.83 x 10^{-32} cm^6 s^{-1}. For our new VTGCM, a temperature dependence was derived using these two measurements, giving a rate of 1.83 x 10^{-32} $(298/T_n)^{0.5}$ cm^6 s^{-1}, where T_n is the neutral temperature. The change in this rate does not impact the O_2 IR nightglow but slightly changes the NO UV nightglow. See Chapter 4 for the VTGCM model results and section 4.2.4.2 for comparisons to available observations.

3.6.7 Chemical Trace Species at lower altitudes

A final chemical update to the VTGCM is implemented by adding nightside profiles of specific chemical trace species. *Krasnopolsky* (2010)'s calculations suggest that other odd-O loss processes may be important on the nightside involving trace species that impact nightglow emissions (*Krasnopolsky*, 2010). Trace species have been added to the VTGCM before, but the profiles used were diurnally averaged (*Bougher and Borucki*, 1994; *Yung and Demore*, 1982). At that time, trace species did make a noteable difference in the O density profiles at low thermospheric altitudes (see figure 8 in *Bougher and Borucki*, 1994).

Currently, single density profiles of trace species (Cl, Cl_2, ClCO, ClO, H_2, HCl, HO_2, O_3, OH) from an altitude of 80 km to 130 km for the nightside have been extracted from *Krasnopolsky* (2010) figure 8 and incorporated into the nightside of the VTGCM. *Krasnopolsky* (2010) employs a 1-D photochemical model that is tuned for nightside conditions (photolysis is not involved) which includes 61 reactions and 24 species. As stated in *Krasnopolsky* (2010), the model results are within observational ranges for the O_2 IR, NO UV, and OH IR nightglow emissions and peak altitudes. Therefore, VTGCM reaction rates involving these trace species are taken from table 4 in *Krasnopolsky* (2010) with additional reaction rates from *Yung and Demore* (1982).

It is appropriate not to carry these trace species dynamically in the VTGCM.

This is justified because in the region where the trace species greatly impact the atmospheric chemistry, they have very short chemical lifetimes with respect to the dynamics. When these trace species were added to the VTGCM, they made a noticeable difference in the nightglow layers (see Chapter 4). They provide additional loss terms for the O chemistry at the lower altitudes (below 90 km) and help define a narrower O density layer. This directly impacts the O_2 IR nightglow and indirectly impacts the NO UV nightglow. Without these trace species, the chemistry is incomplete in the VTGCM and the varying nightglow emission layers cannot be properly simulated for comparison to available datasets.

3.7 Double Resolution Examination

Experience with Earth models provides valuable information about the importance of the model resolution with respect to the dynamical features being simulated. The Thermosphere Ionosphere Mesosphere Electrodynamics General Circulation Model (TIME-GCM), similar to the VTGCM, has standard 5° x 5° horizontal and 0.5 vertical scale height grid spacing. It has been found when studying the impacts of tides and planetary waves in Earth's upper atmosphere, that the "standard" resolution was inadequate and resulted in the "artificial" doubling of the wave amplitudes (*Bougher et al.*, 2008). Nevertheless, when the resolution was halved horizontally (2.5° x 2.5°) and vertically (0.25 scale height), the need to double the amplitudes was removed. The impacts of finer resolution upon GCM simulations is a keen area of numerical research.

Subsequently, a finer resolution examination with the VTGCM has been produced to consider the impacts on Venus' upper atmospheric dynamics. The standard VTGCM has 5° x 5° horizontal resolution (∼528 km grid spacing at the equator) and 0.5 vertical scale height. For this examination, the horizontal and vertical resolution was halved. Thus, it has 2.5° x 2.5° horizontal resolution (∼264 km grid spacing at the equator) with 138 pressure levels from Z_p = -16 to Z_p = 18, instead of 69 pressure levels. Along with the resolution change, the time-step must be smaller to satisfy the Courant-Friedrichs-Lewy criterion; therefore it now uses 15 seconds instead of 30 seconds. This examination is valuable to better understand the dynamical dependencies on resolution within the VTGCM; it would also be beneficial to incorporate finer resolution for wave studies in the Venus upper atmosphere. The results are shown and discussed in Chapter 4.

3.8 Gravity Wave Momentum Drag Scheme

Gravity wave momentum is thought to be crucial in modeling Venus' upper atmosphere. The most common mechanism to implement gravity wave momentum deposition is Rayleigh friction, which has been discussed in a previous section. The shortcoming of Rayleigh friction is that is it not consistent with the prognostic equations; i.e. it is parameterized and therefore not based on first principles. However, it does provide a starting point in understanding the necessary magnitude of the drag.

Zhang et al. (1996) replaced Rayleigh friction with a gravity wave scheme within an older version of the VTGCM. They incorporated the *Fritts and Lu* (1993) gravity wave parameterization (hereafter F-L scheme) which uses the integrated effect of a full wave spectrum. The F-L scheme is based on gravity wave saturation theory and empirical observations of the characteristics of gravity waves in the Earth's atmosphere. Most of the Earth parameters are assumed to be valid for Venus, since there are very few gravity wave observations in Venus' atmosphere. For brevity the equations will not be discussed (see *Zhang et al.*, 1996, for an explanation and description of the equations). However, the equations contain key adjustable parameters. The first set of parameters are the characteristic intrinsic phase speeds for the east (c_e), west (c_w), north (c_n), and south (c_s) components of the gravity waves at the lower boundary (94 km for the older VTGCM). The second set of parameters describe the shape of the total gravity wave energy density profile: H_E is a growth factor dependent on pressure scale height, z1 and z2 are the bottom and top boundary of the transition region. *Zhang et al.* (1996) made extensive sensitivity tests with these parameters. They used their wind, temperature, and the O_2 IR nightglow results for solar medium condition to help constrain their gravity wave parameters and they show a couple of cases in their paper. The best set of parameters for symmetric zonal winds across the terminator were an average phase speed of $c_e = c_w = c_n = c_s = 60$ m s^{-1} at 94 km, $H_E = 1.5H$ (H = pressure scale height), z1=100 km, and z2 = 115 km. This suite of parameters provided maximum zonal winds at 18:00 LT of 237 m s^{-1} at 160 km and a minimum at 06:00 LT of -237 m s^{-1} at 160 km. The O_2 IR nightglow intensity was 1.04 MR at midnight and a maximum temperature of 306 K at 195 km on the dayside. These quantities were produced with a maximum (minimum) gravity wave drag of 0.02 m s^{-2} (-0.02 m s^{-2}) at 140 km and 06:00 LT (18:00 LT). Their best set of parameters for asymmetric zonal winds across the terminator were $c_w = 65$ m s^{-1}, $c_e = c_n = c_s = 60$ m s^{-1} at 94 km, $H_E = 1.5H$, z1=100 km, and z2 = 115 km. This case simulated maximum zonal winds at 18:00 LT of 265 m s^{-1} at 165 km and a minimum at 06:00 LT of -140 m s^{-1} at 170 km. The O_2 IR nightglow intensity was 0.64 MR at 06:00 LT. These quantities were produced with a maximum (minimum) gravity wave drag of 0.022 m s^{-2} (-0.02 m s^{-2}) at 135 km (140 km) and 06:00 LT (18:00 LT).

This gravity wave study with the older VTGCM proved the gravity wave momentum drag can reduce zonal wind speeds and reproduce the observed asymmetries in temperature and composition. The O_2 IR nightglow intensity and location was very sensitive to small changes of the characteristic intrinsic phase speeds. The nightglow intensity would decrease and shift towards the morning terminator with the stronger asymmetric characteristic intrinsic phase speeds, which was in agreement with observations. *Zhang et al.* (1996) found that implementing the F-L scheme was an improvement over the Rayleigh friction parameterization. It provided self-consistency and was based on the physical process of gravity wave saturation.

As a preliminary study, the F-L scheme is being applied to the new VTGCM. This provides a difficult task in tuning the parameters with the new VTGCM, due to its improvements. One of the improvements is the extension of the vertical scale; the bottom boundary is 70 km instead of 94 km. This impacts the selection of characteristic intrinsic phase speeds and possibly the altitudes of the transition region. The other improvement is the temperature on the dayside and nightside near 120 km and 105 km; these regions are much warmer (∼40 - 60 K warmer) than the previous simulations (*Zhang et al.*, 1996). The warmer temperatures could change how the H_E parameter, the energy density growth factor; responds to the warmer areas since it is based on the pressure scale height. The results of this preliminary study will be discussed further in Chapter 4.

3.9 Summary

Numerical modeling is a very important tool in understanding complex chemical-dynamical systems in planetary upper atmospheres. This is shown throughout the dissertation with the application of the VTGCM. All types of models have their strengths and weaknesses. One-Dimensional modeling is crucial to grasp first principle understanding of the vertical structure at specific locations. It also provides important information, such as eddy diffusion, for other models. Conversely, it fails to provide information on large-scale dynamical feedbacks. The symmetric 2-D models are proven valuable to understand the connection between the temperatures, composition and winds in Venus' upper atmosphere. The more recent models compared quite well with the empirical models. The shortcoming of the 2-D model is the inability to simulate the asymmetric characteristics observed by PVO. The spectral transform 3-D model produced asymmetries in densities and temperatures; reasonable diurnal variation for the major and minor species. It provided dynamical constraints for future modeling; however inconsistency is still a problem due to the model being highly parameterized. The VTGCM fills many of the downfalls of these previous models. It solves the prognostic equations consistently within the GCM and produces comparable results to observations. These results are illustrated and described in the next chapter. However, gravity wave momentum drag schemes must be incorporated and thoroughly tested within the VTGCM to remove its reliance upon Rayleigh friction.

CHAPTER IV

Results and Implications

4.1 Introduction

With a completed background description of the VTGCM and current observations, it is only appropriate to launch into model results and the comparison with observations. The first half of this chapter has two detailed sections about (1) the VTGCM "mean" simulation and the sensitivity tests performed and (2) a comparison of measured and calculated VEX O density distributions on the nightside. These sections are followed by (3) a short explanation how the VTGCM performed in high resolution (2.5° x 2.5°) simulations. The last sub-section contains the results from preliminary work with the incorporation of the F-L gravity wave drag scheme.

4.2 VTGCM "Mean" Simulation

This section outlines the inputs specified for a VTGCM best case (also referred to as a "mean" simulation) and illustrates specific results for the Venus upper atmosphere structure and dynamics (e.g. temperatures, winds, O and N(^{4}S) densities, O_2 IR and NO UV nightglow emissions). A "mean" simulation is computed from a "warm" start-up and with static input parameters (section 4.2.1) and boundary conditions (section 3.6.2). The model is run to a steady-state solution. Steady-state is determined by the difference between the last simulated model day and the previous simulated model day having a percent difference of less than 2% for all prognostic fields. For the VTGCM, a typical simulation takes around 9 simulated Earth days to reach a steady-state solution. Once a realistic "mean" simulation is completed, sensitivity tests are performed with two adjustable parameters (maximum nightside eddy diffusion and wave drag impacting the global wind system). In addition, an evaluation is made of the chemical impacts by varying key reaction rates and adding chemical trace species. The purpose of this section is to examine the VTGCM "mean" simulation results using VEX parameters and to demonstrate the VTGCM sensitivity to specific input parameters. Data-model comparison will be conducted in section 4.2.4, specifically focused on VEX measurements.

4.2.1 "Mean" Simulation - Parameters for VEX conditions

In order to simulate mean conditions for the Venus' middle and upper atmospheres during VEX sampling period, the VTGCM is run with solar minimum fluxes (F10.7 = 70), a nightside max eddy diffusion of 1.0 x 10^7 cm^2 sec^{-1} and a wave drag parameter of 0.5 x 10^{-4} sec^{-1}. Mean VEX conditions are best captured by VEX statistically averaged mean nightglow emission maps. Presently, the O_2 IR statistical map exists and is used for data-model comparisons for mean conditions (*Gérard et al.*, 2008c; *Piccioni et al.*, 2009; *Soret et al.*, 2010a). Other maps have been created for single orbits and are being used to observe the airglow morphology (*Hueso et al.*, 2008). The NO UV statistical map is in progress and has provided initial information on the averaged nightglow morphology (*Cox*, 2010).

4.2.2 "Mean" Simulation - Results

The measured thermal structure of Venus' upper atmosphere has several interesting characteristics that the VTGCM reproduces in its "mean" simulation. Figure 4.1

represents the simulated thermal structure near the equator at 2.5°N. At the exobase (~190 km), temperatures range from 238 K on the dayside to 111 K on the nightside. At 1200 LT near 112 km is a warm region, about 207 K, created by near IR (i.e. mostly 4.3 μm) heating. Near 0000 LT, a warm layer is produced at 103 km with a simulated temperature around 188 K. Figure 4.2 illustrates the heating and cooling at 12:00 LT and 00:00 LT. Furthermore, Figure 4.3a shows a 1D representation of the nightside temperature profile.

The nightside warm region is associated with the dayside warm area (in the lower thermosphere) and the resulting day-to-night global circulation, which produces dynamical heating near midnight. The total dynamical heating rate (adiabatic + total (horizontal + vertical) advection) at 103 km near the anti-solar point is 64 K/day (see Figure 4.3b). This heating rate is dominated by adiabatic heating at 103 km near midnight. Above 130 km on the nightside, temperatures remain cold at 114 K. Thus the new VTGCM simultaneously reproduces the nightside cryosphere (>130 km) characterized by PVO observations and reproduced by previous modeling efforts (*Keating et al.*, 1979a; *Bougher et al.*, 1997), and the observed warm nightside temperature near 100 km at midnight (see 4.2.4.1).

The neutral zonal winds near the equator are illustrated in Figure 4.4. The evening terminator (ET) winds are 202 m s^{-1} at ~120 km and reach a maximum at 314 m s^{-1} near 180 km. The morning terminator (MT) winds are -130 m s^{-1} near 120 km and are maximum at -191 m s^{-1} near 172 km. The ET winds are faster than the MT winds since the drag term is prescribed asymmetrically in local time in order to mimic the observed upper atmosphere RSZ winds (see Figure 4.5). It is noteworthy that the VTGCM captures the shift in the convergence of the flow away from midnight and toward the morning terminator above 110 km. This wind system provides a downward vertical velocity at midnight of ~0.1 m s^{-1} at 105 km, which is consistent with other estimates in the literature (*Bailey et al.*, 2008; *Ohtsuki et al.*, 2008) but

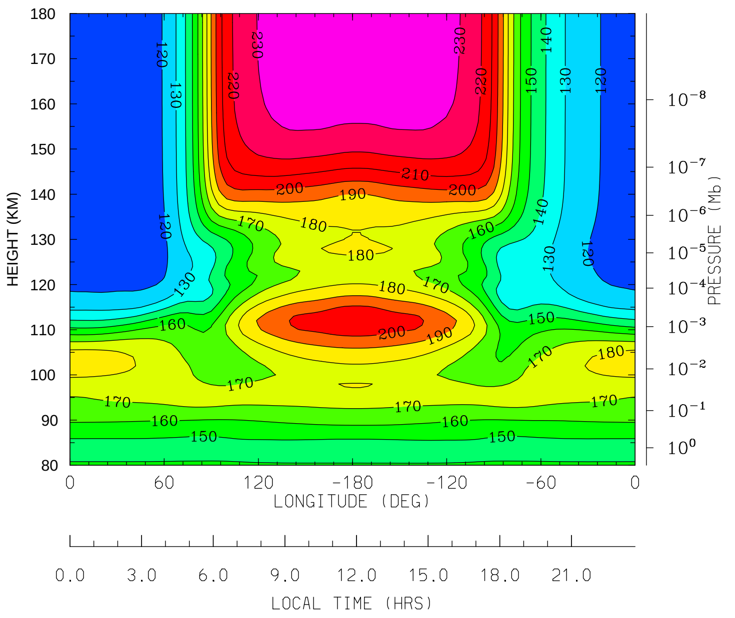

Figure 4.1: VTGCM "mean" case for VEX conditions; longitude-height cross section at 2.5°N (local time vs height) for temperature (K).

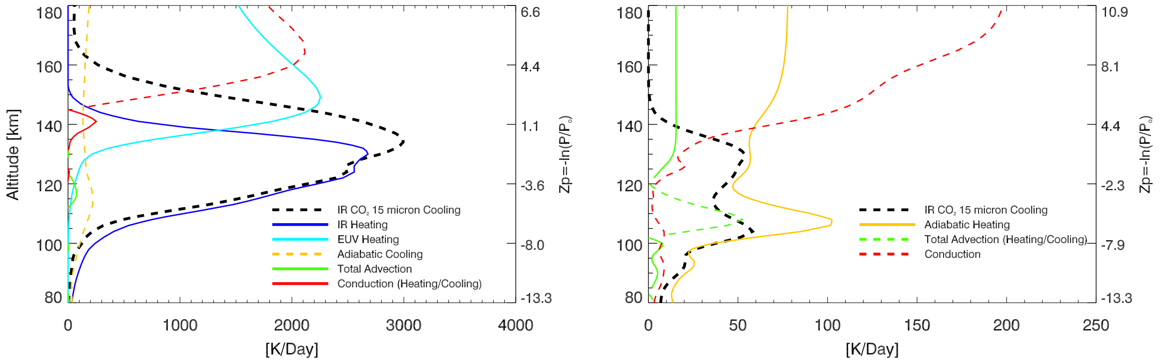

Figure 4.2: The heating and cooling terms at LT = 12:00 (left panel) and LT = 24:00 (right panel) near the equator. The hashed lines represent cooling and the solid lines represent heating

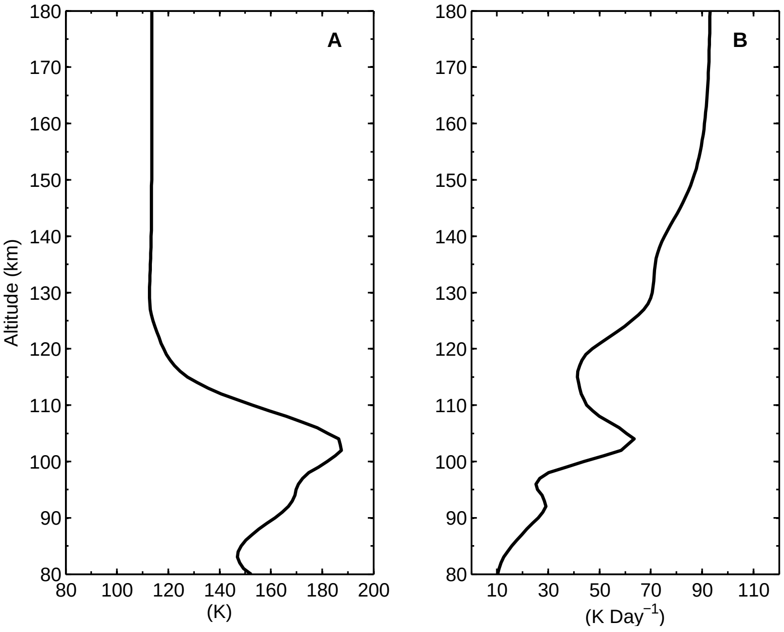

Figure 4.3: VTGCM "mean" case profiles at 2.5°N: (a) temperature (K) at 0000 LT and (b) total dynamical heating rate (K/day) (adiabatic + total advection) at 0000 LT.

lower than the *Bertaux et al.* (2007) value of 0.43 m s^{-1}.

Figure 4.5 shows the ET and MT total zonal wind profiles and the prescribed RSZ wind profile (also discussed as the u$_{SR}$ term in the wave drag equation). The difference between the terminator symmetric and asymmetric total zonal wind profiles reflects the impact of the prescribed RSZ wind profile (see Figure 4.5c). Notice that the RSZ profile is applied globally with respect to height and plays a crucial part in producing the nightglow distributions (i.e. the local time location of the peak emission). In order for the O_2 IR nightglow peak intensity to be produced at midnight, the RSZ needs to be very weak (as shown in Figure 4.5c), up to ∼110 km. By contrast, for the NO UV nightglow peak intensity to be positioned near 02:00 LT, the RSZ wind has to be 30 - 60 m s^{-1}, above ∼110 km. On the dayside, N(^{4}S) atoms are produced near ∼140 km, and subsequently are transported nightward as they follow descending pressure levels to the colder nightside. The dayside pressure at 140 km is equivalent to the pressure at ∼130 km on the nightside. For this altitude region, the RSZ wind is 60 m s^{-1} which is comparable to estimates from previous measurements (see Table 1 in *Bougher et al.* (2006)). Conversely, O is produced near 110 km on the dayside and descends more gradually to the nightside along constant pressure surfaces owing to a weak diurnal variation in temperatures. For more details about the impacts RSZ winds have on the nightglow, see sections 4.2.4.2 and 4.2.4.3.

Figure 4.6 illustrates the atomic oxygen density profiles for noon and midnight near the equator. Profiles are provided from 80 km - 180 km to focus on the density structure near the peak. The atomic oxygen density at noon peaks at 94 km with a value of 5.5 x 10^{10} cm^{-3}, while the midnight value is 3.4 x 10^{11} cm^{-3} at 104 km. This ~6 fold enhancement from day to nightside is the result of efficient transport of atomic oxygen atoms from their day side source to their nightside chemical loss at and below 104 km. The VTGCM also produces a noon time O/CO_2 mixing ratio for the dayside at 140 km of 5%. The corresponding net dayside column integrated production (at 60° SZA) for O atoms is calculated to be 2.34 x 10^{12} cm^{-2} s^{-1}.

The $N(^4S)$ density profile for noon and midnight near the equator is shown in Figure 4.7. The plot ranges from 80 km to 180 km to focus on the structure near the density peak. At noon, the peak value near the equator is 1.0 x 10^8 cm^{-3} at 136 km. The nightside density profile peaks at 1.4 x 10^8 cm^{-3} at 115 km near the equator. This 40% fold enhancement, although less pronounced than atomic oxygen, still reflects the combined effects of transport and nightside chemical destruction of atomic nitrogen at and below ~110 km. This is complemented with a net dayside column integrated production at 60° SZA for $N(^4S)$ of 1.58 x 10^{10} cm^{-2} s^{-1}.

The results presented in Figure 4.8 illustrate the maximum volume emission rate for the O_2 IR nightglow near the equator at ~100 km to be 1.7 x 10^6 (photon cm^{-3} s^{-1}) with a corresponding peak vertical intensity of 1.76 MR. This peak value is near midnight in concert with the simulated global wind structure. The nightside hemispheric average (defined by a box of 60°S to 60°N and 60°E to 60°W) is ~0.51

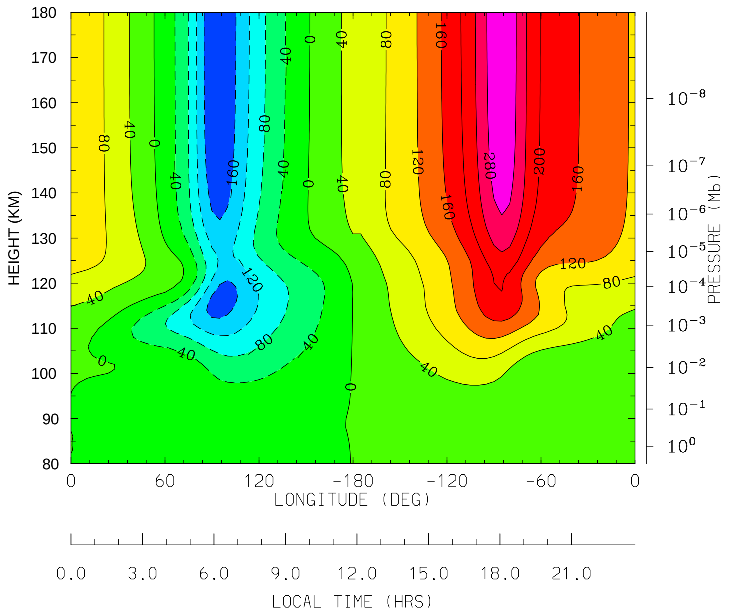

Figure 4.4: VTGCM "mean" case for VEX conditions; longitude-height cross section at 2.5°N (local time vs height) for zonal winds (m s^{-1})

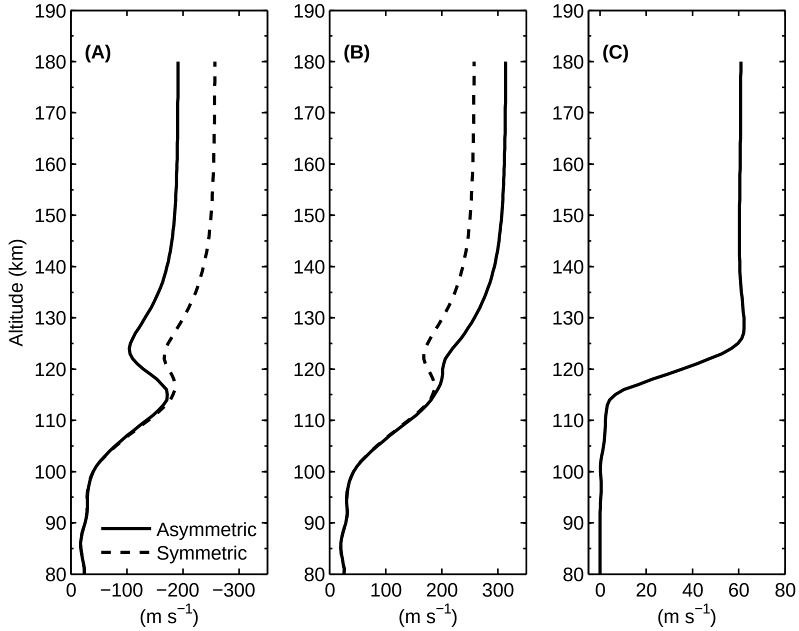

Figure 4.5: VTGCM "mean" case for VEX conditions; longitude-height cross section at 2.5°N: (a) the morning terminator (MT) total zonal winds (m s^{-1}) where the solid line represents the asymmetric case and the dashed line represents the symmetric case, (b) the evening terminator (ET) total zonal winds (m s^{-1}) where the solid line represents the asymmetric case and the dashed line represents the symmetric case, and (c) the retrograde zonal winds (RSZ) prescribed as a function with height (m s^{-1}).

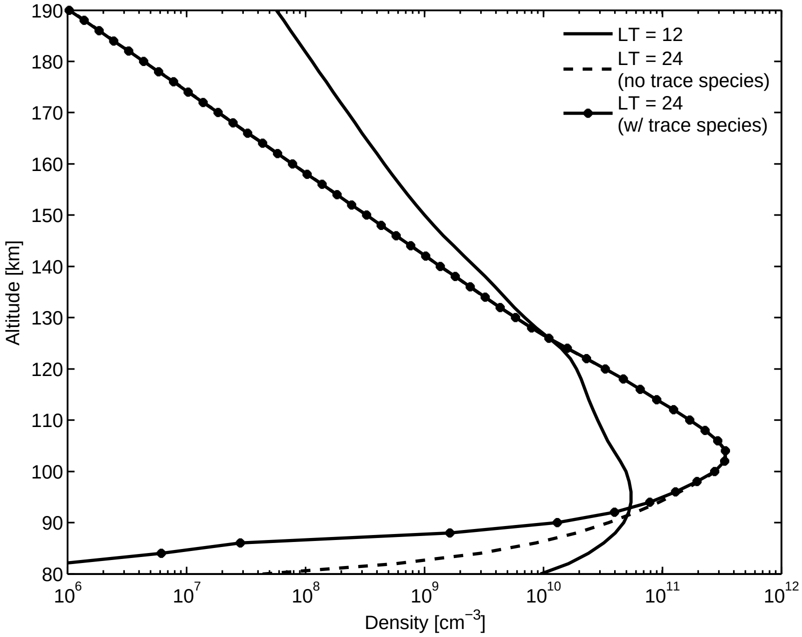

Figure 4.6: VTGCM "mean" case for VEX conditions; density profiles at 2.5°N (density vs height) for atomic oxygen at noon and midnight. The density is in units of cm^{-3}.

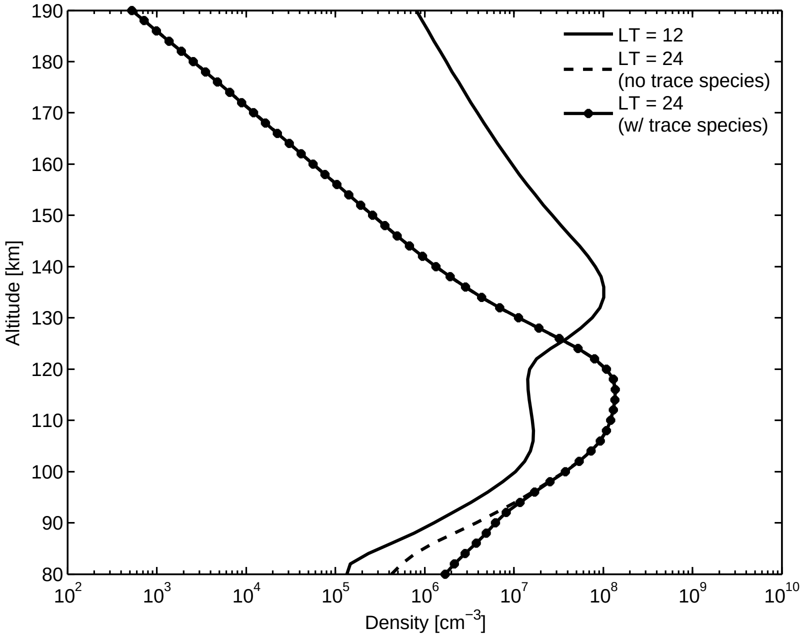

Figure 4.7: VTGCM "mean" case for VEX conditions; density profiles at 2.5°N (density vs height) for N(^{4}S) at noon and midnight. The density is in units of cm^{-3}.

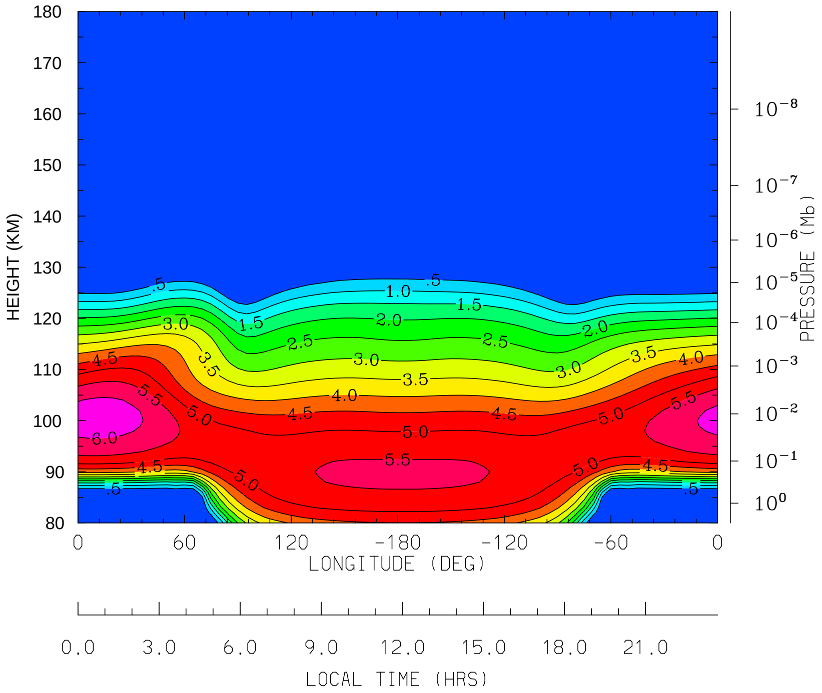

Figure 4.8: VTGCM "mean" case for VEX conditions; longitude-height cross section at 2.5°N (local time vs height) illustrates a max O_2 IR night airglow volume emission rate close to midnight. The emission rate unit is $\log_{10}(\text{photons cm}^{-3}\ \text{s}^{-1})$.

MR requiring ∼0.22 photons per O atom produced on the dayside and made available to the nightside for destruction. A 100% yield of the three body reaction (O + O + CO_2) for production of O_2 IR nightglow would provide a peak vertical intensity closer to 2.37 MR and a hemispheric average of 0.63 MR.

Figure 4.9 illustrates the volume emission rate of the NO UV nightglow for the δ and γ bands near the equator. The maximum value is 1.2 x 10^3 (photon cm^{-3} s^{-1}) near 106 km and has a corresponding peak vertical intensity of 1.83 kR. The peak value is shifted towards the morning terminator and is located at ∼01:00 LT due to the asymmetrical global winds at 107 km (see Figure 4.5). The nightside hemispheric intensity average is 0.68 kR. This emission requires 0.04 photons per N atom produced on the dayside and made available to the nightside for destruction. For this "mean" simulation (and incorporating a suite of standard reactions and modern rates) the O_2

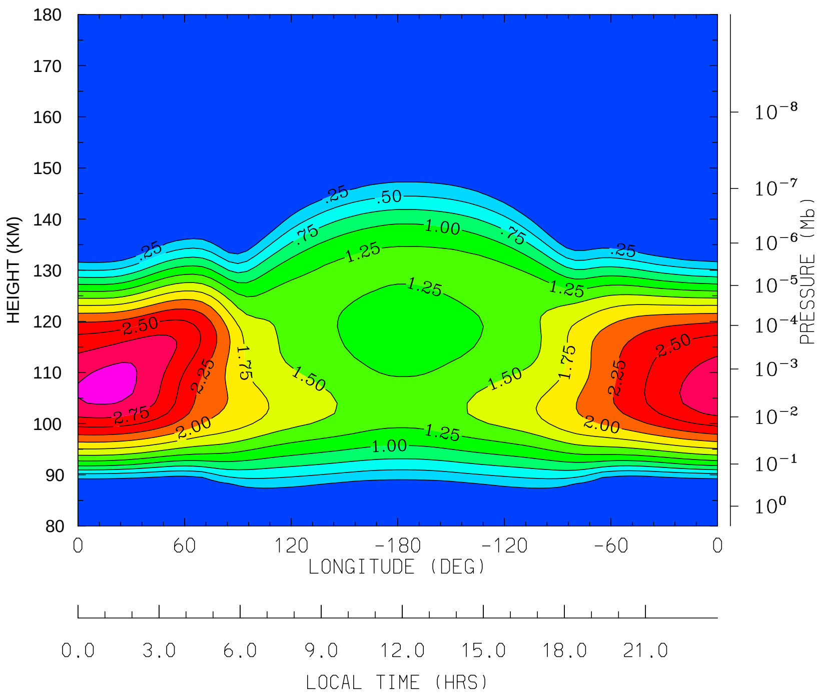

Figure 4.9: VTGCM "mean" case for VEX conditions; longitude-height cross section at 2.5°N (local time vs height) illustrates a max NO UV night airglow volume emission rate close to 01:00 LT. The emission rate unit is $\log_{10}$(photons cm^{-3} s^{-1}).

IR and NO UV night airglow layers are very close in altitude and therefore exist in a similar dynamical region of the upper mesosphere and lower thermosphere.

Time scale plots provide a good measure of the processes which dominate in any given region at a given time. Figure 4.10 shows vertical profiles of the atomic oxygen and N(^{4}S) chemical lifetimes, eddy diffusion lifetime, and dynamical lifetimes at 0000 LT in units of days. The chemical lifetime is calculated as the inverse of loss frequency with atomic oxygen (or N(^{4}S)) being the chemical species of concern, since it is the major contributor for the reaction of the O_2 IR (or NO UV) night airglow. Eddy diffusion lifetime is estimated by $\tau_{eddy} = \frac{H^2}{K_{eddy}}$, where H is the scale height, and K_{eddy} is the eddy diffusion coefficient. The lifetime corresponding to the horizontal wind (motion of a parcel) utilizes the wind velocity on the evening terminator; i.e. it is the location of the fastest horizontal winds and therefore a dominant contributor

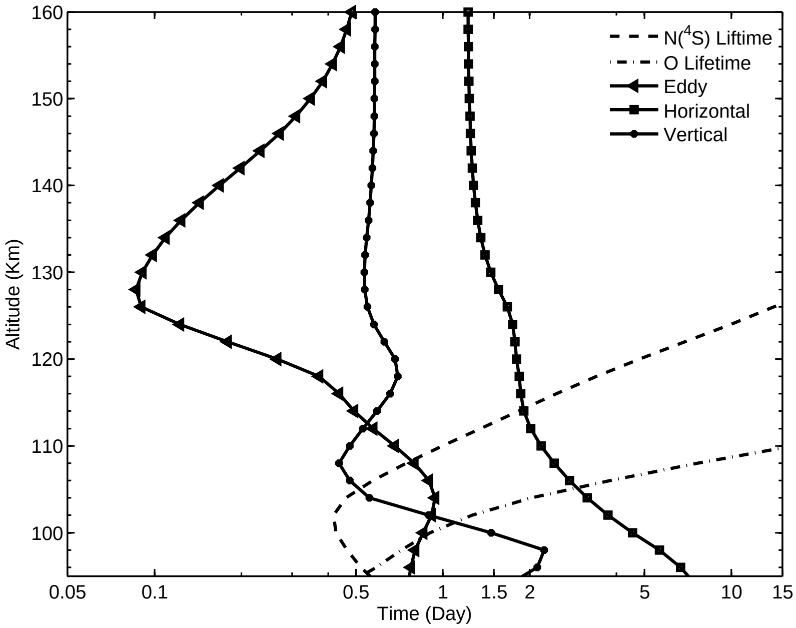

Figure 4.10: VTGCM "mean" case for VEX conditions; time scale profiles at 2.5°N (time (day) vs height (km)) for midnight.

to the distribution of chemical species. The vertical wind lifetime is $\tau_{vertical} = \frac{1}{w}$, where $\tau_{vertical}$ is the vertical velocity lifetime and w is vertical motion. Both nightglow emissions are controlled mainly by the strength of the global circulation which transports O and N(^{4}S) atoms from the dayside. In the case of the O_2 IR night airglow, the time scale plot reveals the eddy diffusion lifetime matches the O chemical lifetime at 100 km, while dynamics plays a role at higher altitudes. Therefore eddy diffusion is the dominating process in the region where the volume emission rate of the O_2 IR night airglow peaks. For N(^{4}S), the altitude of the airglow is different from O_2 IR night airglow and it is controlled by the vertical winds. The vertical wind lifetime and the N(^{4}S) lifetime cross at 105 km. Therefore the time scale plot shows the vertical velocity dominating the region where the NO UV airglow peaks, while the eddy diffusion time scale is not competitive enough to make a significant impact on the airglow altitude peak. If the winds are slowed down sufficiently to let eddy diffusion dominate, day to night transport of O and N atoms is inadequate to provide the source for the intense emissions of O_2 IR or NO UV airglow observed.

4.2.3 Sensitivity Tests upon the “Mean” Simulation

As mentioned in the introduction (Chapter 1), our purpose for VTGCM analysis of VEX datasets is to understand the processes controlling the variable night airglow layers. The O_2 IR and NO UV night airglow layers were subsequently examined for their sensitivity to two adjustable parameters in the VTGCM model (i.e. the maximum nightside eddy diffusion and the strength of the Rayleigh friction (the global wind system)). A discussion follows about the chemical impacts on the nightglow emissions and their distributions.

4.2.3.1 Sensitivity Tests - Eddy Diffusion

For the eddy diffusion test, the maximum eddy diffusion coefficient is varied. The eddy diffusion coefficient is prescribed in the form $K = \frac{A}{\sqrt{n}}$ with units of cm^2 s^{-1} where n is the total number density, A is a constant, and K is the eddy diffusion coefficient (which can be capped at a maximum value, $Kmax$) (*von Zahn et al.*, 1979). Three $Kmax$ values are used for the test; (a) the maximum case is 8.0 x 10^7 cm^2 s^{-1}, (b) the minimum case is 1.0 x 10^6 cm^2 s^{-1}, and (c) the best case (which corresponds to the results previously discussed in section 4.2.2) is 1.0 x 10^7 cm^2 s^{-1}. The results of the sensitivity test can be seen in Table 4.1. Eddy diffusion proves to be a major factor in controlling the altitude of the nightglow peaks (*Bougher et al.*, 1997; *Bougher and Borucki*, 1994). For the new VTGCM, the O_2 IR nightglow intensity is more sensitive than the NO UV nightglow to the changing eddy diffusion coefficient. The airglow intensities also vary with respect to the location of the sources and sinks of the airglow layer. Lower in the atmosphere, CO_2 concentrations are greater, which reduces the O_2 IR night airglow chemical sources by increasing the deactivation of the O_2 ($a^1\Delta$) state by CO_2. The NO UV nightglow intensity varies as the airglow

Table 4.1: Results from the Nightside Eddy Diffusion sensitivity test

O_2 (IR)	O Den Peak (Night) (# cm^{-3})	Alt. (km)	Peak Intensity (MR)	Airglow Peak Alt. (km)
Best	3.41 x 10^{11}	104	1.76	100
Max	2.62 x 10^{11}	102	1.04	100
Min	3.93 x 10^{11}	105	2.58	103
NO (UV)	N Den Peak (Night) [#/cm^3]	Alt. [km]	Peak Intensity [kR]	Airglow Peak Alt. [km]
Best	1.37 x 10^8	115	1.83	106
Max	1.76 x 10^8	109	1.64	104
Min	1.65 x 10^8	118	2.04	109

layer moves vertically for a similar reason, with its sink being:

$$N(^4S) + O + CO_2 \rightarrow NO + CO_2 \tag{R17}$$

A larger eddy coefficient leads to reaction (R17) competing more effectively with reaction (R16) for $N(^4S)$ atoms, thereby reducing the NO^* source. The opposite happens when the eddy coefficient is minimized.

4.2.3.2 Sensitivity Tests - Wind

The wind sensitivity is related to the tunable wave drag parameter which is part of the Rayleigh friction scheme. The Rayleigh friction term is implemented to approximate gravity wave momentum drag affects. This rudimentary formulation is linearly proportional to the horizontal (2D) wind, and is added to the momentum equation thereby controlling the magnitude of the zonal and meridional winds and ultimately the magnitude of the subsiding winds near midnight. The procedure of the wind sensitivity test is similar to the eddy diffusion sensitivity test. The wave drag time scale maximum values (λ_{RF} parameter in the wave drag equation) used are as follows; (a) the maximum case is 2 x 10^{-4} s^{-1} (providing slower winds), (b) the minimum case is 1.25 x 10^{-5} s^{-1} (providing faster winds), and (c) the best case is 0.5 x 10^{-4} s^{-1} (providing optimal winds and is used for all results previously discussed in section 4.2.2).

Table 4.2 summarizes the results of the wind sensitivity study. These cases demonstrate that the intensities of the nightglow emissions are impacted more strongly than the altitude of the airglow peaks. The stronger impact on the intensities is due to the SS-AS wind system that supplies the nightside with O and N(^{4}S) atoms transported from the dayside. The airglow intensities respond accordingly to the strength of the winds while the nightside N(^{4}S) peak density does not. In addition, the O density and the N(^{4}S) density have opposite responses to the strength of the wind. The closer the density peaks are in altitude the greater the loss of N(^{4}S) through reactions R10 and R12. As seen in Table 4.2, the weaker winds provide more N(^{4}S) (less O) on the nightside and the stronger winds yield more N(^{4}S) and O when compared to the Best Case. This implies the drag term is most influential between 100 km and 110 km, where O density peaks. For the morphology of the nightglow emissions, the local time distribution is shifted toward the MT (ET) when there are stronger (weaker) winds. Therefore, the source of these atoms, and thus the airglow peak brightness and location, directly depends on the strength of these winds.

4.2.3.3 Sensitivity Tests - Key Chemical Reaction Rates

For the 3-body reaction rate R1, modelers have been using a standard Earth value and multiplying it by a constant factor to enable the reaction rate to correspond to a CO_2 dominated atmosphere. Recently, this reaction has been measured in the laboratory in a CO_2 background atmosphere by *Jamieson et al.* (2009b). In Table 4.3 the different reaction rates used in this sensitivity test are clearly stated. When the preliminary R1 rate is used a slight impact on the O density profiles is identified within the VTGCM's simulations. The change to the preliminary rate leaves more O available on the nightside and decreases the peak O_2 airglow intensity to 1.68 MR. However, the peak altitude remained at 100 km. The NO UV airglow layer remains

Table 4.2: Results from the wind sensitivity test

O_2 (IR)	O Den Peak (Day) (# cm^{-3})	Alt. (km)	O Den Peak (Night) (# cm^{-3})	Alt. (km)	Peak Intensity (MR)	Airglow Peak Alt. (km)
Best	5.47 x 10^{10}	94	3.41 x 10^{11}	104	1.76	100
Max	5.56 x 10^{10}	95	2.36 x 10^{11}	104	0.92	99
Min	5.44 x 10^{10}	94	3.93 x 10^{11}	104	2.42	101

NO (UV)	N Den Peak (Day) (# cm^{-3})	Alt. (km)	N Den Peak (Night) (# cm^{-3})	Alt. (km)	Peak Intensity (kR)	Airglow Peak Alt. (km)
Best	1.03 x 10^{8}	136	1.37 x 10^{8}	115	1.83	106
Max	2.17 x 10^{8}	134	2.30 x 10^{8}	115	1.64	110
Min	7.00 x 10^{7}	136	1.65 x 10^{8}	115	3.56	106

T_{night}	Peak Temp [K]	Alt. [km]
Best	188	103
Max	173	94
Min	207	105

at 106 km, but has a slight increase in intensity to 1.9 kR.

In the past, the VTGCM used an Earth based value for the 3-body reaction rate R17. This sensitivity study compares the atmospheric impacts when using this previous reaction rate (test) and a standard one based upon measurements using a CO_2 background atmosphere (see Table 4.3 and see section 3.6.6 for more details about the rates). By using the standard reaction rate (1.83 x 10^{-32} $(298/T_n)^{0.5}$ cm^6 s^{-1}), which is faster, this requires fewer N and O atoms for reaction R16 to occur at higher altitudes, thus resulting in the NO UV airglow layer occurring higher in the atmosphere and further separated from the O_2 IR airglow layer. When using the test reaction rate (1.1 x 10^{-32} $(300/T_n)^{0.5}$ cm^6 s^{-1}), which is slower, this leads to N and O atoms recombining lower in the atmosphere. Indeed, application of the standard rate raises the NO UV nightglow layer a couple of kilometers and the intensity decreases slightly. R17 is the least important loss of N(^{4}S) compared to reactions R16 and R15. Nevertheless, since R17 does impact the NO UV nightglow, this chemical reaction rate is in need of a modern laboratory measurement for application to Venus.

Table 4.3: Key Chemical Reaction Rate Tests (cm^6 s^{-1})

	R1 (O + O + M)	R17 (N + O + M)
Standard	2.75×10^{-32} (*Gérard et al.* (2008b))	1.83×10^{-32} $(298/T_n)^{0.5}$ (*Campbell and Thrush* (1966))
Test	1.8×10^{-32} (*Jamieson et al.* (2009b))	1.1×10^{-32} $(300/T_n)^{0.5}$ (*Stewart and Barth* (1979)

In the literature, error bars are typically stated for measurements of chemical reaction rates. Thus, a careful examination of a range of reaction rates for odd-N chemistry was tested using the VTGCM. Little impact was observed on the altitude of the NO UV nightglow peak (*Bougher et al.*, 1990; *Fox*, 1994; *Fox and Sung*, 2001; *Krasnopolsky*, 2010). In short, the best combination of rates are listed in Table 3.2.

4.2.3.4 Sensitivity Tests - Chemical Trace Species

By implementing the *Krasnopolsky* (2010) night profiles of chemical trace species into the VTGCM, the density profiles and night airglow distributions were impacted. The trace species provide additional loss terms for the O chemistry below 95 km, which creates a narrower O density layer (see Figure 4.6). The more defined O density layer becomes more sensitive to the dominating reactions (e.g. R1), as previously discussed, resulting in a more sensitive airglow emission layer with respect to the eddy diffusion coefficient. The O_2 IR nightglow layer is raised a kilometer with the trace species, and the peak intensity is increased (by 0.2 MR). The $N(^4S)$ density plot changes slightly as well (see Figure 4.7). The NO UV airglow is created in the region where the $N(^4S)$ density layer overlaps the O density layer. Since the O density layer is more sensitive to the eddy diffusion coefficient, this also creates a more variable NO UV airglow layer. However, the NO UV nightglow layer and intensity did not change in altitude with the addition of trace species.

4.2.3.5 Sensitivity Tests - Conclusions

These sensitivity tests show that the wave drag parameter (impacting wind magnitudes) controls the intensity of the nightglow emissions, while eddy diffusion controls the altitude of the nightglow layers. The O_2 IR nightglow is more sensitive to eddy diffusion and the NO UV nightglow is more sensitive to the wave drag parameter (the strength of the global wind system). The key reaction rate tests revealed little impact on the nightglow layers location, but slightly impacted the intensity. The addition of chemical trace species is crucial for completeness and determining the shape of the O_2 airglow layer. Overall, these different responses may explain (in part) the observed variability in location and intensity of the O_2 IR and NO UV nightglow emissions. Moreover, the implications of the time scale plot (see Figure 4.10) plus, the eddy diffusion, and the wind sensitivity tests point to a dynamical explanation for the lack of correlation between these recently observed nightglow emissions (see section 4.2.4.3)(*Gérard et al.*, 2009a).

4.2.4 Implications and Data Model Comparisons

The latest VTGCM modeling efforts have been focused on three key VEX observations; (a) the nightside warm layer near 100 km, (b) the O_2 IR nightglow, and (c) the NO UV nightglow. Currently, the modeling of these key observations is unique because the VTGCM alone provides a self-consistent set of structural and dynamical fields (i.e. temperature, three component winds, major composition). These results provide confidence in the "realism" of the global thermospheric circulation pattern for mean conditions.

4.2.4.1 Nightside Temperature

The first key observation is the nightside warm layer, which was first measured using stellar occultations from SPICAV (*Bertaux et al.*, 2007). These limited VEX measurements show temperatures of ∼185 K up to ∼240 K for an altitude range of 95-100 km. These authors state that continued measurements are needed to establish a climatology of these temperatures and confirm a mean value in this nightside altitude region. VEX observations are being supplemented with ground-based observations which generally reveal ∼95 to 100 km nightside temperatures near midnight that are cooler (∼160 - 200 K) than the SPICAV values (*Rengel et al.*, 2008; *Clancy et al.*, 2008; *Bailey et al.*, 2008). See Table 2.5 for a summary of recent observations of this nightside warm layer.

The VTGCM "mean" simulation (e.g. Figure 4.3) shows a peak nightside temperature of 188 K at 103 km for comparison with previously discussed observations. This nightside peak temperature, absent in the earlier version of the VTGCM, is directly connected with a more realistic 4.3 micron heating on the dayside, and the resultant enhancement of day-to-night winds. The stronger winds create a larger thermal advection and result in increased adiabatic heating near midnight. The opposite effect on the temperature occurs when the winds are weakened (see section 4.2.3.2). The VTGCM nightside temperature of ∼190 K near 100 km corresponds to an average case for solar minimum conditions, in accord with available spacecraft and ground-based observations (see Table 2.5. Continued monitoring will provide additional observations that will help confirm average nightside temperatures.

4.2.4.2 O_2 IR Nightside Airglow

The second key observation is the O_2 IR nightside airglow. *Gérard et al.* (2008c) created a statistical hemispheric mean map of the nadir viewed O_2 IR airglow intensity which provided a maximum emission of ∼3 MR, but was later corrected to be ∼1.6 MR (*Soret et al.*, 2010a). The peak emission is located near the equator at midnight, but significant variability is shown in the distribution and intensity. In addition, *Piccioni et al.* (2009) created a similar O_2 IR nightglow map using an expanded data set that overlaps the one used by *Gérard et al.* (2008c) for their map. The maximum vertical emission rate is 1.2 MR and is located at the antisolar point slightly below the equator. Both the *Soret et al.* (2010a) and *Piccioni et al.* (2009) O_2 IR nightglow maps illustrate a hemispheric average intensity of ~0.5 MR. *Gérard et al.* (2009b) and *Soret et al.* (2010a) have been able to deduce nightside O density profiles (consistent with O_2 IR nightglow maps) which provide additional valuable constraints for modelers.

The *Gérard et al.* (2008c) one-dimensional chemical diffusive model can replicate the O_2 IR airglow peak altitude. This nightside one-dimensional model has two main tunable parameters: the downward flux of atomic oxygen and the eddy diffusion coefficient. Using these parameters, the authors were able to match the observed O_2 IR night airglow limb profiles. Specifically when modeling the O_2 IR night airglow, they keep the atomic oxygen downward flux at 130 km relatively constant near 3.5 x 10^{12} cm^{-2} s^{-1} and vary the eddy diffusion coefficient ($A = 4$ x 10^{12}). *Gérard et al.* (2008c) show one of their selected 1-D model fits for a single orbit. The O density peak obtained when nearly matching the airglow layer is 1.8 x 10^{11} cm^{-3} at 104 km.

The new VTGCM model produces O_2 nightglow intensities and O density values within the ranges stated in *Gérard et al.* (2008c) and *Gérard et al.* (2009b), and is in excellent accord with mean values derived in those studies. The VTGCM nightside O density peaks at 104 km, compared to VEX mean altitude of 102 km (*Soret et al.*, 2009, 2010a), with a value of 3.41 x 10^{11} cm^{-3}, compared to the VEX value of 2 x 10^{11} cm^{-3}. The O_2 nightglow peak volume emission rate produced by the VTGCM is located at ~100 km with an integrated vertical intensity of 1.76 MR, which is located near 00:00 LT. As mentioned earlier, the VTGCM nightglow result is for a yield of 75% in reaction (9); a 100% yield would provide a VTGCM peak vertical intensity of 2.37 MR. Statistically averaged observations reveal the mean peak intensity to be 1.6 MR at 96 km and on average seen at midnight (*Soret et al.*, 2009, 2010a; *Gérard et al.*, 2008c). The VTGCM produces a hemispheric average intensity of 0.51 - 0.63

MR (averged over a limited nightside box) when compared to VEX's 0.47 MR (*Soret et al.*, 2010a). For the VTGCM sensitivity test results, we notice the O_2 IR night airglow layer is controlled by two processes. The altitude is mainly controlled by eddy diffusion and the intensity of the airglow is controlled by the winds. The stronger the winds, the more O is transported from the dayside to the nightside resulting in a more intense emission with a corresponding depletion of O on the dayside.

4.2.4.3 NO UV Nightside Airglow

The third key observation is the NO UV night airglow. *Bougher et al.* (1990) published results for solar minimum simulations from an older version of the VTGCM. The older VTGCM adopted different values for certain parameters and did not include all the updates the new VTGCM has incorporated. A few of the modified parameters are the eddy diffusion coefficient, the RSZ wind profile, chemical reaction rates and reactions, and heating and cooling rates. For details on the updates see Chapter 3. Nevertheless, comparing case 5a from *Bougher et al.* (1990) to the new VTGCM best case can be insightful. Case 5a produced a dayside N-density of 2.6 x 10^7 cm^{-3} at 135 km with a corresponding nightside peak density of 1.8 x 10^8 cm^{-3} at 112 km. This case produced a net dayside column production of 1.05 x 10^9 cm^{-2} s^{-1}. The nightglow dark disk average is 0.156 kR with a peak intensity of 0.42 kR for the (0,1) δ band only. Recall that this δ band is ~20% of the total spectrum and was calculated in order to be comparable with the typical PVO observations.

VEX global maps of the statistical mean NO UV night airglow structure do not yet exist, unlike the O_2 IR night airglow. However, *Gérard et al.* (2008b) employed their 1-D model to simulate individual NO UV nightglow limb profiles, just as for the O_2 IR night airglow. This study used several values for A, the variable prescribed in the calculation for the eddy diffusion coefficient, to reproduce three limb profiles (7.4 x 10^{11}, 4 x 10^{12}, and 0). The downward nitrogen flux at 130 km ranges between 1 x

10^8 cm^{-2} s^{-1} and 4 x 10^9 cm^{-2}s^{-1}, but has a typical value of 2 x 10^9 cm^{-2} s^{-1}. For one specific orbit (Orbit 320), the N(^{4}S) nightside density is 2 x 10^8 cm^{-3} at 122 km (*Gérard et al.*, 2008b). *Cox* (2010) has calculated a hemispheric averaged ~1.2 kR for all bands (δ and γ bands) and identified the mean altitude for the NO UV night airglow to be 114.8±5.8 km, but can vary from 95-132 km (*Gérard et al.*, 2008b; *Cox*, 2010).

The new VTGCM simulates a nightside N(^{4}S) density peak value of 1.37 x 10^8 cm^{-3} at 115 km with a peak volume emission rate of 1.23 x 10^3 (photon cm^{-3} s^{-1}) located at 106 km. The corresponding peak airglow intensity for solar minimum conditions is 1.83 kR for the combined δ and γ bands. This peak intensity is similar to the old VTGCM value (0.42 kR x 5 = 2.1 kR)(*Bougher et al.*, 1990). The simulated peak nightside N(^{4}S) density value is a nearly a factor of 1.5 times smaller than that of *Bougher et al.* (1990) and *Gérard et al.* (2008b) values (1.37 x 10^8 vs 2 x 10^8 cm^{-3}) . The simulated peak airglow altitude (~106 km) is at the lower end of the established range; i.e. the range for the peak altitude is 95-132 km with a mean of 113 km (*Gérard et al.*, 2008b). Abel inversion of 725 deconvolved limb profiles (*Cox*, 2010) indicates that the peak volume emission rate is located at 114.8±5.8 km. The hemispheric averaged intensity on the nightside is 1.2 kR while the VTGCM simulates a smaller intensity of 0.68 kR, but once again similar to the old VTGCM value (*Bougher et al.*, 1990; *Gérard et al.*, 2008b; *Cox*, 2010). Reasonable chemical reaction rate tests (i.e. within established measurement error bars) have been conducted to increase the simulated intensity and raise the nightglow emission layer; little variation of these nightglow features has resulted. The simulated NO UV night airglow distribution shows a maximum near 01:00 LT. The NO UV night airglow peak emission is not shifted closer to 02:00 LT because the NO emission layer is too close in altitude to the O_2 IR emission layer. The calculated separation of these airglow layers is ~7 km and the corresponding RSZ wind change is not dramatic (see Figure 4.5). If the altitude separation of these two airglow layers is increased to 17-20 km, the RSZ wind approach 30 m s^{-1}. This would provide a greater shift in local time for the NO UV nightglow compared to the O_2 IR nightglow.

4.3 Atomic Oxygen Distributions

4.3.1 Introduction

For the O_2 IR and NO UV nightglow features, atomic oxygen plays a major role in the creation of the emissions. Atomic oxygen is formed by CO_2 photolysis and ion-neutral chemical reactions on the dayside and transported by the global circulation to the nightside where it recombines with other chemical species. The O distribution can provide insight into the circulation and, similarly, contribute to the understanding of the night airglow variability. Previously, there have only been very few measurements of Venus thermospheric densities. PVO neutral mass spectrometer in situ measurements were obtained at low latitudes ($\sim \pm 16°$) and above ∼140 km (*Niemann et al.*, 1980). Magellan obtained drag measurements, yielding mass densities, at extratropical latitudes and above ∼130 km (*Keating and Hsu*, 1993). Furthermore, VEX has also performed an atmospheric drag experiment near the South pole and above ∼180 km (*Mueller-Wodarg et al.*, 2008). However, recently, *Soret et al.* (2010a) have deduced a three-dimensional atomic oxygen density map from the statistical O_2 IR nightglow emission map (see Figure 4.11). The hemispheric average density is 1.9 x 10^{11} cm^{-3} and depending on the CO_2 profiles used (VTS3 or SPICAV stellar occultations) the peak altitude is 106.1 km and 103.4 km, respectively. The derived VEX O density map provides the first nightside distribution of Venus' O density (*Soret et al.*, 2010a). Moreover, the statistical O density map and the associated profiles provide constraints for the O_2 IR and NO UV nightglow as well as the inferred circulation. These dynamical implications are investigated using the VTGCM. More details about the derivation of the O density profiles and maps are discussed in section 4.3.2.

In order to bring the new VEX O density map into a global context, the VTGCM will be utilized to provide a self-consistent global view of the O density distributions. More specifically, this study utilizes the VTGCM to reproduce nightside O density profiles and maps derived from VEX observations. The VTGCM results used in this study are extracted from the VTGCM "best case" which represents mean conditions for Venus' middle and upper atmosphere during the VEX sampling period (see Section 4.1). Mean VEX conditions are best captured by VEX statistically averaged mean nightglow emission maps which have been discussed in the previous sections. The goal is to understand the horizontal and vertical distributions of O densities, and their implications for Venus thermospheric dynamics.

4.3.2 Observations and Generation of Statistical Maps

As mentioned in Chapter 2, VEX has observed O_2 IR nightglow with the VIRTIS instrument. In the past, nadir observations have been used to create O_2 IR nightglow statistical maps (*Gérard et al.*, 2008c; *Piccioni et al.*, 2009). These nadir observations are mainly obtained in the southern hemisphere due to the VEX elliptical polar orbit. However, limb observations provide information from the northern hemisphere as a function of altitude and span a limited latitude versus a local time range. Recently, *Soret et al.* (2010a) have compiled nadir and limb profiles to create a more complete statistical emission map of the O_2 IR nightglow.

The nadir observations used to create the emission map are corrected for thermal contributions, emission angles, and backscattering (*Soret et al.*, 2010a). Conversely, the limb observations are vertically integrated after having the inverse Abel transform applied to simulate nadir observations. Combining the corrected nadir observations and the derived emissions from the limb observations results in the statistical O_2 IR nightglow emission map. The maximum bright spot is 1.6 MR and the area weighted

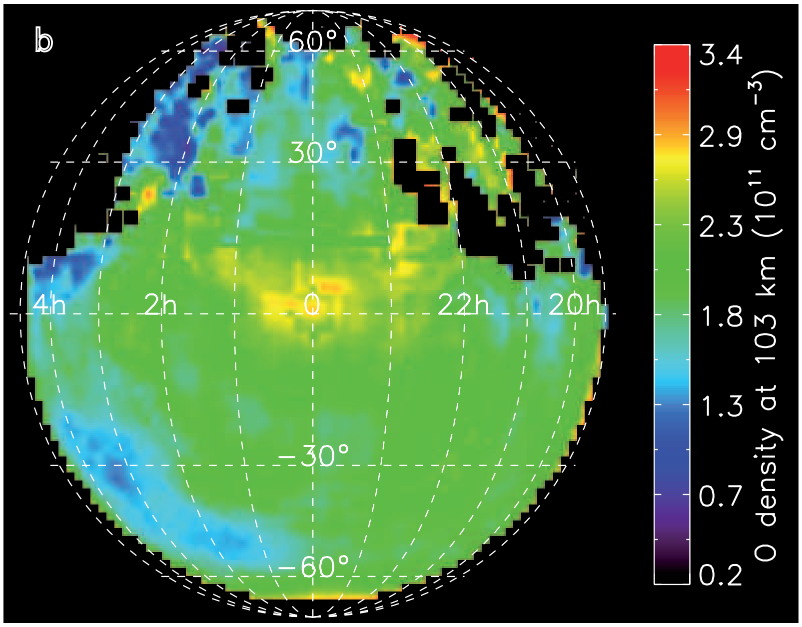

Figure 4.11: Altitude slice at 103 km from the three-dimensional map of atomic oxygen density (cm^{-3}) derived from the VEX O_2 IR nightglow emission map (local time vs latitude) (*Soret et al.*, 2010a). The maximum value is 2.8 x 10^{11} cm^{-3}.

hemispheric average is 0.5 MR (*Soret et al.*, 2010a).

The O_2 IR statistical map helps interpret the mean nightglow emission distribution and intensity as well as the global circulation at a specific location. Furthermore, O density can be derived from the O_2 IR emission map. There are three steps to deriving O density from the observed O_2 IR nightglow map. The first step involves calculating the O_2 ($a^1\Delta$) density and creating a corresponding map from the O_2 IR emission map. The next step requires generation of a CO_2 density map from available CO_2 density profiles. At this time, there are two sets of density profiles which can be used. One set is from the VTS3 empirical model (*Hedin et al.*, 1983). This model is based upon PVO neutral mass spectrometer in situ measurements obtained at low latitudes above ~140 km. The model symmetrically distributes the CO_2 density cylindrically at higher latitudes and uses the hydrostatic equilibrium assumption to extrapolate densities below ~140 km. Alternatively, CO_2 density profiles are obtained using 114 observations from SPICAV stellar occultations, ranging from 80 - 140 km.

SPICAV profiles were averaged within specified 15° bins and assigned an associated solar zenith angle (*Soret et al.*, 2010a). For this study, the referenced VEX O density is derived specifically utilizing the SPICAV CO_2 densities. Finally, once both maps (O_2 ($a^1\Delta$) density and CO_2 density) are assembled, they are used together to derive the O density:

$$[O](z) = \sqrt{[O_2^*](z)\frac{A + C_q[CO_2](z)}{k\varepsilon[CO_2](z)}} \tag{4.1}$$

where [O] is O density in cm^{-3}, z is the distance from the center of Venus in km, $[O_2^*]$ is O_2 ($a^1\Delta$) density in cm^{-3}, A = 2.19 x 10^{-4} s^{-1} is the Einstein coefficient (*Newman et al.*, 1999) for $O_2^* \rightarrow O_2 + h\nu$, C_q = 2 x 10^{-20} cm^{-3} s^{-1} is the quenching coefficient (*Sander and et al.*, 2003) for $O_2^* + CO_2 \rightarrow O_2 + CO_2$, k = 3.1 x 10^{-32} cm^6 s^{-1} is the reaction rate (*Huestis et al.*, 2008) for $O + O + CO_2 \rightarrow O_2^* + CO_2$, and $\varepsilon = 75\%$ is the efficiency for the last equation (see *Soret et al.* (2010a) for more details about equation 1). Equation 4.1 is based on the assumption that three-body recombination ($O+O+CO_2$) is the source of the O_2 ($^1\Delta$) molecules on the nightside. *Soret et al.* (2010a) present an O density map at a given altitude of 103 km, which uses SPICAV CO_2 densities (see Figure 4.11). The corresponding hemispheric area weighted mean O density peak is 1.9 x 10^{11} cm^{-3}. For more details on the derivation of the O density maps and differences between the two sets of CO_2 profiles, see *Soret et al.* (2010a).

4.3.3 Results

4.3.3.1 VTGCM and VEX O density map at 103 km

The VTGCM simulation is conducted for solar minimum conditions, as discussed previously in this chapter. With these parameters, a nightside O density map (latitude vs. longitude) at 103 km is presented in Figure 4.12. This specific altitude was chosen

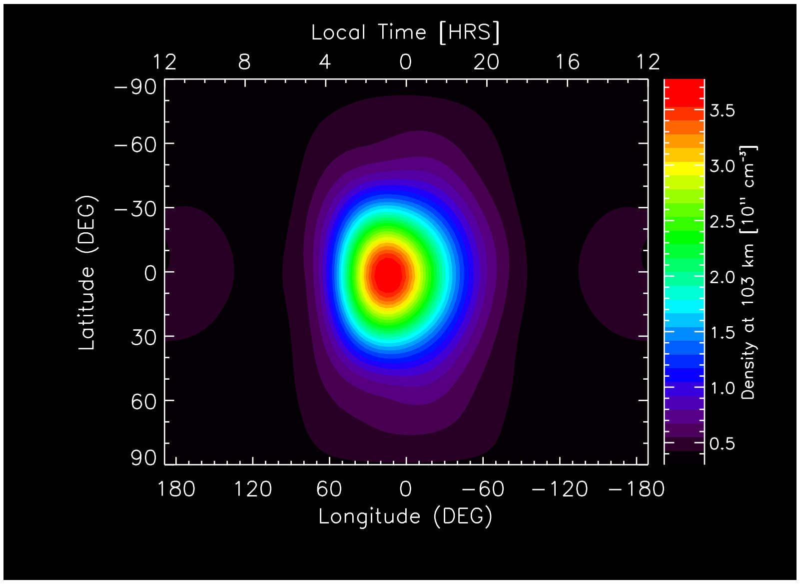

Figure 4.12: VTGCM “mean” case for VEX conditions; altitude slice at 103 km (local time vs latitude) for atomic oxygen density (cm^{-3}). The maximum value = 3.77 x 10^{11} cm^{-3}.

to compare the VEX derived O density peak near 103 km, and the VTGCM peak O density also near 103 km. The nightside O density distribution is a result of the production of O on the dayside and its transport to the nightside by the global wind system. The density map is a global representation of the O distribution at a specific altitude consistent with the combined SS-AS and RSZ wind components captured by the VTGCM.

The VTGCM simulated O density map at 103 km has a maximum value of 3.77 x 10^{11} cm^{-3} at 01:00 LT near the equator and has a corresponding hemispheric area weighted mean of 1.38 x 10^{11} cm^{-3}. Table 4.4 lists density values for specific locations from the VTGCM simulated O density map. The density contour circles symmetrically decrease away from the maximum value near the anti-solar (AS) point. The O density along a contour circle at roughly 60° from the AS point (i.e. 60°N, 60°S, 04:00 LT, and 20:00 LT) displays an average ∼6 fold decrease when compared to the maximum value. Along a 30° contour from the AS point (i.e. 30°N, 30°S, 02:00 LT,

Table 4.4: Density map values at 103 km (cm^{-3}) for specific locations from VTGCM simulation and VEX data

LT / Lat. [hours/°]	VTGCM Density [cm^{-3}]	VEX Density [cm^{-3}]
Max 01/00	3.03×10^{11}	–
Max 00/05	–	2.80×10^{11}
20/00	6.48×10^{10}	2.00×10^{11}
22/00	1.77×10^{11}	1.90×10^{11}
00/00	3.40×10^{11}	2.78×10^{11}
02/00	3.19×10^{11}	1.98×10^{11}
04/00	5.59×10^{10}	1.61×10^{11}
00/30N	1.59×10^{11}	1.78×10^{11}
00/30S	1.89×10^{11}	1.89×10^{11}
00/60N	6.20×10^{10}	1.30×10^{11}
00/60S	5.35×10^{10}	2.01×10^{11}

and 22:00 LT), the O density decreases with respect to the maximum by a factor of ~2. Thus, the O density decreases more rapidly at further distances from the AS point.

The VEX O density map, Figure 4.11, has a maximum density value of 2.8×10^{11} cm^{-3} (excluding extraneous data points) located near ~00:00 LT at 5° latitude with a corresponding hemispheric area weighted mean of 1.9×10^{11} cm^{-3}. Densities for specific locations from the VEX O density map are expressed in table 4.4. At the equator, the O density near 04:00 LT and 20:00 LT decrease away from the AS point by a factor of 1.7 and 1.4 respectively. Conversely, at 60°N, the density decreases by a factor of 2.1 and at 60°S by a smaller factor of 1.4. Thus, closer to the AS point, the density decreases more symmetrically. Moreover, the best comparisons of the VEX and VTGCM O densities are found within 30° of the AS point.

4.3.3.2 VTGCM and VEX O density profiles

Along with the O density map, vertical profiles have been generated for different locations (see Table 4.5) based upon CO_2 densities. Figure 4.13 illustrates CO_2 density profiles from the VTS3 empirical model (solid line with squares), the VTGCM

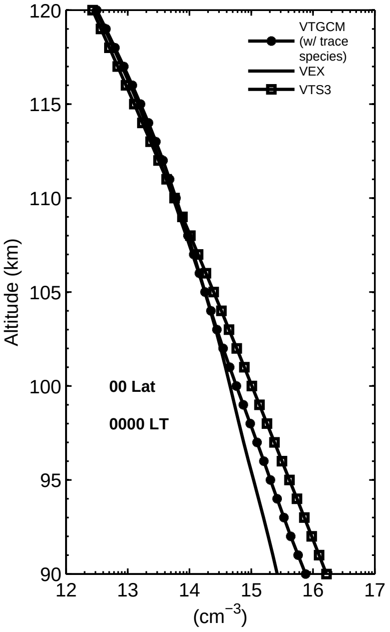

Figure 4.13: Vertical profiles of CO_2 density (cm^{-3}) near the equator at 0000 LT on a log scale. VTGCM "mean" case for VEX conditions with trace species (solid line with dots), VEX-SPICAV CO_2 mean density vertical profiles (solid line), VTS3 CO_2 density vertical profiles (circles).

(solid line with dots), and SPICAV/VEX observations (solid line). The location at which these profiles are displayed is near the equator at midnight. Above ~100 km the three profiles agree reasonably well. However, below ~100 km the CO_2 profiles diverge. At 90 km, the VEX profile and the VTS3 profile are nearly an order of magnitude different. As previously discussed, the VTS3 model is based upon PVO neutral mass spectrometer in situ measurements above ~140 km (*Hedin et al.*, 1983), with extrapolation using the hydrostatic equation to lower altitudes, thus suggesting the VTS3 empirical model is likely to be inaccurate at these lower altitudes. The VTGCM profile lies between the two profiles and is only a factor of ~3.0 larger than VEX densities at 90 km.

Figures 4.14 - 4.17 represent the O density at different locations with the AS point location (0° latitude at 00:00 LT) shown in each figure for comparison. In each plot, there are two profiles from the VTGCM and one from the VEX statistical O

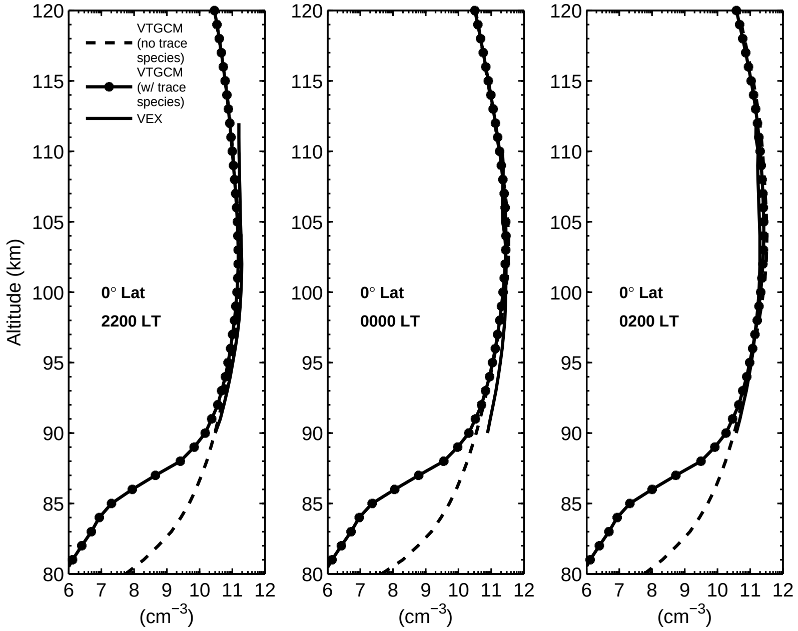

Figure 4.14: Vertical profiles of O density (cm^{-3}) near the equator at different local times, 2200 LT (left), 0000 LT (center), 0200 LT (right), on a log scale. VTGCM "mean" case for VEX conditions with trace species (solid line with dots) and without trace species (dashed line). VEX O density vertical profiles derived from the O density maps (solid line). The VEX profile is given above 90 km due to the limitations of CO_2 (SPICAV) densities.

Table 4.5: Vertical profile density peaks (cm^{-3}) and altitude (km) for VTGCM simulations and VEX data

LT / Lat. [hours/°]	VTGCM Den. Peak [cm^{-3}]	VTGCM Alt. [km]	VEX Den. Peak [cm^{-3}]	VEX Alt. [km]
20/00	8.56×10^{10}	100	2.22×10^{11}	104.5
22/00	1.81×10^{11}	102	1.96×10^{11}	102.5
00/00	3.41×10^{11}	104	2.86×10^{11}	102.5
02/00	3.23×10^{11}	104	2.00×10^{11}	102.5
04/00	1.05×10^{11}	101	1.78×10^{11}	104.5
00/30N	1.55×10^{11}	102	1.83×10^{11}	102.5
00/30S	1.80×10^{11}	102	1.94×10^{11}	102.5
00/45S	1.01×10^{11}	100	1.94×10^{11}	102.5
00/60S	6.75×10^{10}	100	2.23×10^{11}	104.5

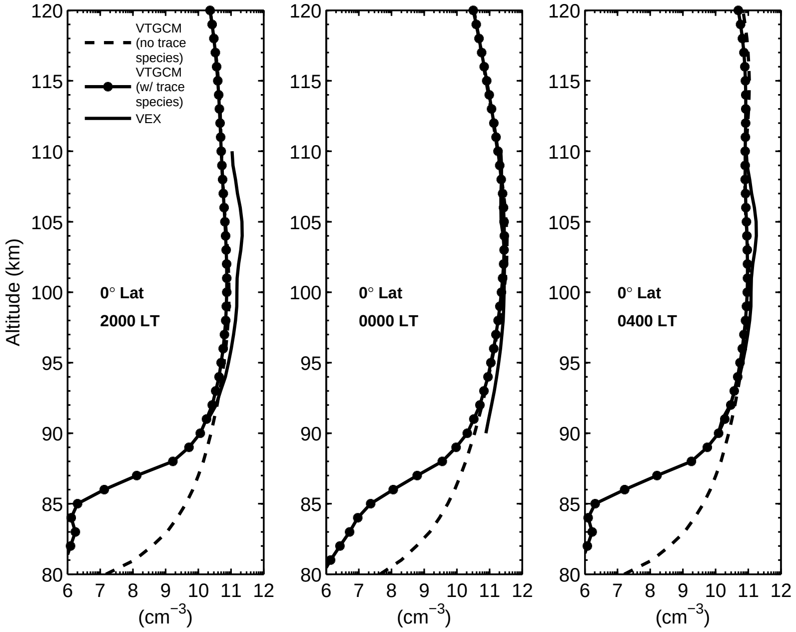

Figure 4.15: Vertical profiles of O density (cm^{-3}) near the equator at different local times, 2000 LT (left), 0000 LT (center), 0400 LT (right), on a log scale. VTGCM "mean" case for VEX conditions with trace species (solid line with dots) and without trace species (dashed line). VEX O density vertical profiles derived from the O density maps (solid line). The VEX profile is given above 90 km due to the limitations of CO_2 (SPICAV) densities.

density map. The solid profile with dots corresponds to the VTGCM simulation with nightside low altitude trace species. The dashed line is the same VTGCM simulation but without the nightside low altitude trace species. The solid profile represents the VEX density. Throughout all locations, the O density profiles without trace species have a similar shape and change slightly compared to the profiles with trace species. This is due to the magnitude of losses, specially below ∼95 km, and the altitude of those losses. Details on the impact nightside trace species have have been discussed earlier in this chapter and in *Brecht et al.* (2010a). It is clear that the trace species are key in reducing the O densities below ∼95 km and the atomic oxygen destruction is seen at all locations. The addition of the trace species gives rise to a more realistic O density profile in the lower thermosphere (*Krasnopolsky*, 2010).

The VTGCM vertical profiles illustrate a similar pattern as the density map, with

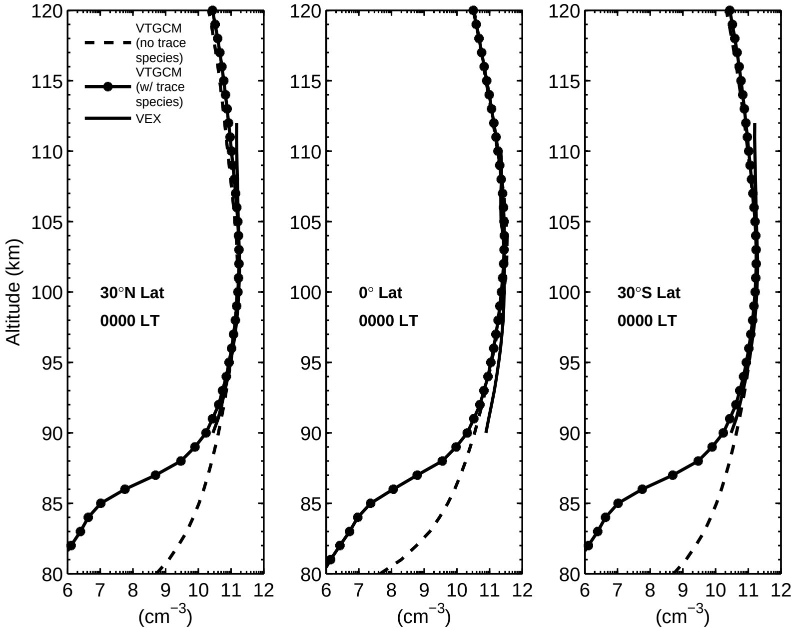

Figure 4.16: Vertical profiles of O density (cm^{-3}) near 0000 LT at different latitudes, 30°N (left), 0° (center), 30°S LT (right), on a log scale. VTGCM "mean" case for VEX conditions with trace species (solid line with dots) and with out trace species (dashed line). VEX O density vertical profiles derived from the O density maps (solid line). The VEX profile is given above 90 km due to the limitations of CO_2 (SPICAV) densities.

density values decreasing away from midnight (see Table 4.5). A ~4 fold enhancement of the peak O density from 20:00 LT to 00:00 LT along the equator is illustrated, while a ~3 fold decrease is shown from 00:00 LT to 04:00 LT along the equator. Moreover, the peak density altitude is maximum at midnight and decreases by ~3 km at locations four hours before and after midnight.

Furthermore, along the midnight meridian, the VTGCM simulates peak density values at 30°N and 30°S that are a factor of nearly two times less than the AS point. Peak density altitudes decrease by ~2 km along the midnight meridian, similar to the decreasing peak density altitude with respect to local time (see Figure 4.16). At 45°S and 60°S (see Figure 4.17), the peak density decreases by a factor of 3.4 and 5.1 from the AS point, respectively. The corresponding peak density altitudes also decrease by 4 km. Overall, the further away from the AS point the greater the rate

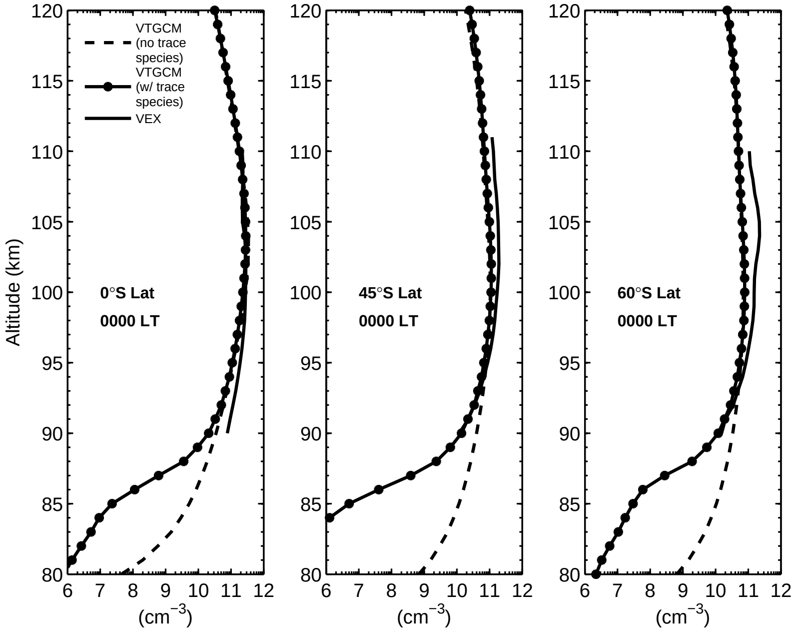

Figure 4.17: Vertical profiles of O density (cm^{-3}) near 0000 LT at different latitudes, 0° (left), 45°S (center), 60°S LT (right), on a log scale. VTGCM "mean" case for VEX conditions with trace species (solid line with dots) and with out trace species (dashed line). VEX O density vertical profiles derived from the O density maps (solid line). The VEX profile is given above 90 km due to the limitations of CO_2 (SPICAV) densities.

of decrease in the O density and its peak altitude.

The VEX O density profiles were derived from the statistical O density map. From 20:00 LT to 00:00 LT the density increases by a factor of 1.3, while from 00:00 LT to 04:00 LT the O density decreases 1.6 times. Along the midnight meridian there is a reduction of ~1.6 at 30 N and 30 S. Even farther from the AS point, the density decreases by a factor of 1.5 at 45°S, and a factor of 1.3 at 60°S. The peak densities from the vertical profiles represent a non-symmetrical distribution around the maximum density value. VEX maximum O density peak altitude increases by 2 km along the equator and away from the AS point; conversely this altitude increases slowly with latitude (0 - 60°S).

4.3.4 Implications for Night Airglow and Thermospheric Circulation

The VTGCM O density map to first order illustrates a similar O density distribution at 103 km as the statistical VEX O density map. The two maps have similar maximum density values near ~3.0 x 10^{11} cm^{-3} and the values are located close to the AS point. The VEX maximum density value is ~00:00 LT at 5°N latitude, while the VTGCM maximum density value is near 01:00 LT at ~0° latitude. Considering a contour circle of 30° from the AS point, both maps show a density decrease of nearly half their maximum density values. However, when considering the contour circle of 60°, the maps start to deviate from one another. The VTGCM O density decreases much more rapidly beyond the 30° contour than the VEX O density. The difference in the distributions suggests the VTGCM is most accurate up to ~30° from the maximum (near the AS point), thereby representing average conditions. Beyond ~30°, the smaller decrease for the VEX O density map implies the actual wind distribution may not vary as strongly as the VTGCM suggests. Along the equator at 103 km, the SS-AS + RSZ winds are $\sim \pm 60$ m s^{-1} at 06:00 and 18:00 LT. However at 04:00 and 20:00 LT the winds decrease to $\sim \pm 20$ m s^{-1}. The dramatic decrease provides a more dramatic change in the O density distribution and does not reflect a more uniform distribution as seen in the VEX O density distribution. Conversely, along the midnight meridian at 60° north and south, the corresponding meridional winds are ± 15 m s^{-1}.

It is important to recognize that the VEX O density map captures a statistically average distribution, while the VTGCM reflects a steady state situation corresponding to mean wind conditions. The VEX O map is created from a conglomerate of many spatially separated O_2 IR nightglow emission bright spots and there may be several simultaneous bright spots. The VEX O map is the average of all these widespread enhancements which may be found almost anywhere on the nightside. By contrast, this VTGCM is a climate model that presently cannot reproduce a wide range of morphological variability using average wind conditions.

Overall, the VTGCM vertical profiles are in very good agreement with the VEX O density profiles (Figures 4.14 - 4.17). Similarly when comparing the maps, the VTGCM is most accurate within a contour of 30° of the AS point. The profiles at 45°S along the midnight meridian are very similar but at 60°S the VTGCM density does not reproduce the VEX density profile. In addition, the altitude of the VTGCM peak O density has an opposite trend to that displayed by the VEX data, i.e. the VTGCM value decreases away from midnight along the equator while the corresponding VEX altitude increases slightly. The VTGCM altitude trend may imply that the simulated middle atmosphere temperatures are too cold away from the AS point. The simulated temperature change from the AS point to ∼60° contour at 103 km decreases from 185 K to 173 K and is in agreement with PV OIR (*Schofield and Taylor*, 1983). However at 90 km, data from PV OIR and the VeRa occultations shows, the temperature increases from ∼175 K to ∼180 from the AS point to 60° along the midnight meridian (*Schofield and Taylor*, 1983; *Pätzold et al.*, 2007). The VTGCM calculates colder temperatures with an opposite trend away from the AS point; i.e. near the AS point the temperature is 162 K and near the 60° contour it is ∼160 K. Nevertheless, for most of the locations, the O density profiles spanning ∼90 km to 110 km agree favorably.

However, a detailed comparison with the VEX O density profiles below ∼90 km and VTGCM is not presently possible. In addition, the VTGCM and VEX-SPICAV CO_2 profiles are different by a factor of 2 at these altitudes. This will cause a discrepancy between the derived O density from VEX and the VTGCM O density profiles. The two VTGCM profiles illustrate a wide separation below ∼95 km when considering trace species. From the VTGCM simulations and *Krasnopolsky* (2010), it is necessary to include trace species in future investigation of the O densities below 95 km.

4.4 Implications from the Double Resolution Examination

The VTGCM, for the first time ever, was run with 2.5° x 2.5° horizontal resolution, 0.25 vertical scale height, and a time-step of 15 seconds to understand the dynamical dependencies on resolution. The finer resolution case will be known as the high resolution (Hi-Res) case, while the original resolution will be know as the low resolution (Low-Res) case. The increase in resolution did provide small differences between the simulated two cases; the most noticeable increase is seen in the terminator zonal winds, shown in Figure 4.18. The Hi-Res case produced larger maximum zonal winds on the evening terminator of 345 m s^{-1} compared to the Low-Res case of 314 m s^{-1}. It also produced larger maximum zonal winds across the morning terminator at -215 m s^{-1} compared to the lower value produced with the Low-Res case, -199 m s^{-1}. The implication is that the Hi-Res case is able to resolve the sharp gradients across the terminators more accurately. The temperature values, overall, remained very similar between the two cases; see Figure 4.18. Yet, a more detailed structure is seen in the Hi-Res case. The O_2 IR nightglow peak volume emission rate increased by a factor of 1.6 and the NO UV nightglow emission increased by a factor of 1.5, shown in Figure 4.19. Correspondingly, the O_2 IR nightglow peak intensity increase from 1.76 MR to 2.52 MR for the Hi-Res case. Additionally, the NO UV nightglow peak intensity increases from 1.83 kR to 2.4 kR. The increase in the nightglow emission is due to the zonal wind increase, which transports the chemistry from the dayside to the nightside to produce the nightglow. The dynamical structure of the emissions is the same between the two cases, except the NO UV emission shows slightly more detail near the 01:00 LT peak. Overall, for examining larger scale features, such as nightglow distributions, the Low-Res is satisfactory. However, for examining small scale features, such as gravity waves and terminator physics, the Hi-Res case is needed. The finer resolution case examination has proven to be a valuable test in understanding the importance of grid size in capturing dynamical features.

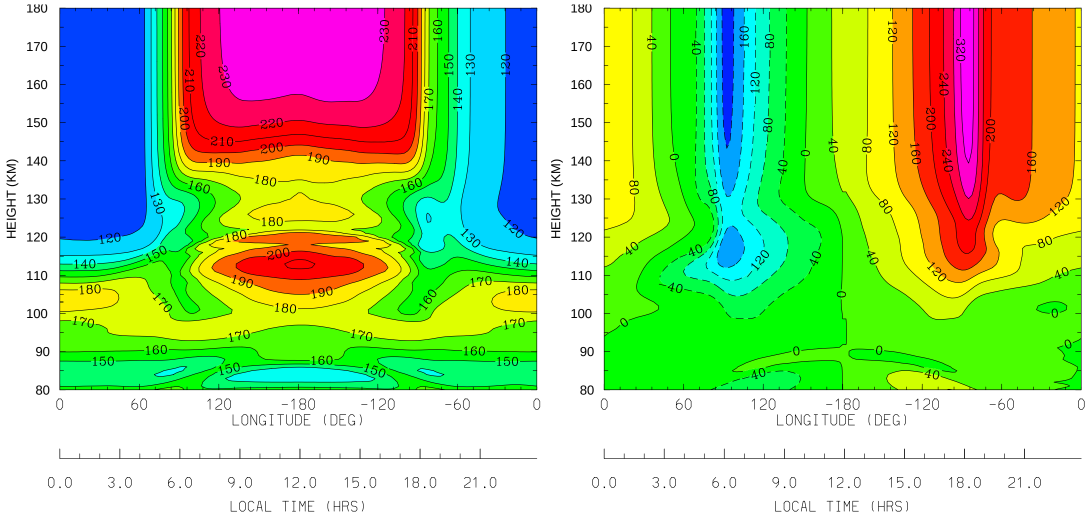

Figure 4.18: VTGCM "mean" case for VEX conditions at 2.5° x 2.5° resolution; longitude-height cross section at 2.5°N (local time vs height). Neutral temperature (K) is on the left side and zonal winds (m s^{-1}) are on the right side.

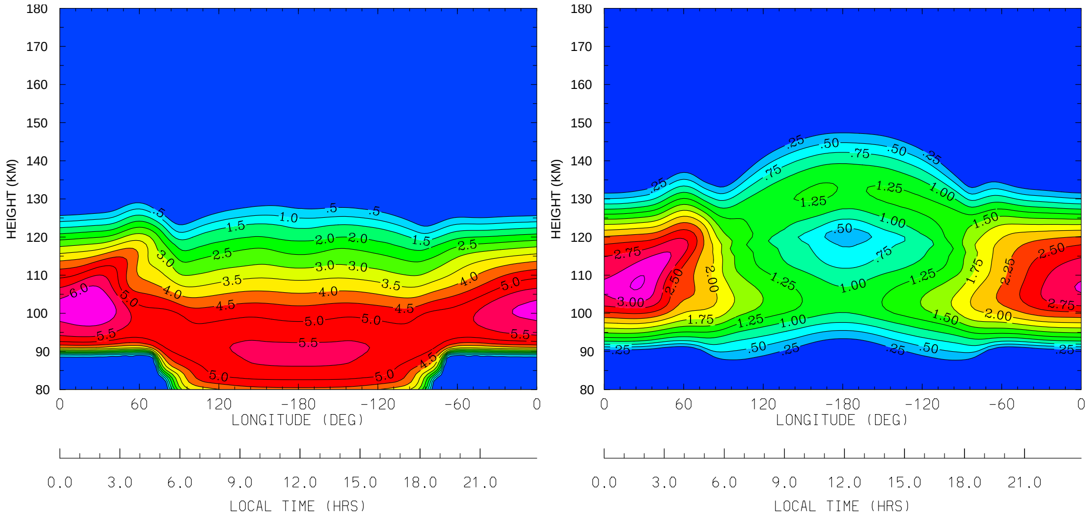

Figure 4.19: VTGCM "mean" case for VEX conditions at 2.5° x 2.5° resolution; longitude-height cross section at 2.5°N (local time vs height). A illustration of the max O_2 IR night airglow volume emission rate close to midnight in the left panel and the max NO UV night airglow volume emission rate close to 01:00 LT in the right panel. The emission rate unit is $\log_{10}$(photons cm^{-3} s^{-1}).

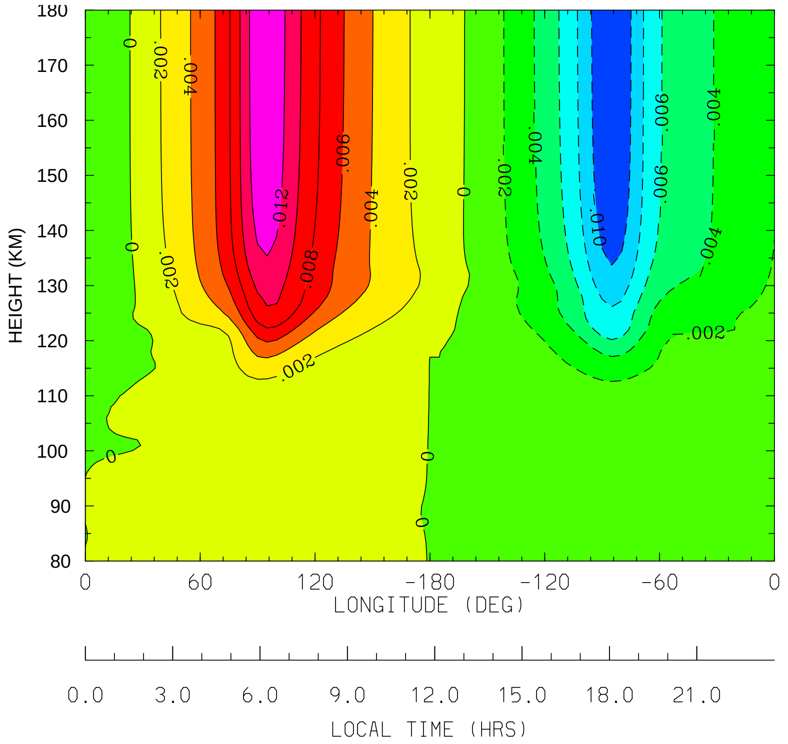

Figure 4.20: VTGCM "mean" case for VEX conditions; longitude-height cross section at 2.5°N (local time vs height) for the zonal drag (m s^{-2}) due to Rayleigh friction. The maximum drag is 0.012 m s^{-2} near 140 km at 06:00 LT.

4.5 Preliminary Study with Gravity Wave Scheme

Chapter 3 provided an introduction to the F-L scheme and the past incorporation into the older VTGCM. In this section, the incorporation of the same F-L scheme into the new VTGCM (5° x 5° grid spacing) is discussed. Similar to *Zhang et al.* (1996), many sensitivity tests have been performed to find the best suite of parameters for a symmetric zonal wind case. The adjustable parameters are the same: the characteristic intrinsic phase speeds for the east (c_e), west (c_w), north (c_n), and south (c_s) components of the gravity waves at the lower boundary (70 km); the gravity wave energy density growth factor (H_E); and the top and bottom boundary of the transition region (z1 and z2).

The calculated symmetrical drag term from the "mean" simulation (using Rayleigh friction as drag), shown in Figure 4.20, provided insight into the magnitude of mo-

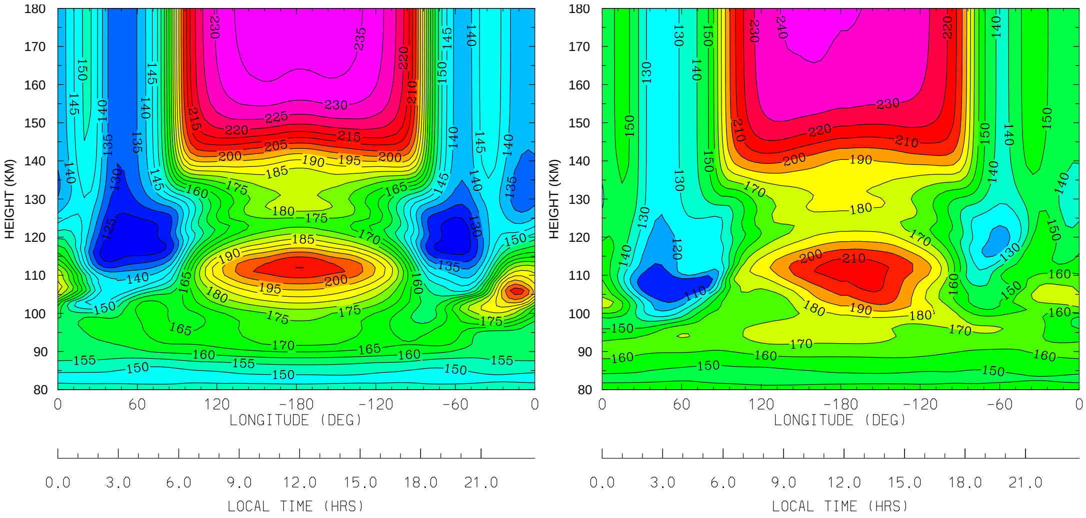

Figure 4.21: VTGCM “mean” case with *Fritts and Lu* (1993) wave drag scheme replacing Rayleigh friction. Both figures are longitude-height cross sections at 2.5°N (local time vs height) illustrating neutral temperature (K). The figure on the left prescribed phase speeds of 6 m s^{-1} and the figure on the right prescribed phase speeds of 8 m s^{-1}.

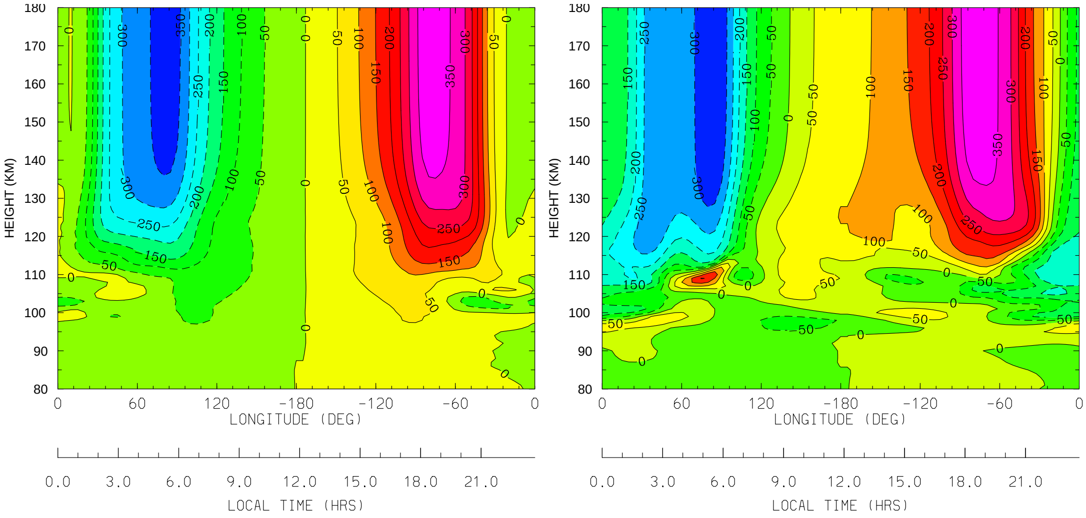

Figure 4.22: VTGCM “mean” case with *Fritts and Lu* (1993) wave drag scheme replacing Rayleigh friction. Both figures are longitude-height cross sections at 2.5°N (local time vs height) illustrating zonal wind (m s^{-1}). The figure on the left prescribed phase speeds of 6 m s^{-1} and the figure on the right prescribed phase speeds of 8 m s^{-1}.

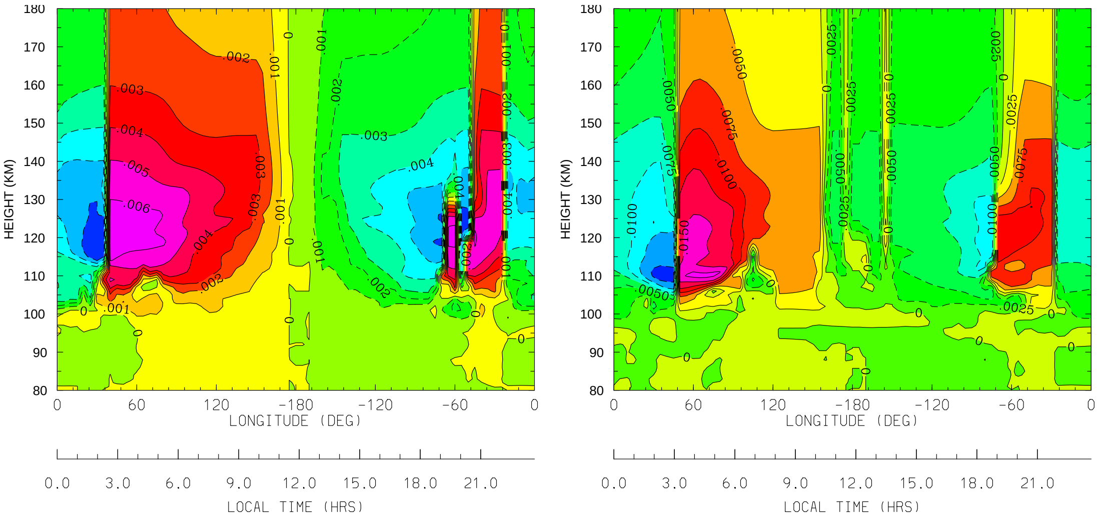

Figure 4.23: VTGCM "mean" case with *Fritts and Lu* (1993) wave drag scheme replacing Rayleigh friction. Both figures are longitude-height cross sections at 2.5°N (local time vs height) illustrating the magnitude of drag (m s^{-1}). The figure on the left prescribed phase speeds of 6 m s^{-1} and the figure on the right prescribed phase speeds of 8 m s^{-1}.

mentum drag needed to produce the appropriate winds and provided insight into the approximate location where the maximum amount of drag is needed. Simulations suggested a wave drag peak magnitude of ∼0.012 m s^{-2} with its deposition between 130 km and 140 km.

The best case generated with the F-L scheme used these chosen parameters: $c_e = c_w = c_n = c_s = 6$ m s^{-1}; 1.8H_E; z1 = 110; and z2 = 125. This case provided exospheric temperatures of 238 K and a night warm spot at 105 km of ∼200 K. A longitude-height cross section at 2.5°N of the temperatures is illustrated in Figure 4.21. Simulated winds speeds are symmetrical across the dayside and reached 380 m s^{-1} maximum at the terminators, shown in Figure 4.22. The corresponding drag deceleration on the terminators are 0.007 m s^{-2} in the altitude range of 115 km to 130 km, shown in Figure 4.23. It is unclear why the drag has "drop outs" and rapidly changes direction. Even in the best case, the simulated F-L scheme, drag is not strong enough; this is consistent with the very warm temperatures near 110 km on the dayside and nightside (see Figure 4.21). However, the tuning of parameters proved to be very difficult and the results were hard to interpret. Specifically, the results from the sensitivity tests did not show obvious trends/correlations between the tuning of any parameter and the corresponding results. To increase the drag (to lower the temperatures in the 110 km region on the dayside and nightside), the phase speeds were all increased to 8 m s^{-1}. The slight change in phase speed produced dramatic and surprising results. For example, the exospheric temperature increased to 241 K and the night warm spot decreased to $\sim$170 km, while the temperature of the warm region on the dayside at 110 km did not change (Figure 4.21). Moreover, the phase speeds are prescribed symmetrically, while the terminator winds have a 50 m s^{-1} difference in magnitude with the maximum zonal velocity on the evening terminator being 380 m s^{-1}. Lastly, the maximum drag is $\sim$0.02 m s^{-1} shown in Figure 4.23.

Incorporating gravity wave parameterization is very important to the development of Venus upper atmosphere modeling. However, the F-L scheme is shown to be to complex and unpredictable. Future work would entail incorporating a different gravity wave parameterization scheme to continue this research. Furthermore, the VTGCM should utilize double resolution to examine the differences in resolving gravity wave momentum deposition effects, especially across the terminators.

CHAPTER V

Conclusions and Future Work

The VTGCM is currently able to provide a self consistent view of Venus' time averaged global dynamics in the middle and upper atmosphere. The validity of the VTGCM and confidence in the results has been demonstrated by detail comparisons between VTGCM simulations and recent spacecraft and groundbased observations. The comparisons were focused upon modeling certain observed dynamical features (e.g. night airglow emissions, the nightside warm spot) that serve as effective tracers of Venus' middle and upper atmosphere global wind system.

The VTGCM simulations have provided new insight into the middle and upper atmospheric flow on Venus. The primary focus for ongoing observations is in the transition region (∼70-120 km), more specifically on the dayside, where the Sun provides the thermal heating and wave sources that drive the thermospheric flow. This region is not accessible by many of the spacecraft instruments, yet the VTGCM has provided insight into the parameters that control the general circulation of the atmosphere. We now know how changes in the external thermal heating affect the thermospheric circulation. In addition, we are starting to understand the impacts the warm lower atmosphere has on the upper atmosphere. The simulations have also provided insight into regions of the VTGCM that are in need of more realistic boundary conditions. In the following subsection the findings of this dissertation research are summarized.

5.1 Conclusions on VTGCM Mean Simulation

With the VTGCM successfully representing mean VEX observations, sensitivity studies were performed with the two tunable parameters (nightside eddy diffusion coefficient and the wave drag term). The results of the sensitivity studies implied that there were at least two sources of variability (eddy diffusion and the global wind system) impacting nightside emissions. It is noteworthy that dynamical consequences of the eddy diffusion variability and the global wind variability can only be simulated utilizing a multi-dimensional dynamical model. The two sources of variability did not always impact both night airglow emissions equally. The VTGCM simulations clearly showed eddy diffusion dominates the region where O_2 IR nightglow emission peaks and the vertical wind dominated the region where NO UV nightglow peaked, both near midnight. These responses revealed why the two nightglow layers should vary independently of each other. *Gérard et al.* (2009b) measured the O_2 IR and NO UV night airglows simultaneously and did not find a spatial correlation between the two airglow emissions. They explained this lack of correlation by the two different wind regimes encountered by the separate airglow layers. In VTGCM simulations, it is crucial to prescribe a very weak RSZ wind below ∼110 km and a rapidly growing RSZ wind above ∼110 km to ∼130 km in order to model the nightglow peak emissions at the observed local times. The VTGCM demonstrated why this non-correlation of the two nightglow layers exists, provided that the distinct airglow layers are separated in altitude by at least ∼15 km.

5.2 Conclusions on Atomic Oxygen Distributions

Overall, the VTGCM simulated O densities within ∼30-45° of the AS point agreed favorably with VEX observations. However, the VTGCM O density decreased more rapidly beyond 45° than VEX observations. This discrepancy implied the combined SS-AS and RSZ wind distribution in the VTGCM may be too strong and/or the underlying middle atmosphere temperatures outside the equatorial zone were too cold. A comparison of VTGCM and VEX profiles below ∼90 km is not possible due to the problem of extending VEX profiles below 90 km using uncertain CO_2 densities. Further, the VTGCM indicates that trace species become important in controlling the O density below ∼95 km and this is not well represented in the VEX profiles at this time.

The VTGCM was expected to correspond closely to VEX observations because of the favorable agreement between the model and the observed O_2 IR nightglow emission. The O density comparison, in fact, did provide confirmation of the simulated O_2 IR nightglow emission results from *Brecht et al.* (2010a). Moreover, the time averaged SS-AS and RSZ wind components simulated by the VTGCM in the lower thermosphere are entirely sufficient to capture the VEX O distribution and the associated O_2 IR nightglow emission within 30° - 45° of the AS point. This examination provides reasonable confirmation of the simulated global wind system simulated by the VTGCM for mean conditions.

5.3 Conclusions on VTGCM Numerical and Physical Improvements

The numerical convergence of these VTGCM results was tested by running a high resolution simulation where the cell size was decreased by a factor of two (with respect to the standard simulations) in each dimension. The results indicated that standard resolution used to obtain the results presented in this dissertation was sufficient for the airglow distribution studies undertaken. However, a higher resolution scheme will be necessary for the next generation of modeling activities addressing a gravity wave momentum deposition scheme and terminator features.

Although the VTGCM has been benchmarked and produces results within observational ranges, it is clear that numerical and physical improvements need to be made. The incorporation of a gravity wave momentum deposition scheme to replace Rayleigh friction is a much needed improvement. However, it was necessary to first test the resolution of the VTGCM before exploring the detailed impacts of gravity waves; i.e. the model must be capable of resolving gravity wave effects. The high resolution case proved the low resolution case inadequate to resolve smaller scale features, especially along the terminators. Lastly, a modern gravity wave momentum deposition scheme is important to incorporate into the VTGCM. Initially, the F-L scheme replaced the Rayleigh friction parameterization, incorporated similarly to *Zhang et al.* (1996). For the current VTGCM, this scheme proved to be very difficult to use. As shown in Chapter 4, the model was very sensitive to slight parameter changes and the changes were erratic. However, coupling the lower and upper atmosphere of Venus is important to address. Gravity wave momentum deposition is a key element in this coupling.

5.4 Future Work

This dissertation work has provided a platform to begin new studies in understanding the dynamics in Venus' upper atmosphere. Furthermore, VEX is continuing to make observations that are contributing to a better understanding of Venus' global dynamics in the middle and upper atmosphere. Thus, the most evident future research paths are listed below.

1. **Lower Boundary - Wave Studies.** Studying wave mechanisms at the lower boundary of the VTGCM (near ∼70 km) has been started and allows exploration of possible drivers for the varying wind system in the upper atmosphere. A different gravity wave momentum deposition scheme should be modified and implemented for Venus, such as the Global Scale Wave Model used in NCAR Earth models (*Garcia and Solomon*, 1985) and used to perform sensitivity tests. Moreover, an examination of the observed gravity wave parameters provided by VEX should continue (e.g. *Sánchez-Lavega et al.*, 2008; *Garcia et al.*, 2009), since this would provide needed constraints for the scheme . Along with the gravity wave scheme, an examination of other waves being launched from the VTGCM lower boundary should be inspected to understand their impact upon the global wind system. These additional lower boundary waves would include planetary waves and Kelvin waves. Lower boundary wave amplitudes and phase speeds will be prescribed based upon existing independent models of the lower atmosphere (<80 km).

2. **CO and Temperature Global Distributions.** Similar to the O density distributions, comparison of observed CO and temperature global distributions will provide constraints for the VTGCM and help elucidate the day to night wind patterns at specific altitudes. Currently, VEX and ground-based observations are becoming available for this study (*Clancy et al.*, 2008; *Vandaele et al.*, 2008; *Sonnabend et al.*, 2010).

3. **Low Altitude Trace Species.** In the oxygen density distribution examination, it was noted that the presence of trace species made a noticeable impact on the density profiles. However, the trace species were only prescribed on the nightside. It would be important to test the full global impact of the trace species by adding dayside and nightside profiles from the same 1-D model.

Oxygen density is a very important constituent in Venus' atmosphere, when examining nightglow (e.g. O_2 IR, NO UV, and OH IR) which provides constraints on the global wind system.

4. **OH IR Night Airglow.** The OH IR nightglow has been observed at Venus and is seen in the altitude range of 90 to 100 km, similar to the O_2 IR nightglow (*Piccioni et al.*, 2008; *Krasnopolsky*, 2010). Adding the OH IR nightglow into the VTGCM would be important in validating our understanding of the dynamics in the middle atmosphere of Venus, such as the NO UV and the O_2 IR nightglow.

5. **Upper Boundary - Ion Loss and Ion Precipitation.** Currently the VTGCM's upper boundary does not incorporate coupling to the space environment. It would be useful to improve this boundary to evaluate the impacts the space environment has on the neutral atmosphere. A boundary which provides accurate ion densities and ion flow would focus upon the impacts and strengths of ion-neutral drag. Another quantity would be ion and/or electron precipitation; i.e. understanding where the ion/electron precipitation distributes its energy and how does this additional energy impact the neutral system. Most of this information can be provided by Magnetohydrodynamic model (MHD) and/or a Hybrid model simulations (e.g. *Brecht and Ferrante*, 1991; *Kallio et al.*, 2006). Currently there is a multi-fluid MHD model for Mars which is being applied to Venus (*Najib*, 2010). In addition, the VTGCM would serve to provide a more accurate 3-D neutral atmosphere for the MHD code, i.e. replace the simplified reference atmosphere currently being used.

In summary, the VTGCM has been improved and tested against spacecraft and ground-based observations. The simulations have provided new insights into the global thermospheric circulation of Venus. Additionally, these new insights have led to new questions and research opportunities concerning the very unique planet, Venus.

BIBLIOGRAPHY

BIBLIOGRAPHY

Alexander, M. J. (1992), A mechanism for the Venus thermospheric superrotation, *Geophys. Res. Lett*, *19*, 2207–2210, doi:10.1029/92GL02110.

Alexander, M. J., A. I. F. Stewart, S. C. Solomon, and S. W. Bougher (1993), Local time asymmetries in the Venus thermosphere, *J. Geophys. Res.*, *98*, 10,849–10,871, doi:10.1029/93JE00538.

Allen, D., D. Crisp, and V. Meadows (1992), Variable oxygen airglow on Venus as a probe of atmospheric dynamics, *Nature*, *359*, 516–519, doi:10.1038/359516a0.

Anderson, D. E., Jr. (1976), The Mariner 5 ultraviolet photometer experiment - Analysis of hydrogen Lyman alpha data, *J. Geophys. Res.*, *81*, 1213–1216, doi:10.1029/JA081i007p01213.

Asselin, R. (1972), Frequency filter for time integrations, *Monthly Weather Review*, *100*(6), 487–490, doi:10.1175/1520-0493(1972)100<0487:FFFTI>2.3.CO;2.

Avduevskii, V. S., et al. (1976), Preliminary results of an investigation of the light regime in the atmosphere and on the surface of Venus, *Kosmicheskie Issledovaniia*, *14*, 735–742.

Bailey, J., S. Chamberlain, D. Crisp, and V. S. Meadows (2008), Near infrared imaging spectroscopy of Venus with the Anglo-Australian Telescope, *Planet. Space Sci.*, *56*, 1385–1390, doi:10.1016/j.pss.2008.03.006.

Banks, P. M., and G. Kockarts (1973), Aeronomy., in *Aerospace UK*, edited by Banks, P. M. & Kockarts, G.

Barth, C. A. (1968), Interpretation of the Mariner 5 Lyman alpha measurements., *Journal of Atmospheric Sciences*, *25*, 564–567, doi:10.1175/1520-0469(1968)025<0564:IOTMLA>2.0.CO;2.

Barth, C. A., J. B. Pearce, K. K. Kelly, L. Wallace, and W. G. Fastie (1967), Ultraviolet Emissions Observed near Venus from Mariner V, *Science*, *158*, 1675–1678, doi:10.1126/science.158.3809.1675.

Bauer, S. J., and R. E. Hartle (1974), Venus ionosphere: an interpretation of Mariner 10 observations., *Geophys. Res. Lett.*, *1*, 7–10, doi:10.1029/GL001i001p00007.

Baulch, D. L., D. Drysdale, D. G. Horne, and A. C. Lloyd (1973), Homoeneous gas phase reactions of the H_2-N_2-O_2 system, in *Evaluated Kinetic Data for High Temperature Reactions*, vol. 2, pp. 1–557, Chemical Rubber Company Press, Cleveland, Ohio.

Bell, J. M. (2008), The dynamics in the upper atmospheres of Mars and Titan, Ph.D. thesis, University of Michigan.

Belton, M. J. S., G. R. Smith, D. A. Elliott, K. Klaasen, and G. E. Danielson (1976a), Space-time relationships in the UV markings on Venus, *Journal of Atmospheric Sciences*, *33*, 1383–1393, doi:10.1175/1520-0469(1976)033<1383:STRITU>2.0.CO;2.

Belton, M. J. S., G. R. Smith, G. Schubert, and A. D. del Genio (1976b), Cloud Patterns, Waves, and Convection in the Venus Atmosphere, in *Bulletin of the American Astronomical Society*, *Bulletin of the American Astronomical Society*, vol. 8, pp. 486–+.

Belton, M. J. S., G. R. Smith, G. Schubert, and A. D. del Genio (1976c), Cloud patterns, waves and convection in the Venus atmosphere, *Journal of Atmospheric Sciences*, *33*, 1394–1417, doi:10.1175/1520-0469(1976)033<1394:CPWACI>2.0.CO;2.

Bertaux, J., et al. (2007), A warm layer in Venus' cryosphere and high-altitude measurements of HF, HCl, H_2O and HDO, *Nature*, *450*, 646–649, doi:10.1038/nature05974.

Bougher, S. W. (1985), Venus Thermospheric Circulation., Ph.D. thesis, The University of Michigan.

Bougher, S. W., and W. J. Borucki (1994), Venus O_2 visible and IR nightglow: Implications for lower thermosphere dynamics and chemistry, *J. Geophys. Res.*, *99*, 3759–3776, doi:10.1029/93JE03431.

Bougher, S. W., R. E. Dickinson, E. C. Ridley, R. G. Roble, A. F. Nagy, and T. E. Cravens (1986), Venus mesosphere and thermosphere. II - Global circulation, temperature, and density variations, *Icarus*, *68*, 284–312, doi:10.1016/0019-1035(86)90025-4.

Bougher, S. W., R. G. E. Roble, R. E. Dickinson, and E. C. Ridley (1988), Venus mesosphere and thermosphere. III - Three-dimensional general circulation with coupled dynamics and composition, *Icarus*, *73*, 545–573, doi:10.1016/0019-1035(88)90064-4.

Bougher, S. W., J.-C. Gérard, A. I. F. Stewart, and C. G. Fesen (1990), The Venus nitric oxide night airglow - Model calculations based on the Venus Thermospheric General Circulation Model, *J. Geophys. Res.*, *95*, 6271–6284, doi:10.1029/JA095iA05p06271.

Bougher, S. W., M. J. Alexander, and H. G. Mayr (1997), Upper Atmosphere Dynamics: Global Circulation and Gravity Waves, in *Venus II: Geology, Geophysics, Atmosphere, and Solar Wind Environment*, edited by S. W. Bougher, D. M. Hunten, & R. J. Phillips, pp. 259 –291.

Bougher, S. W., S. Engel, R. G. Roble, and B. Foster (1999), Comparative terrestrial planet thermospheres 2. Solar cycle variation of global structure and winds at equinox, *J. Geophys. Res.*, *104*, 16,591–16,611, doi:10.1029/1998JE001019.

Bougher, S. W., R. G. Roble, and T. Fuller-Rowell (2002), Simulations of the Upper Atmospheres of the Terrestrial Planets, in *Atmospheres in the Solar System: Comparative Aeronomy; AGU Geophysical Monogragh 130*, edited by Mendillo, M., Nagy, A., & Waite, J. H., pp. 261–288.

Bougher, S. W., S. Rafkin, and P. Drossart (2006), Dynamics of the Venus upper atmosphere: Outstanding problems and new constraints expected from Venus Express, *Planet. Space Sci.*, *54*, 1371–1380, doi:10.1016/j.pss.2006.04.023.

Bougher, S. W., P. Blelly, M. Combi, J. L. Fox, I. Mueller-Wodarg, A. Ridley, and R. G. Roble (2008), Neutral Upper Atmosphere and Ionosphere Modeling, *Space Science Reviews*, *139*, 107–141, doi:10.1007/s11214-008-9401-9.

Brace, L. H., and A. J. Kliore (1991), The structure of the Venus ionosphere, *Space Science Reviews*, *55*, 81–163, doi:10.1007/BF00177136.

Brace, L. H., H. A. Taylor, Jr., T. I. Gombosi, A. J. Kliore, W. C. Knudsen, and A. F. Nagy (1983), The ionosphere of Venus - Observations and their interpretation, in *Venus*, edited by Hunten, D. M., Colin, L., Donahue, T. M., & Moroz, V. I., pp. 779–840.

Brecht, A., S. Bougher, S. Rafkin, and B. Foster (2007), Venus Upper Atmosphere Winds Traced by Night Airglow Distributions: NCAR VTGCM Simulations, *AGU Fall Meeting Abstracts*.

Brecht, A., S. W. Bougher, C. D. Parkinson, Y. L. Yung, and S. C. Rafkin (2009), Understanding the Variability of Nightside Temperatures and Airglow Emissions in Venus' Middle and Upper Atmosphere: NCAR VTGCM Simulations, *AGU Fall Meeting Abstracts*, p. A1267.

Brecht, A. S., S. Bougher, J.-C. Gérard, C. D. Parkinson, S. Rafkin, and B. Foster (2010a), Understanding the Variability of Nightside Temperatures, NO UV and O_2 IR Nightglow Emissions in the Venus Upper Atmosphere, *Journal of Geophysical Research (Planets), Submitted*.

Brecht, A. S., S. Bougher, J.-C. Gérard, and L. Soret (2010b), Atomic Oxygen Distributions in the Venus Thermosphere: Comparisons Between VEX VIRTIS Observations and NCAR VTGCM Simulations, *Icarus, Submitted*.

Brecht, S. H., and J. R. Ferrante (1991), Global hybrid simulation of unmagnetized planets - Comparison of Venus and Mars, *J. Geophys. Res.*, *96*, 11,209–11,220, doi:10.1029/91JA00671.

Broadfoot, A. L., S. Kumar, M. J. S. Belton, and M. B. McElroy (1974), Ultraviolet Observations of Venus from Mariner 10: Preliminary Results, *Science*, *183*, 1315–1318, doi:10.1126/science.183.4131.1315.

Campbell, I. M., and C. N. Gray (1973), Rate constants for O(^{3}P) recombination and association with N(^{4}S), *Chemical Physics Letters*, *18*, 607–609, doi:10.1016/0009-2614(73)80479-8.

Campbell, I. M., and B. A. Thrush (1966), Behaviour of carbon dioxide and nitrous oxide in active nitrogen, *Trans. Faraday Soc.*, *62*, 3366–3374.

Carpenter, R. L. (1964), Symposium on Radar and Radiometric Observations of Venus during the 1962 Conjunction: Study of Venus by CW radar, *AJ*, *69*, 2–11, doi:10.1086/109220.

Clancy, R. T., and D. O. Muhleman (1985), Diurnal CO variations in the Venus mesosphere from CO microwave spectra, *Icarus*, *64*, 157–182, doi:10.1016/0019-1035(85)90084-3.

Clancy, R. T., and D. O. Muhleman (1991), Long-term (1979-1990) changes in the thermal, dynamical, and compositional structure of the Venus mesosphere as inferred from microwave spectral line observations of C-12O, C-13O, and CO-18, *Icarus*, *89*, 129–146, doi:10.1016/0019-1035(91)90093-9.

Clancy, R. T., B. J. Sandor, and G. H. Moriarty-Schieven (2003), Observational definition of the Venus mesopause: vertical structure, diurnal variation, and temporal instability, *Icarus*, *161*, 1–16, doi:10.1016/S0019-1035(02)00022-2.

Clancy, R. T., B. J. Sandor, and G. H. Moriarty-Schieven (2008), Venus upper atmospheric CO, temperature, and winds across the afternoon/evening terminator from June 2007 JCMT sub-millimeter line observations, *Planet. Space Sci.*, *56*, 1344–1354, doi:10.1016/j.pss.2008.05.007.

Colin, L. (1980), The Pioneer Venus Program, *J. Geophys. Res.*, *85*, 7575–7598, doi:10.1029/JA085iA13p07575.

Colin, L. (1983), Basic facts about Venus, in *Venus*, edited by Hunten, D. M., Colin, L., Donahue, T. M., & Moroz, V. I., pp. 10–26.

Colin, L., and C. F. Hall (1977), The Pioneer Venus program, *Space Science Review*, *20*, 283–306, doi:10.1007/BF02186467.

Colin, L., and D. M. Hunten (1977), 11. Pioneer venus experiment descriptions, *Space Science Review*, *20*, 451–525, doi:10.1007/BF02186463.

Collet, A., C. Cox, and J. C. Gérard (2010), Two-dimensional time-dependent model of the transport of minor species in the Venus night side upper atmosphere, *Planet. Space Sci.*, doi:10.1016/j.pss.2010.08.016 in press.

Connes, P., J. F. Noxon, W. A. Traub, and N. P. Carleton (1979), $O_2(^1\ \Delta)$ emission in the day and night airglow of Venus, *Astrophys. J.*, *233*, L29–L32, doi: 10.1086/183070.

Counselman, C. C., S. A. Gourevitch, R. W. King, G. B. Loriot, and E. S. Ginsberg (1980), Zonal and meridional circulation of the lower atmosphere of Venus determined by radio interferometry, *J. Geophys. Res.*, *85*, 8026–8030, doi: 10.1029/JA085iA13p08026.

Covey, C., and G. Schubert (1982), Planetary-scale waves in the Venus atmosphere, *Journal of Atmospheric Sciences*, *39*, 2397–2413, doi:10.1175/1520-0469(1982)039<2397:PSWITV>2.0.CO;2.

Covey, C. C., and G. Schubert (1981a), Mesoscale convection in the clouds of Venus, *Nature*, *290*, 17–20, doi:10.1038/290017a0.

Covey, C. C., and G. Schubert (1981b), 4-day waves in the Venus atmosphere, *Icarus*, *47*, 130–138, doi:10.1016/0019-1035(81)90097-X.

Cox, C. (2010), Analyse et modélisation des émissions ultraviolettes de l'atmosphère de Vénus et de Mars à l'aide des instruments SPICAM et SPICAV, Ph.D. thesis, Université de Liège.

Crisp, D., V. S. Meadows, B. Bézard, C. de Bergh, J. Maillard, and F. P. Mills (1996), Ground-based near-infrared observations of the Venus nightside: 1.27-μm $O_2(a\Delta_g)$ airglow from the upper atmosphere, *J. Geophys. Res.*, *101*, 4577–4594, doi:10.1029/95JE03136.

Dalgarno, A., J. F. Babb, and Y. Sun (1992), Radiative association in planetary atmospheres, *Planet. Space Sci.*, *40*, 243–246, doi:10.1016/0032-0633(92)90062-S.

del Genio, A. D., and W. Zhou (1996), Simulations of Superrotation on Slowly Rotating Planets: Sensitivity to Rotation and Initial Condition, *Icarus*, *120*, 332–343, doi:10.1006/icar.1996.0054.

del Genio, A. D., W. Zhou, and T. P. Eichler (1993), Equatorial superrotation in a slowly rotating GCM - Implications for Titan and Venus, *Icarus*, *101*, 1–17, doi: 10.1006/icar.1993.1001.

Deng, Y., A. D. Richmond, A. J. Ridley, and H. Liu (2008), Assessment of the non-hydrostatic effect on the upper atmosphere using a general circulation model (GCM), *Geophys. Res. Lett.*, *35*, L01,104, doi:10.1029/2007GL032182.

Dickinson, R. E. (1972), Infrared radiative heating and cooling in the Venusian mesosphere. I. Global mean radiative equilibrium., *Journal of Atmospheric Sciences*, *29*, 1531–1556, doi:10.1175/1520-0469(1972)029<1531:IRHACI>2.0.CO;2.

Dickinson, R. E. (1976), Venus mesosphere and thermosphere temperature structure. I - Global mean radiative and conductive equilibrium, *Icarus*, *27*, 479–493, doi: 10.1016/0019-1035(76)90164-0.

Dickinson, R. E., and S. W. Bougher (1986), Venus mesosphere and thermosphere. I - Heat budget and thermal structure, *J. Geophys. Res.*, *91*, 70–80, doi: 10.1029/JA091iA01p00070.

Dickinson, R. E., and E. C. Ridley (1972), Numerical solution for the composition of a thermosphere in the presence of a steady subsolar to-antisolar circulation with application to venus, *Journal of the Atmospheric Sciences*, *29*(8), 1557–1570, doi: 10.1175/1520-0469(1972)029<1557:NSFTCO>2.0.CO;2.

Dickinson, R. E., and E. C. Ridley (1975), A numerical model for the dynamics and composition of the Venusian thermosphere, *Journal of Atmospheric Sciences*, *32*, 1219–1231, doi:10.1175/1520-0469(1975)032<1219:ANMFTD>2.0.CO;2.

Dickinson, R. E., and E. C. Ridley (1977), Venus mesosphere and thermosphere temperature structure. II - Day-night variations, *Icarus*, *30*, 163–178, doi:10.1016/0019-1035(77)90130-0.

Dickinson, R. E., E. C. Ridley, and R. G. Roble (1981), A three-dimensional general circulation model of the thermosphere, *J. Geophys. Res.*, *86*, 1499–1512, doi: 10.1029/JA086iA03p01499.

Donnelly, R. F., and J. H. Pope (1973), The 1-3000 *Å* solar flux for a moderate level of solar activity for use in modeling the ionosphere and upper atmosphere, in *The 1-3000 Å solar flux for a moderate level of solar activity for use in modeling the ionosphere and upper atmosphere*, edited by Donnelly, R. F. & Pope, J. H.

Drossart, P., et al. (2007), Scientific goals for the observation of Venus by VIRTIS on ESA/Venus express mission, *Planet. Space Sci.*, *55*, 1653–1672, doi: 10.1016/j.pss.2007.01.003.

Fjeldbo, G., B. Seidel, D. Sweetnam, and T. Howard (1975), The Mariner 10 radio occultation measurements of the ionosphere of Venus, *Journal of Atmospheric Sciences*, *32*, 1232–1236, doi:10.1175/1520-0469(1975)032<1232:TMROMO>2.0.CO;2.

Fox, J. L. (1988), Heating efficiencies in the thermosphere of Venus reconsidered, *Planet. Space Sci.*, *36*, 37–46, doi:10.1016/0032-0633(88)90144-4.

Fox, J. L. (1994), Rate coefficient for the reaction N + NO, *J. Geophys. Res.*, *99*, 6273–6276, doi:10.1029/93JA03299.

Fox, J. L., and A. Dalgarno (1981), Ionization, luminosity, and heating of the upper atmosphere of Venus, *J. Geophys. Res.*, *86*, 629–639, doi:10.1029/JA086iA02p00629.

Fox, J. L., and A. J. Kliore (1997), Ionosphere: Solar Cycle Variations, in *Venus II: Geology, Geophysics, Atmosphere, and Solar Wind Environment*, edited by S. W. Bougher, D. M. Hunten, & R. J. Phillips, pp. 161–188.

Fox, J. L., and K. Y. Sung (2001), Solar activity variations of the Venus thermosphere/ionosphere, *J. Geophys. Res.*, *106*, 21,305–21,336, doi:10.1029/2001JA000069.

Fox, J. L., M. I. Galand, and R. E. Johnson (2008), Energy Deposition in Planetary Atmospheres by Charged Particles and Solar Photons, *Space Science Reviews*, *139*, 3–62, doi:10.1007/s11214-008-9403-7.

Fritts, D. C., and W. Lu (1993), Spectral estimates of gravity wave energy and momentum fluxes. Part 2: Parameterization of wave forcing and variability, *Journal of Atmospheric Sciences*, *50*, 3695–3713, doi:10.1175/1520-0469(1993)050<3695:SEOGWE>2.0.CO;2.

Gabsi, Y., J. L. Bertaux, A. Hauchecorne, J. Schmitt, and S. Guibert (2008), Measuring Venus' winds using the Absolute Astronomical Accelerometer: Solid super-rotation model of Venus' clouds, *Planet. Space Sci.*, *56*, 1454–1466, doi:10.1016/j.pss.2008.07.016.

Garcia, R. F., P. Drossart, G. Piccioni, M. López-Valverde, and G. Occhipinti (2009), Gravity waves in the upper atmosphere of Venus revealed by CO_2 nonlocal thermodynamic equilibrium emissions, *Journal of Geophysical Research (Planets)*, *114*(E00B32), doi:10.1029/2008JE003073.

Garcia, R. R., and S. Solomon (1985), The effect of breaking gravity waves on the dynamics and chemical composition of the mesosphere and lower thermosphere, *J. Geophys. Res.*, *20*, 3850–3868.

Gaulme, P., F. Schmider, C. Grec, A. López Ariste, T. Widemann, and B. Gelly (2008), Venus wind map at cloud top level with the MTR/THEMIS visible spectrometer, I: Instrumental performance and first results, *Planet. Space Sci.*, *56*, 1335–1343, doi:10.1016/j.pss.2008.06.014.

Gérard, J., B. Hubert, V. I. Shematovich, D. V. Bisikalo, and G. R. Gladstone (2008a), The Venus ultraviolet oxygen dayglow and aurora: Model comparison with observations, *Planet. Space Sci.*, *56*, 542–552, doi:10.1016/j.pss.2007.11.008.

Gérard, J. C., A. I. F. Stewart, and S. W. Bougher (1981), The altitude distribution of the Venus ultraviolet nightglow and implications on vertical transport, *Geophys. Res. Lett.*, *8*, 633–636, doi:10.1029/GL008i006p00633.

Gérard, J. C., C. Cox, A. Saglam, J. Bertaux, E. Villard, and C. Nehmé (2008b), Limb observations of the ultraviolet nitric oxide nightglow with SPICAV on board Venus Express, *Journal of Geophysical Research (Planets)*, *113*(E12), doi: 10.1029/2008JE003078.

Gérard, J. C., A. Saglam, G. Piccioni, P. Drossart, C. Cox, S. Erard, R. Hueso, and A. Sánchez-Lavega (2008c), Distribution of the O_2 infrared nightglow observed with VIRTIS on board Venus Express, *Geophys. Res. Lett.*, *35*, doi: 10.1029/2007GL032021.

Gérard, J. C., C. Cox, L. Soret, A. Saglam, G. Piccioni, J. Bertaux, and P. Drossart (2009a), Concurrent observations of the ultraviolet nitric oxide and infrared O_2 nightglow emissions with Venus Express, *Journal of Geophysical Research (Planets)*, *114*(E00B44), doi:10.1029/2009JE003371.

Gérard, J. C., A. Saglam, G. Piccioni, P. Drossart, F. Montmessin, and J. Bertaux (2009b), Atomic oxygen distribution in the Venus mesosphere from observations of O_2 infrared airglow by VIRTIS-Venus Express, *Icarus*, *199*, 264–272, doi: 10.1016/j.icarus.2008.09.016.

Gérard, J. C., L. Soret, A. Saglam, G. Piccioni, and P. Drossart (2010), The distributions of the OH Meinel and $O_2(a^1\Delta{-}X^3\Sigma)$ nightglow emissions in the Venus mesosphere based on VIRTIS observations, *Advances in Space Research*, *45*, 1268–1275, doi:10.1016/j.asr.2010.01.022.

Gierasch, P. J. (1975), Meridional circulation and the maintenance of the Venus atmospheric rotation, *Journal of Atmospheric Sciences*, *32*, 1038–1044, doi: 10.1175/1520-0469(1975)032<1038:MCATMO>2.0.CO;2.

Gierasch, P. J., et al. (1997), The General Circulation of the Venus Atmosphere: an Assessment, in *Venus II: Geology, Geophysics, Atmosphere, and Solar Wind Environment*, edited by S. W. Bougher, D. M. Hunten, & R. J. Phillips, p. 459.

Gilli, G., M. A. López-Valverde, P. Drossart, G. Piccioni, S. Erard, and A. Cardesín Moinelo (2009), Limb observations of CO_2 and CO non-LTE emissions in the Venus atmosphere by VIRTIS/Venus Express, *Journal of Geophysical Research (Planets)*, *114*, doi:10.1029/2008JE003112.

Goldstein, J. J. (1989), Absolute wind measurements in the lower thermosphere of Venus using infrared heterodyne spectroscopy, Ph.D. thesis, Pennsylvania Univ., Philadelphia.

Goldstein, J. J., M. J. Mumma, T. Kostiuk, D. Deming, F. Espenak, and D. Zipoy (1991), Absolute wind velocities in the lower thermosphere of Venus using infrared heterodyne spectroscopy, *Icarus*, *94*, 45–63, doi:10.1016/0019-1035(91)90140-O.

Goldstein, R. M. (1964), Symposium on Radar and Radiometric Observations of Venus during the 1962 Conjunction: Venus characteristics by earth-based radar, *AJ*, *69*, 12–18, doi:10.1086/109221.

Gombosi, T. I. (1998), Physics of the Space Environment, Cambridge University Press (Cambridge Atmospheric and Space Science Series), Cambridge, New York.

Gulkis, S., R. K. Kakar, M. J. Klein, E. T. Olsen, and W. J. Wilson (1977), Venus - Detection of variations in stratospheric carbon monoxide, in *Planetary Atmospheres*, edited by A. Vallance Jones, pp. 61–65.

Gurwell, M. A., D. O. Muhleman, K. P. Shah, G. L. Berge, D. J. Rudy, and A. W. Grossman (1995), Observations of the CO bulge on Venus and implications for mesospheric winds, *Icarus*, *115*, 141–158, doi:10.1006/icar.1995.1085.

Hedin, A. E., H. G. Mayr, L. H. Brace, H. C. Brinton, D. T. Pelz, P. Bauer, G. R. Carignan, and A. D. Parks (1977a), Observations of neutral composition and related ionospheric variations during a magnetic storm in February 1974, *J. Geophys. Res.*, *82*, 3183–3189, doi:10.1029/JA082i022p03183.

Hedin, A. E., C. A. Reber, G. P. Newton, N. W. Spencer, H. C. Brinton, H. G. Mayr, and W. E. Potter (1977b), A global thermospheric model based on mass spectrometer and incoherent scatter data MSIS. II - Composition, *J. Geophys. Res.*, *82*, 2148–2156, doi:10.1029/JA082i016p02148.

Hedin, A. E., H. B. Niemann, W. T. Kasprzak, and A. Seiff (1983), Global empirical model of the Venus thermosphere, *Journal of Geophysical Research*, *88*, 73–83, doi:10.1029/JA088iA01p00073.

Herrnstein, A., and T. E. Dowling (2007), Effects of topography on the spin-up of a Venus atmospheric model, *Journal of Geophysical Research (Planets)*, *112*, E04S08, doi:10.1029/2006JE002804.

Hollenbach, D. J., R. C. Whitten, and S. S. Prasad (1985), The thermal structure of the dayside upper atmosphere of Venus above 125 KM, *Icarus*, *64*, 205–220, doi:10.1016/0019-1035(85)90086-7.

Hollingsworth, J. L., R. E. Young, G. Schubert, C. Covey, and A. S. Grossman (2007), A simple-physics global circulation model for Venus: Sensitivity assessments of atmospheric superrotation, *Geophys. Res. Lett.*, *34*, L05,202, doi: 10.1029/2006GL028567.

Hueso, R., A. Sánchez-Lavega, G. Piccioni, P. Drossart, J. C. Gérard, I. Khatuntsev, L. Zasova, and A. Migliorini (2008), Morphology and dynamics of Venus oxygen airglow from Venus Express/Visible and Infrared Thermal Imaging Spectrometer observations, *Journal of Geophysical Research (Planets)*, *113*(E12), doi: 10.1029/2008JE003081.

Huestis, D. L. (2002), Current Laboratory Experiments for Planetary Aeronomy, in *Atmospheres in the Solar System: Comparative Aeronomy*, edited by Mendillo, M., Nagy, A., & Waite, J. H., p. 245.

Huestis, D. L., S. W. Bougher, J. L. Fox, M. Galand, R. E. Johnson, J. I. Moses, and J. C. Pickering (2008), Cross Sections and Reaction Rates for Comparative Planetary Aeronomy, *Space Science Review*, *139*, 63–105, doi:10.1007/s11214-008-9383-7.

Jamieson, C., R. M. Garcia, D. A. Pejakovic, and K. S. Kalogerakis (2009a), Oxygen Atom Recombination in Carbon Dioxide Atmospheres, in *AAS/Division for Planetary Sciences Meeting Abstracts*, *AAS/Division for Planetary Sciences Meeting Abstracts*, vol. 41, p. 54.01.

Jamieson, C. S., R. M. Garcia, D. Pejakovic, and K. Kalogerakis (2009b), The Kinetics of Oxygen Atom Recombination in the Presence of Carbon Dioxide, *AGU Fall Meeting Abstracts*.

Kallio, E., R. Jarvinen, and P. Janhunen (2006), Venus solar wind interaction: Asymmetries and the escape of O^+ ions, *Planet. Space Sci.*, *54*, 1472–1481, doi:10.1016/j.pss.2006.04.030.

Kasprzak, W. T., A. E. Hedin, H. G. Mayr, and H. B. Niemann (1988), Wavelike perturbations observed in the neutral thermosphere of Venus, *J. Geophys. Res.*, *93*, 11,237–11,245, doi:10.1029/JA093iA10p11237.

Kasprzak, W. T., H. B. Niemann, A. E. Hedin, and S. W. Bougher (1993), Wave-like perturbations observed at low altitudes by the Pioneer Venus Orbiter Neutral Mass Spectrometer during orbiter entry, *Geophys. Res. Lett.*, *20*, 2755–2758, doi:10.1029/93GL02628.

Kasprzak, W. T., G. M. Keating, N. C. Hsu, A. I. F. Stewart, W. B. Colwell, and S. W. Bougher (1997), Solar Activity Behavior of the Thermosphere, in *Venus II: Geology, Geophysics, Atmosphere, and Solar Wind Environment*, edited by S. W. Bougher, D. M. Hunten, & R. J. Phillips.

Keating, G. M., and N. C. Hsu (1993), The Venus atmospheric response to solar cycle variations, *Geophys. Res. Lett.*, *20*, 2751–2754, doi:10.1029/93GL03010.

Keating, G. M., F. W. Taylor, J. Y. Nicholson, and E. W. Hinson (1979a), Short-term cyclic variations and diurnal variations of the Venus upper atmosphere, *Science*, *205*, 62–64, doi:10.1126/science.205.4401.62.

Keating, G. M., F. W. Taylor, J. Y. Nicholson, and E. W. Hinson (1979b), Short-term cyclic variations and diurnal variations of the Venus upper atmosphere, *Science*, *205*, 62–64, doi:10.1126/science.205.4401.62.

Keating, G. M., R. H. Tolson, and E. W. Hinson (1979c), Venus thermosphere and exosphere - First satellite drag measurements of an extraterrestrial atmosphere, *Science*, *203*, 772–774, doi:10.1126/science.203.4382.772.

Keating, G. M., J. Y. Nicholson, and L. R. Lake (1980), Venus upper atmosphere structure, *J. Geophys. Res.*, *85*, 7941–7956, doi:10.1029/JA085iA13p07941.

Keating, G. M., J. L. Bertaux, S. W. Bougher, R. E. Dickinson, T. E. Cravens, and A. E. Hedin (1985), Models of Venus neutral upper atmosphere - Structure and composition, *Advances in Space Research*, *5*, 117–171, doi:10.1016/0273-1177(85)90200-5.

Kerzhanovich, V. V., et al. (1983), Vertical profiles of wind velocity in the Venus atmosphere according to Doppler measurements of the Venera-13 and Venera-14 probes, *Kosmicheskie Issledovaniia*, *21*, 211–217.

Kliore, A., G. S. Levy, D. L. Cain, G. Fjeldbo, and S. I. Rasool (1967), Atmosphere and Ionosphere of Venus from the Mariner V S-Band Radio Occultation Measurement, *Science*, *158*, 1683–1688, doi:10.1126/science.158.3809.1683.

Kliore, A. J., and I. R. Patel (1980), Vertical structure of the atmosphere of Venus from Pioneer Venus orbiter radio occultations, *J. Geophys. Res.*, *85*, 7957–7962, doi:10.1029/JA085iA13p07957.

Krasnopolsky, V. A. (1983), Venus spectroscopy in the 3000-8000 A region by Veneras 9 and 10, in *Venus*, edited by Hunten, D. M., Colin, L., Donahue, T. M., & Moroz, V. I., pp. 459–483.

Krasnopolsky, V. A. (2010), Venus night airglow: Ground-based detection of OH, observations of O_2 emissions, and photochemical model, *Icarus*, *207*, 17–27, doi:10.1016/j.icarus.2009.10.019.

Krasnopolsky, V. A., and V. A. Parshev (1981), Chemical composition of the atmosphere of Venus, *Nature*, *292*, 610–613, doi:10.1038/292610a0.

Kumar, S., and A. L. Broadfoot (1975), He 584 A airglow emission from Venus - Mariner 10 observations, *Geophys. Res. Lett.*, *2*, 357–360, doi:10.1029/GL002i008p00357.

Lebonnois, S., F. Hourdin, V. Eymet, A. Crespin, R. Fournier, and F. Forget (2010), Superrotation of Venus' atmosphere analyzed with a full general circulation model, *Journal of Geophysical Research (Planets)*, *115*, E06,006, doi:10.1029/2009JE003458.

Lee, C., and M. I. Richardson (2010), A general circulation model ensemble study of the atmospheric circulation of Venus, *Journal of Geophysical Research (Planets)*, *115*, E04,002, doi:10.1029/2009JE003490.

Lee, C., M. I. Richardson, C. Newman, and A. D. Toigo (2006), VenusWRF: A New Venus GCM Using PlanetWRF, in *Bulletin of the American Astronomical Society*, *Bulletin of the American Astronomical Society*, vol. 38, pp. 526–+.

Lellouch, E., J. J. Goldstein, J. Rosenqvist, S. W. Bougher, and G. Paubert (1994), Global circulation, thermal structure, and carbon monoxide distribution in Venus' mesosphere in 1991, *Icarus*, *110*, 315–339, doi:10.1006/icar.1994.1125.

Lellouch, E., T. Clancy, D. Crisp, A. J. Kliore, D. Titov, and S. W. Bougher (1997), Monitoring of Mesospheric Structure and Dynamics, in *Venus II: Geology, Geophysics, Atmosphere, and Solar Wind Environment*, edited by S. W. Bougher, D. M. Hunten, & R. J. Phillips, pp. 295 – 324.

Lellouch, E., G. Paubert, R. Moreno, and A. Moullet (2008), Monitoring Venus' mesospheric winds in support of Venus Express: IRAM 30-m and APEX observations, *Planet. Space Sci.*, *56*, 1355–1367, doi:10.1016/j.pss.2008.06.010.

Limaye, S. S. (1990), Venus: Thermal Tides in the Venera 15 Fourier Spectrometer Data Between 300-1300 cm $^{-1}$, in *Bulletin of the American Astronomical Society*, *Bulletin of the American Astronomical Society*, vol. 22, p. 1052.

Limaye, S. S. (2007), Venus atmospheric circulation: Known and unknown, *Journal of Geophysical Research (Planets)*, *112*, E04S09, doi:10.1029/2006JE002814.

Lindzen, R. S. (1971), Tides and Gravity Waves in the Upper Atmosphere, in *Mesospheric Models and Related Experiments*, *Astrophysics and Space Science Library*, vol. 25, edited by G. Fiocco, p. 122.

López-Valverde, M. A., P. Drossart, R. Carlson, R. Mehlman, and M. Roos-Serote (2007), Non-LTE infrared observations at Venus: From NIMS/Galileo to VIRTIS/Venus Express, *Planet. Space Sci.*, *55*, 1757–1771, doi:10.1016/j.pss.2007.01.008.

Maillard, J., E. Lellouch, J. Crovisier, C. de Bergh, and B. Bézard (1995), Carbon Monoxide 4.7 μm Emission: A New Dynamical Probe of Venus' Thermosphere, in *Bulletin of the American Astronomical Society*, *Bulletin of the American Astronomical Society*, vol. 27, p. 1080.

Markiewicz, W. J., et al. (2007), Morphology and dynamics of the upper cloud layer of Venus, *Nature*, *450*, 633–636, doi:10.1038/nature06320.

Massie, S. T., D. M. Hunten, and D. R. Sowell (1983), Day and night models of the Venus thermosphere, *J. Geophys. Res.*, *88*, 3955–3969, doi:10.1029/JA088iA05p03955.

Mayr, H. G., I. Harris, H. B. Niemann, H. C. Brinton, N. W. Spencer, H. A. Taylor, R. E. Hartle, W. R. Hoegy, and D. M. Hunten (1980), Dynamic properties of the thermosphere inferred from Pioneer Venus mass spectrometer measurements, *J. Geophys. Res.*, *85*, 7841–7847, doi:10.1029/JA085iA13p07841.

Mayr, H. G., I. Harris, D. R. Stevens-Rayburn, H. B. Niemann, H. A. Taylor, and R. E. Hartle (1985), On the diurnal variations in the temperature and composition - A three-dimensional model with superrotation, *Advances in Space Research*, *5*, 109–112, doi:10.1016/0273-1177(85)90277-7.

McGouldrick, K., and O. B. Toon (2008), Observable effects of convection and gravity waves on the Venus condensational cloud, *Planet. Space Sci.*, *56*, 1112–1131, doi: 10.1016/j.pss.2008.02.010.

McGouldrick, K., K. H. Baines, T. W. Momary, and D. H. Grinspoon (2008), Venus Express/VIRTIS observations of middle and lower cloud variability and implications for dynamics, *Journal of Geophysical Research (Planets)*, *113*(E12), doi: 10.1029/2008JE003113.

Mehr, F. J., and M. A. Biondi (1969), Electron Temperature Dependence of Recombination of O_2^+ and N_2^+ Ions with Electrons, *Physical Review*, *181*, 264–271, doi:10.1103/PhysRev.181.264.

Mengel, J. G., D. R. Stevens-Rayburn, H. G. Mayr, and I. Harris (1989), Non-linear three dimensional spectral model of the venusian thermosphere with super-rotation-II. Temperature, composition, and winds, *Planet. Space Sci.*, *37*, 707–722, doi: 10.1016/0032-0633(89)90041-X.

Moissl, R., et al. (2009), Venus cloud top winds from tracking UV features in Venus Monitoring Camera images, *Journal of Geophysical Research (Planets)*, *114*, E00B31, doi:10.1029/2008JE003117.

Mueller-Wodarg, I., S. Bruinsma, J. M. Forbes, R. Keating, S. Yelle Sci. Gerald, P. Withers, and M. A. Lopez-Valverde (2008), The structure of Venus' Upper Atmosphere and forthcoming measurements by the Venus Express Atmospheric Drag Experiment, in *37th COSPAR Scientific Assembly*, *COSPAR, Plenary Meeting*, vol. 37.

Murray, B. C., et al. (1974), Venus: Atmospheric Motion and Structure from Mariner 10 Pictures, *Science*, *183*, 1307–1315, doi:10.1126/science.183.4131.1307.

Nagy, A. F., T. E. Cravens, S. G. Smith, H. A. Taylor, and H. C. Brinton (1980), Model calculations of the dayside ionosphere of Venus - Ionic composition, *J. Geophys. Res.*, *85*, 7795–7801, doi:10.1029/JA085iA13p07795.

Nair, H., M. Allen, A. D. Anbar, Y. L. Yung, and R. T. Clancy (1994), A photochemical model of the martian atmosphere, *Icarus*, *111*, 124–150, doi: 10.1006/icar.1994.1137.

Najib, D. (2010), 3-D, multi-fluid, high spatial resolution, MHD model studies of the solar wind interaction with Mars, *J. Geophys. Res.*, doi:Submitted.

Newman, M., and C. Leovy (1992), Maintenance of strong rotational winds in Venus' middle atmosphere by thermal tides, *Science*, *257*, 647–650, doi: 10.1126/science.257.5070.647.

Newman, S. M., I. C. Lane, A. J. Orr-Ewing, D. A. Newnham, and J. Ballard (1999), Integrated absorption intensity and Einstein coefficients for the O_2 $a^1\Delta_g$-X $^3\Sigma_g^-$

(0,0) transition: A comparison of cavity ringdown and high resolution Fourier transform spectroscopy with a long-path absorption cell, *Journal of Chemical Physics*, *110*, 10,749–10,757, doi:10.1063/1.479018.

Niemann, H. B., R. E. Hartle, A. E. Hedin, W. T. Kasprzak, N. W. Spencer, D. M. Hunten, and G. R. Carignan (1979), Venus upper atmosphere neutral gas composition - First observations of the diurnal variations, *Science*, *205*, 54–56, doi:10.1126/science.205.4401.54.

Niemann, H. B., W. T. Kasprzak, A. E. Hedin, D. M. Hunten, and N. W. Spencer (1980), Mass spectrometric measurements of the neutral gas composition of the thermosphere and exosphere of Venus, *Journal of Geophysical Research*, *85*, 7817–7827, doi:10.1029/JA085iA13p07817.

Ohtsuki, S., N. Iwagami, H. Sagawa, Y. Kasaba, M. Ueno, and T. Imamura (2005), Ground-based observation of the Venus 1.27-μm O_2 airglow, *Advances in Space Research*, *36*, 2038–2042, doi:10.1016/j.asr.2005.05.078.

Ohtsuki, S., N. Iwagami, H. Sagawa, M. Ueno, Y. Kasaba, T. Imamura, and E. Nishihara (2008), Imaging spectroscopy of the Venus 1.27-μm O_2 airglow with ground-based telescopes, *Advances in Space Research*, *41*, 1375–1380, doi:10.1016/j.asr.2007.10.014.

Parish, H. F., G. Schubert, C. Covey, R. L. Walterscheid, A. Grossman, and S. Lebonnois (2010), Decadal variations in a Venus General Circulation Model, *Icarus*, doi:10.1016/j.icarus.2010.11.015 in press.

Pätzold, M., et al. (2007), The structure of Venus' middle atmosphere and ionosphere, *Nature*, *450*, 657–660, doi:10.1038/nature06239.

Paxton, L. J. (1985), Pioneer Venus orbiter ultraviolet spectrometer limb observations - Analysis and interpretation of the 166- and 156-nm data, *J. Geophys. Res.*, *90*, 5089–5096, doi:10.1029/JA090iA06p05089.

Paxton, L. J. (1988), CO^+ and N_2^+ in the Venus ionosphere, *J. Geophys. Res.*, *93*, 8473–8482, doi:10.1029/JA093iA08p08473.

Paxton, L. J., D. E. Anderson, and A. I. F. Stewart (1988), Erratum: Analysis of Pioneer Venus orbiter ultraviolet spectrometer Lyman α data from near the subsolar region [J. Geophys. Res. 93(A3), 1766-1772 (1988)], *J. Geophys. Res.*, *93*, 11,551–11,551, doi:10.1029/JA093iA10p11551.

Pechmann, J. B., and A. P. Ingersoll (1984), Thermal tides in the atmosphere of Venus - Comparison of model results with observations, *Journal of Atmospheric Sciences*, *41*, 3290–3313, doi:10.1175/1520-0469(1984)041<3290:TTITAO>2.0.CO;2.

Peralta, J., R. Hueso, A. Sánchez-Lavega, G. Piccioni, O. Lanciano, and P. Drossart (2008), Characterization of mesoscale gravity waves in the upper and lower clouds of Venus from VEX-VIRTIS images, *Journal of Geophysical Research (Planets)*, *113*(E12), doi:10.1029/2008JE003185.

Piccioni, G., L. Zasova, A. Migliorini, P. Drossart, A. Shakun, A. García Muñoz, F. P. Mills, and A. Cardesin-Moinelo (2009), Near-IR oxygen nightglow observed by VIRTIS in the Venus upper atmosphere, *Journal of Geophysical Research (Planets)*, *114*(E00B38), doi:10.1029/2008JE003133.

Piccioni, G., et al. (2007), South-polar features on Venus similar to those near the north pole, *Nature*, *450*, 637–640, doi:10.1038/nature06209.

Piccioni, G., et al. (2008), First detection of hydroxyl in the atmosphere of Venus, *Astron. Astrophys.*, *483*, L29–L33, doi:10.1051/0004-6361:200809761.

Pollack, J. B., and C. Sagan (1965a), The Microwave Phase Effect of Venus, *Icarus*, *4*, 62–103, doi:10.1016/0019-1035(65)90018-7.

Pollack, J. B., and C. Sagan (1965b), The Infrared Limb Darkening of Venus, *J. Geophys. Res.*, *70*, 4403–4426, doi:10.1029/JZ070i018p04403.

Rafkin, S., A. Stern, S. Bougher, and A. Brecht (2007), VTGCM and Applications to VEX and PVO Data Analysis: Upgraded Simulations (F10.7∼70 and 200), in *Venus Express Science Meeting, held 18-24 March in Thuile, Italy.*

Rengel, M., P. Hartogh, and C. Jarchow (2008), Mesospheric vertical thermal structure and winds on Venus from HHSMT CO spectral-line observations, *Planet. Space Sci.*, *56*, 1368–1384, doi:10.1016/j.pss.2008.07.004.

Robert, A. J. (1966), A solar EUV flux model, *J. Meteor. Soc. Japan*, *44*, 237–245.

Roldán, C., M. A. López-Valverde, M. López-Puertas, and D. P. Edwards (2000), Non-LTE Infrared Emissions of CO_2 in the Atmosphere of Venus, *Icarus*, *147*, 11–25, doi:10.1006/icar.2000.6432.

Rosenqvist, J., E. Lellouch, T. Encrenaz, and G. Paubert (1995), Global Circulation in Venus' Mesosphere from IRAM CO Observations (1991-1994): A Tribute to Jan Rosenqvist, in *Bulletin of the American Astronomical Society*, *Bulletin of the American Astronomical Society*, vol. 27, p. 1080.

Rossow, W. B., and G. P. Williams (1979), Large-scale motion in the Venus stratosphere, *Journal of Atmospheric Sciences*, *36*, 377–389, doi:10.1175/1520-0469(1979)036<0377:LSMITV>2.0.CO;2.

Rossow, W. B., S. B. Fels, and P. H. Stone (1980), Comments on "A three-dimensional model of dynamical processes in the Venus atmosphere", *Journal of Atmospheric Sciences*, *37*, 250–252, doi:10.1175/1520-0469(1980)037<0250:COTDMO>2.0.CO;2.

Rottman, G. J., and H. W. Moos (1973), The ultraviolet (1200 - 1900 Ångstrom) spectrum of Venus., *J. Geophys. Res.*, *78*, 8033–8048, doi:10.1029/JA078i034p08033.

Rusch, D. W., and T. E. Cravens (1979), A model of the neutral and ion nitrogen chemistry in the daytime thermosphere of Venus, *Geophys. Res. Lett.*, *6*, 791–794, doi:10.1029/GL006i010p00791.

Sagan, C. (1961), The Planet Venus, *Science*, *133*, 849–858, doi: 10.1126/science.133.3456.849.

Sánchez-Lavega, A., et al. (2008), Variable winds on Venus mapped in three dimensions, *Geophys. Res. Lett.*, *35*, 13,204–+, doi:10.1029/2008GL033817.

Sander, S. P., and et al. (2003), Chemical Kinetics and Photochemical Data for use in Atmospheric Studies, Evaluation No. 14, *JPL Publication 02-25*.

Schloerb, F. P., S. E. Robinson, and W. M. Irvine (1980), Observations of CO in the stratosphere of Venus via its J = 0 - 1 rotational transition, *Icarus*, *43*, 121–127, doi:10.1016/0019-1035(80)90112-8.

Schmülling, F., J. Goldstein, T. Kostiuk, T. Hewagama, and D. Zipoy (2000), High precision Wind measurements in the upper Venus atmosphere, in *Bulletin of the American Astronomical Society*, *Bulletin of the American Astronomical Society*, vol. 32, p. 1121.

Schofield, J. T., and F. W. Taylor (1983), Measurements of the mean, solar-fixed temperature and cloud structure of the middle atmosphere of Venus, *Quarterly Journal of the Royal Meteorological Society*, *109*, 57–80, doi:10.1256/smsqj.45903.

Schubert, G. (1983), General circulation and the dynamical state of the Venus atmosphere, in *Venus*, edited by Hunten, D. M., Colin, L., Donahue, T. M., & Moroz, V. I., pp. 681–765.

Schubert, G., and J. A. Whitehead (1969), Moving Flame Experiment with Liquid Mercury: Possible Implications for the Venus Atmosphere, *Science*, *163*, 71–72, doi:10.1126/science.163.3862.71.

Schubert, G., S. W. Bougher, A. D. Covey, C. C.and Del Genio, A. S. Grossman, J. L. Hollingsworth, S. S. Limaye, and R. E. Young (2007), Venus atmosphere dynamics: A continuing enigma, in *Exploring Venus as terrestrial planet, AGU Geophysical Monograph 176*, edited by L. W. Esposito, E. R. Stofan, & T. E. Cravens, pp. 121–138.

Schubert, G., et al. (1980), Structure and circulation of the Venus atmosphere, *J. Geophys. Res.*, *85*, 8007–8025, doi:10.1029/JA085iA13p08007.

Schunk, R. W., and A. F. Nagy (2009), Ionospheres: Physics, Plasma Physics, and Chemisty, Cambridge University Press (Cambridge Atmospheric and Space Science Series), Cambridge, New York.

Seiff, A. (1983), Thermal structure of the atmosphere of Venus, in *Venus*, edited by Hunten, D. M., Colin, L., Donahue, T. M., & Moroz, V. I., pp. 215–279.

Seiff, A. (1991), Waves in Venus's middle and upper atmosphere: Implications of Pioneer Venus probe data above the clouds, *J. Geophys. Res.*, *96*, 11,021–11,032, doi:10.1029/91JA01101.

Seiff, A., and D. B. Kirk (1982), Structure of the Venus mesosphere and lower thermosphere from measurements during entry of the Pioneer Venus probes, *Icarus*, *49*, 49–70, doi:10.1016/0019-1035(82)90056-2.

Seiff, A., D. B. Kirk, R. E. Young, R. C. Blanchard, J. T. Findlay, G. M. Kelly, and S. C. Sommer (1980), Measurements of thermal structure and thermal contrasts in the atmosphere of Venus and related dynamical observations - Results from the four Pioneer Venus probes, *J. Geophys. Res.*, *85*, 7903–7933, doi: 10.1029/JA085iA13p07903.

Seiff, A., J. T. Schofield, A. J. Kliore, F. W. Taylor, and S. S. Limaye (1985), Models of the structure of the atmosphere of Venus from the surface to 100 kilometers altitude, *Advances in Space Research*, *5*, 3–58, doi:10.1016/0273-1177(85)90197-8.

Shah, K. P., D. O. Muhleman, and G. L. Berge (1991), Measurement of winds in Venus' upper mesosphere based on Doppler shifts of the 2.6-mm (C-12)O line, *Icarus*, *93*, 96–121, doi:10.1016/0019-1035(91)90167-R.

Shapiro, I. I. (1968), Rotation of Venus, *Science*, *159*, 1124, doi: 10.1126/science.159.3819.1124.

Shapiro, R. (1970), Smoothing, Filtering, and Boundary Effects, *Reviews of Geophysics and Space Physics*, *8*, 359–387.

Shimazaki, T., R. C. Whitten, W. C. Knudsen, K. L. Miller, and H. T. Woodward (1984), The dayside Venus ionosphere. II - Combined numerical model of ion and neutral composition above 120 KM, *Icarus*, *60*, 654–674, doi:10.1016/0019-1035(84)90171-4.

Sonnabend, G., P. Kroetz, M. Sornig, and D. Stupar (2010), Direct observations of Venus upper mesospheric temperatures from ground based spectroscopy of CO_2, *Geophys. Res. Lett.*, *37*, L11,102, doi:10.1029/2010GL043335.

Soret, L., J. C. Gérard, A. Saglam, G. Piccioni, and P. Drossart (2009), Latitudinal - local time distribution of the O_2 and OH infrared nightglows and O density in the Venus lower thermosphere, in *European Planetary Science Congress, held 14-18 September in Potsdam, Germany. http://meetings.copernicus.org/epsc2009, p.160.*

Soret, L., J. C. Gérard, F. Montmessin, G. Piccioni, P. Drossart, and J.-L. Bertaux (2010a), Atomic Oxygen on the Venus Nightside: global distribution deduced from airglow mapping, *Icarus, This Issue.*

Soret, L., J. C. Gérard, G. Piccioni, and P. Drossart (2010b), Venus OH Nightglow Distribution from VIRTIS Limb Observations from Venus Express, *Geophys. Res. Lett.*, *37*(L06805), doi:10.1029/2010GL042377.

Sornig, M. (2009), Investigations of Upper Atmosphere Dynamics on Mars and Venus by High Resolution Infrared Heterodyne Spectroscopy of CO_2, Ph.D. thesis, Physikalisches Institut, Universität zu Köln, Köln, Germany.

Sornig, M., T. Livengood, G. Sonnabend, P. Kroetz, D. Stupar, T. Kostiuk, and R. Schieder (2008), Venus upper atmosphere winds from ground-based heterodyne spectroscopy of CO_2 at 10μm wavelength, *Planet. Space Sci.*, *56*, 1399–1406, doi:10.1016/j.pss.2008.05.006.

Stevens-Rayburn, D. R., J. G. Mengel, I. Harris, and H. G. Mayr (1989), Non-linear three dimensional spectral model of the Venusian thermosphere with super-rotation. I - Formulation and numerical technique. II - Temperature, composition, and winds, *Planet. Space Sci.*, *37*, 701–705, doi:10.1016/0032-0633(89)90040-8.

Stewart, A. I., and C. A. Barth (1979), Ultraviolet night airglow of Venus, *Science*, *205*, 59–62, doi:10.1126/science.205.4401.59.

Stewart, A. I. F., J. Gerard, D. W. Rusch, and S. W. Bougher (1980), Morphology of the Venus ultraviolet night airglow, *J. Geophys. Res.*, *85*, 7861–7870, doi:10.1029/JA085iA13p07861.

Strickland, D. J. (1973), The O I 1304- and 1356-Å emission from the atmosphere of Venus., *J. Geophys. Res.*, *78*, 2827–2836, doi:10.1029/JA078i016p02827.

Suomi, V. E., and S. S. Limaye (1978), Venus - Further evidence of vortex circulation, *Science*, *201*, 1009–1011, doi:10.1126/science.201.4360.1009.

Svedhem, H., D. Titov, F. Taylor, and O. Witasse (2009), Venus Express mission, *Journal of Geophysical Research (Planets)*, *114*, E00B33, doi:10.1029/2008JE003290.

Taylor, F. W., F. E. Vescelus, J. R. Locke, R. Beer, G. T. Foster, P. B. Forney, J. T. Houghton, J. Delderfield, and J. T. Schofield (1979), Infrared radiometer for the Pioneer Venus orbiter. I - Instrument description, *Applied Optics*, *18*, 3893–3900, doi:10.1364/AO.18.003893.

Taylor, F. W., D. M. Hunten, and L. V. Ksanfomaliti (1983), The thermal balance of the middle and upper atmosphere of Venus, in *Venus*, edited by Hunten, D. M., Colin, L., Donahue, T. M., & Moroz, V. I., pp. 650–680.

Taylor, F. W., et al. (1980), Structure and meteorology of the middle atmosphere of Venus Infrared remote sensing from the Pioneer orbiter, *J. Geophys. Res.*, *85*, 7963–8006, doi:10.1029/JA085iA13p07963.

Theis, R. F., L. H. Brace, and H. G. Mayr (1980), Empirical models of the electron temperature and density in the Venus ionosphere, *J. Geophys. Res.*, *85*, 7787–7794, doi:10.1029/JA085iA13p07787.

Thompson, R. (1970), Venus's General Circulation is a Merry-Go-Round., *Journal of Atmospheric Sciences*, *27*, 1107–1116, doi:10.1175/1520-0469(1970)027<1107:VGCIAM>2.0.CO;2.

Titov, D. V., F. W. Taylor, H. Svedhem, N. I. Ignatiev, W. J. Markiewicz, G. Piccioni, and P. Drossart (2008), Atmospheric structure and dynamics as the cause of ultraviolet markings in the clouds of Venus, *Nature*, *456*, 620–623, doi: 10.1038/nature07466.

Tobiska, W. K., and C. A. Barth (1990), A solar EUV flux model, *J. Geophys. Res.*, *95*, 8243–8251, doi:10.1029/JA095iA06p08243.

Torr, M. R., and D. G. Torr (1985), Ionization frequencies for solar cycle 21 - Revised, *J. Geophys. Res.*, *90*, 6675–6678, doi:10.1029/JA090iA07p06675.

Torr, M. R., D. G. Torr, R. A. Ong, and H. E. Hinteregger (1979), Ionization frequencies for major thermospheric constituents as a function of solar cycle 21, *Geophys. Res. Lett.*, *6*, 771–774, doi:10.1029/GL006i010p00771.

Torr, M. R., D. G. Torr, and H. E. Hinteregger (1980), Solar flux variability in the Schumann-Runge continuum as a function of solar cycle 21, *J. Geophys. Res.*, *85*, 6063–6068, doi:10.1029/JA085iA11p06063.

Vandaele, A. C., et al. (2008), Composition of the Venus mesosphere measured by Solar Occultation at Infrared on board Venus Express, *Journal of Geophysical Research (Planets)*, *113*, doi:10.1029/2008JE003140.

von Zahn, U., K. H. Fricke, H. Hoffmann, and K. Pelka (1979), Venus - Eddy coefficients in the thermosphere and the inferred helium content of the lower atmosphere, *Geophys. Res. Lett.*, *6*, 337–340.

von Zahn, U., K. H. Fricke, D. M. Hunten, D. Krankowsky, K. Mauersberger, and O. A. Nier (1980), The upper atmosphere of Venus during morning conditions, *J. Geophys. Res.*, *85*, 7829–7840, doi:10.1029/JA085iA13p07829.

von Zahn, U., S. Kumar, H. Niemann, and R. Prinn (1983), Composition of the Venus atmosphere, in *Venus*, edited by Hunten, D. M., Colin, L., Donahue, T. M., & Moroz, V. I., pp. 299–430.

Washington, W. M., and D. L. Williamson (1977), A description of the NCAR global circulation models., in *Methods in Computational Physics. General Circulation Models of the Atmosphere*, vol. 17, edited by J. Chang, pp. 111–172.

Widemann, T., E. Lellouch, and A. Campargue (2007), New wind measurements in Venus' lower mesosphere from visible spectroscopy, *Planet. Space Sci.*, *55*, 1741–1756, doi:10.1016/j.pss.2007.01.005.

Widemann, T., E. Lellouch, and J. Donati (2008), Venus Doppler winds at cloud tops observed with ESPaDOnS at CFHT, *Planet. Space Sci.*, *56*, 1320–1334, doi:10.1016/j.pss.2008.07.005.

Wildt, R. (1940a), Note on the Surface Temperature of Venus., *ApJ*, *91*, 266–268, doi:10.1086/144165.

Wildt, R. (1940b), On the Possible Existence of Formaldehyde in the Atmosphere of Venus., *ApJ*, *92*, 247–255, doi:10.1086/144214.

Williamson, D. L. (1976), Linear stability of finite-difference approximations on a uniform latitude-longitude grid with fourier filtering, *Monthly Weather Review*, *104*(1), 31–41, doi:10.1175/1520-0493(1976)104<0031:LSOFDA>2.0.CO;2.

Williamson, D. L., and G. L. Browning (1973), Comparison of Grids and Difference Approximations for Numerical Weather Prediction Over a Sphere., *Journal of Applied Meteorology*, *12*, 264–274, doi:10.1175/1520-0450(1973)012<0264:COGADA>2.0.CO;2.

Williamson, D. L., G. L. Browning, T. Sasamori, and R. K. Sato (1977), Description of the NCAR Global Circulation Model with Transformed z Vertical Coordinate and Fourth-Order Horizontal Difference Approximations, in *NCAR Ms. 0501/77-6*.

Yamamoto, M., and M. Takahashi (2003a), The Fully Developed Superrotation Simulated by a General Circulation Model of a Venus-like Atmosphere., *Journal of Atmospheric Sciences*, *60*, 561–574, doi:10.1175/1520-0469(2003)060<0561:TFDSSB>2.0.CO;2.

Yamamoto, M., and M. Takahashi (2003b), Superrotation and equatorial waves in a T21 Venus-like AGCM, *Geophys. Res. Lett.*, *30*(9), 1449, doi:10.1029/2003GL016924.

Yamamoto, M., and M. Takahashi (2004), Dynamics of Venus' superrotation: The eddy momentum transport processes newly found in a GCM, *Geophys. Res. Lett.*, *31*, L09,701, doi:10.1029/2004GL019518.

Yamamoto, M., and M. Takahashi (2006a), An aerosol transport model based on a two-moment microphysical parameterization in the Venus middle atmosphere: Model description and preliminary experiments, *Journal of Geophysical Research (Planets)*, *111*, E08,002, doi:10.1029/2006JE002688.

Yamamoto, M., and M. Takahashi (2006b), Superrotation Maintained by Meridional Circulation and Waves in a Venus-Like AGCM, *Journal of Atmospheric Sciences*, *63*, 3296–3314, doi:10.1175/JAS3859.1.

Yamamoto, M., and M. Takahashi (2007a), A parametric study of atmospheric superrotation on Venus-like planets: Effects of oblique angle of planetary rotation axis, *Geophys. Res. Lett.*, *34*, L16,202, doi:10.1029/2007GL030220.

Yamamoto, M., and M. Takahashi (2007b), Simulations of superrotation using a GCM for Venus' middle atmosphere, *Earth, Planets, and Space*, *59*, 971–979.

Yamamoto, M., and M. Takahashi (2009a), Influences of Venus' topography on fully developed superrotation and near-surface flow, *Earth, Planets, and Space*, *61*.

Yamamoto, M., and M. Takahashi (2009b), Dynamical effects of solar heating below the cloud layer in a Venus-like atmosphere, *Journal of Geophysical Research (Planets)*, *114*, doi:10.1029/2009JE003381.

Young, R. E., and J. B. Pollack (1977), A three-dimensional model of dynamical processes in the Venus atmosphere, *Journal of Atmospheric Sciences*, *34*, 1315–1351, doi:10.1175/1520-0469(1977)034<1315:ATMODP>2.0.CO;2.

Young, R. E., and J. B. Pollack (1980), Reply., *Journal of Atmospheric Sciences*, *37*, 253–256, doi:10.1175/1520-0469(1980)037<0253:R>2.0.CO;2.

Yung, Y. L., and W. B. Demore (1982), Photochemistry of the stratosphere of Venus - Implications for atmospheric evolution, *Icarus*, *51*, 199–247, doi:10.1016/0019-1035(82)90080-X.

Zasova, L. V., V. I. Moroz, V. M. Linkin, I. V. Khatuntsev, and B. S. Maiorov (2006), Structure of the Venusian atmosphere from surface up to 100 km, *Cosmic Research*, *44*, 364–383, doi:10.1134/S0010952506040095.

Zhang, S., S. W. Bougher, and M. J. Alexander (1996), The impact of gravity waves on the Venus thermosphere and O_2 IR nightglow, *J. Geophys. Res.*, *101*, 23,195–23,206, doi:10.1029/96JE02035.